

## ABSTRACT

Title of Document:                   STUDIES OF HIGH FREQUENCY WAVE  
EXCITATION IN FAST AND SLOW WAVE  
VACUUM DEVICES

Jiao Yu, Doctor of Philosophy, 2011

Directed By:                         Professor Thomas M, Antonsen, Jr., Department  
of Electrical and Computer Engineering and  
Department of Physics

THz and millimeter-wave length radiation is widely used in imaging, detection and plasma heating. Vacuum electronic devices are the most efficient sources of high power radiation in the THz and millimeter range. Efforts to increase power by increasing current, are hampered by self-field effects and instabilities. Two examples of these effects are considered: the reduction in bunching efficiency in orotrons (a slow wave device), and the excitation of backward wave instabilities, in gyrotrons (a fast wave device).

The goal of producing THz radiation from miniature electron beam devices has refocused interest in orotrons. The efficiency of these devices improves with increasing current density. However, with increasing current density, self-fields become more important. Here, the theory of self-fields in a planar orotron is developed. We find that the parameters of the grating, which provides the slow wave

fields that interact with the beam, also affect the self-fields, which give rise to the slow space charge wave. Thus, optimization of the grating parameters requires consideration of their impact on the dispersive properties of the slow space charge wave. We present a sample structure design appropriate for a planar orotron.

Heating plasma to fusion temperatures will require multi megawatts of continuous wave (CW) power. Gyrotrons are the sources of choice for this heating. However, the maximum CW power from a single gyrotron is about 1.5MW. Efforts to increase gyrotrons power have led to instabilities in the electron beam. Here, the starting conditions for excitation of backward waves in the beam tunnel between the electron gun and the cavity of a high-power gyrotron are studied. The excitation of these waves leads to electron energy spread that spoils the beam quality and, hence, degrades the gyrotron efficiency. The suppression of these modes by a resistive coating on the wall of a smooth beam tunnel is examined. The guiding magnetic field and the tunnel wall radius vary along the axis, so the theory is essentially the small-signal theory of a gyro-backward-wave oscillator (gyro-BWO) with tapered parameters. The velocity spread and space charge of the beam will affect the interaction between the electron beam and backward wave. We find that space charge significantly lowers backward wave start currents and suppression of the space charge effect is key to operating at higher currents.

STUDIES OF HIGH FREQUENCY WAVE EXCITATION IN FAST AND SLOW  
WAVE VACUUM DEVICES

By

Jiao Yu

Dissertation submitted to the Faculty of the Graduate School of the  
University of Maryland, College Park, in partial fulfillment  
of the requirements for the degree of  
Doctor of Philosophy  
2011

Advisory Committee:  
Professor Thomas M. Antonsen, Jr., Chair  
Professor Gregory S. Nusinovich  
Professor Victor L. Granatstein  
Professor Thomas E. Murphy  
Professor Adil B. Hassam

© Copyright by  
Jiao Yu  
2011

## Acknowledgements

It is a pleasure to thank the many people who made this thesis possible!

First of all, I would like to express my deep and sincere gratitude to my advisor, Professor Antonsen. Through my Ph.D. study, he provided encouragements, sound advises, good teaching and tons of good ideas to me. His patient guidance in both my research and writing helped me a lot. I could not image having a better Ph.D. advisor.

I am also deeply grateful to my advisor, Dr. Nusinovich for his detailed and constructive advices and comments. His support throughout my research is very important to me.

Besides my advisors, I would like to warmly thank the rest of my committees, Professor Granatstein, Professor Murphy and Professor Hassam for their time spent on my thesis and their insightful comments and questions. I want to take this chance to thank Dr. Murphy for his kindly help when I just arrived Maryland.

I also thank Dr. Valsov for his comments and discussions, thank Dr. Sinitsyn, Ruifeng Pu, Ran Yan, Wenxi Zhu, Dimitry Kashyn, Dr. Romero-Talamas and Aydin Cem Keser for the discussions on our Friday meetings, thank Dr. Palastro for his help. I also thank Dr. Thumm and his student Andreas Schlaich for answering my questions about their experiments. I thank my friend Changhan Zhong for helping me with Linux and c programming.

At the last, I thank my family: my parents, my parents in law, my husband and my son. I appreciate my parents Lijuan Kong and Zhiqiang Yu so much. They bore and raised me in a love environment, gave me endless encouragement and support. I owe my loving thanks to my husband Qin Zhong and my son Kairan Zhong for their

understanding, companionship and love. All my friends and my whole family turned my journal through graduate school into pleasure.

# Table of Contents

Table of Contents .....	ii
Chapter 1: Introduction .....	1
Chapter 2: Self-field in Planar Orotron .....	9
2.1 Background .....	9
2.2 Basic theory .....	10
2.3 Start oscillation condition including AC space charge .....	15
2.4 Results and analysis .....	21
2.5 Conclusions and future work .....	29
Chapter 3: Formulation of Backward wave excitation .....	30
3.1 Background .....	30
3.2 Formula of the backward wave excitation .....	34
3.2.1 Model Equations .....	34
3.2.2 Normalized equations far from cut-off frequency .....	41
3.3 Results and Analysis .....	46
3.3.1 Results by solving the normalized first order equations .....	46
3.3.2 Results by solving the second order equations .....	52
3.3.3 Boundary condition modifications to the model .....	56
3.4 Conclusions .....	69
Chapter 4: Velocity Spread and Space Charge Effect in Gyrotron Beams .....	71
4.1 CPI Gyrotron .....	72
4.2 Velocity Spread .....	81
4.3 Coupling to the Electrostatic Cyclotron Maser Instability .....	88
4.3.1 Motion Equation .....	89
4.3.2 Space-charge spatial growth .....	93
4.3.3 Results and analysis .....	95
4.4 Conclusions .....	104
Appendix A .....	105
Appendix B .....	109

References.....	112
-----------------	-----

This Table of Contents is automatically generated by MS Word, linked to the Heading formats used within the Chapter text.

## Chapter 1: Introduction

In the electro-magnetic spectrum, which has been widely used since the 1900's, THz radiation ( $3 \times 10^{11}$  Hz -  $3 \times 10^{12}$  Hz), occupies the region between microwave and far-infrared radiation. Similar to microwaves, THz radiation can penetrate dry, non-conducting and non-polar materials such as clothing, paper and plastics, and even non-polar organic objects. In dielectrics, its absorption depends on the polarity and the optical phonon resonance of the material. In the gas phase, most molecules have unique rotational or ro- vibrational spectra of the absorbing species. Thus many materials have unique spectral fingerprints in THz range, this gives THz radiation high selectivity in different materials. In addition, THz radiation is non-ionizing radiation, so it can be used for imaging and detecting without damaging the objects. All these advantages bring THz radiation potential applications in a wide range of fields such as packaging inspection, materials evaluations, biomedical engineering research and plasma physics. However THz is not suitable for communications, because it is strongly absorbed in the atmosphere.

Sources of THz radiation can be grouped into three categories. The first category is vacuum electronic devices such as gyrotrons and backward wave oscillators (BWOs). The second is lasers. Far infrared lasers, the quantum cascade laser and the photomixing source all can generate THz radiation. The last category is solid-state sources. It includes the surface emitter, photoconductive emitters and the optical rectifiers, all of which are used in Terahertz time-domain spectroscopy. Our research focuses on vacuum electronic devices.

There are two basic mechanisms to generate THz waves in vacuum electronic devices: slow wave excitation and fast wave excitation. In slow wave devices, beam electrons travel along a straight path and interact with a wave whose phase velocity is below the speed of light. Radiation can be generated when the Cherenkov synchronism condition ( $v_p \approx v_e$ ) is satisfied, where  $v_p = \omega/k_z$  is the phase velocity of the wave,  $\omega$  and  $k_z$  are frequency and wave number, and  $v_e$  is the velocity of the electron. Cherenkov radiation occurs when  $v_p < v_e$ . The orotron is an example of a potential source of high power THz. In fast wave devices, such as the gyrotron, the beam electrons travel along a curved path and interact with a wave whose velocity is larger than the velocity of light. Radiation can be generated when the cyclotron synchronism condition  $\omega - k_z v_z \approx \Omega$ , is satisfied, where  $\Omega$  is the cyclotron resonance frequency.

The orotron was first proposed by Rusin and Bogomolov in 1966 [1]. It generates millimeter and sub-millimeter coherent radiation from the interaction between an electron beam and the electromagnetic field of a cavity containing a periodic grating. Near the grating surface, the field is a superposition of waves with wave numbers as  $k_{z,n} = k_{z,0} + n2\pi/p$ , where  $p$  is one period length of the grating surface. The orotron converts the spontaneous Smith-Purcell radiation [2] into stimulated radiation via the addition of a cavity. The dispersion diagram of the interaction between the electron beam and electromagnetic wave is shown in Fig. 1.1. The periodic curve indicates the dispersion curve of the field. The intercept is where the Cherenkov resonance occurs.

Figure 1.2 displays schematically the structure of an orotron consisting of a movable parabolic mirror and a fixed plane periodic grating. The upper mirror is

movable to generate different radiation frequencies. The lower mirror is a periodic grating surface to provide slow waves that will couple with the electron beam. Reviews of the orotron can be found in Refs. 3, 4 and 5. Reference 6 describes an example of the application of an orotron.

To produce higher power THz radiation from an orotron, higher beam current density will be needed. The self-fields in the beam, which resist the beam-wave interaction, will lower the efficiency of the orotron. To calculate the electron beam density needed to generate THz radiation, the self-field effects should be considered. We calculated start currents as function of various parameters. This is the essence of chapter 2.

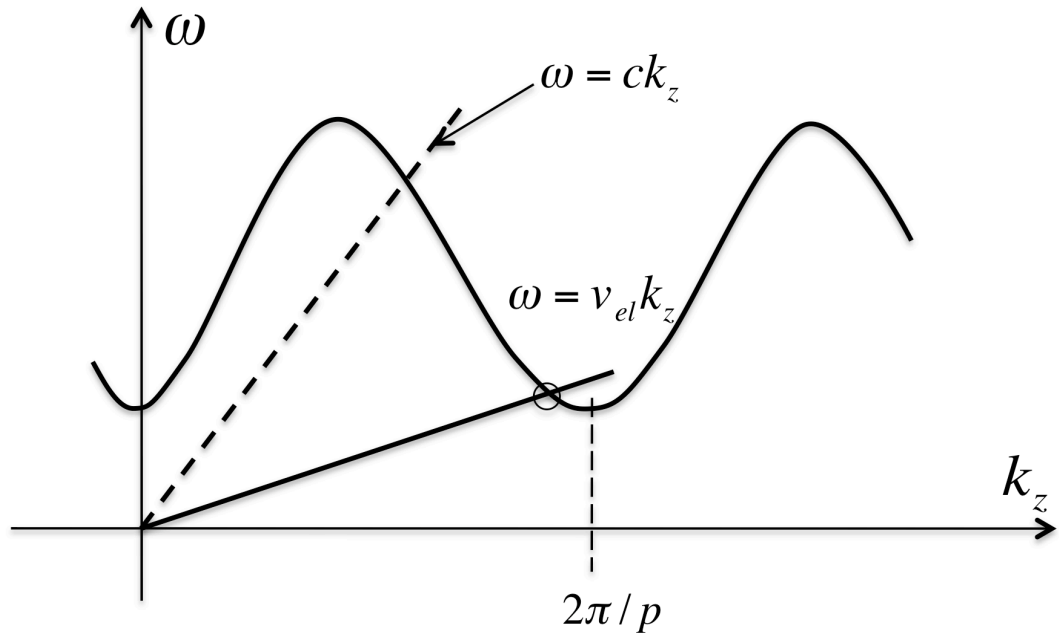


**Fig.1.1.** Dispersion diagram for the interaction between electron beam and electromagnetic wave in orotron.

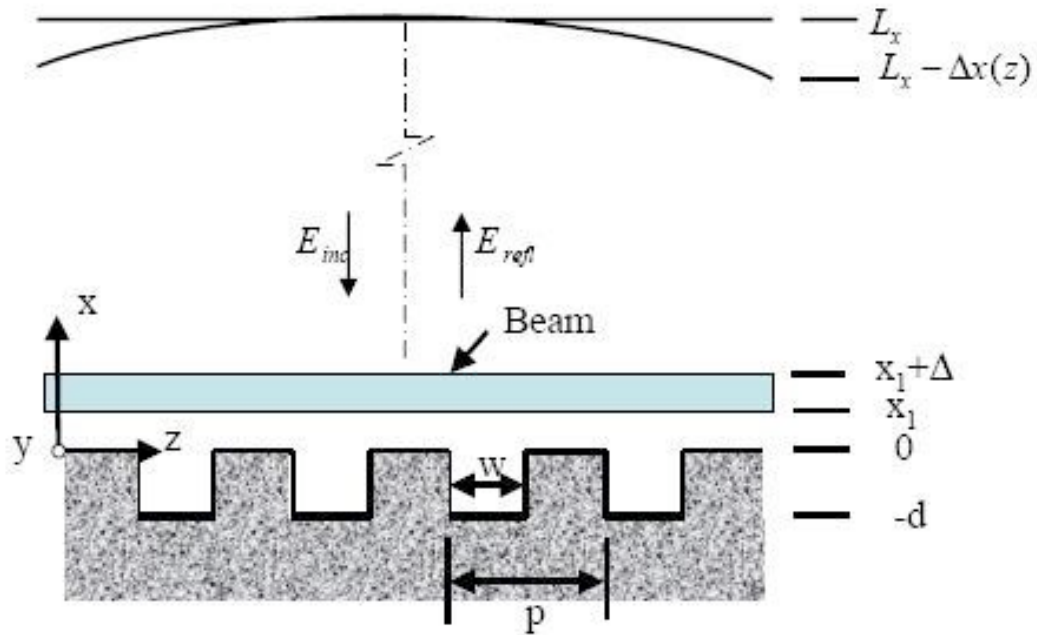


**Fig. 1.2.** Structure of a plane orotron ( $L_x \gg x_1 + \Delta + d$ )  
with rectangular grooves showing the important dimensions

The gyrotron [7] is based on mechanism of coherent cyclotron radiation. The theory was first developed by Richard Twiss in Australia [8], Jurgen Schneider in the US [9], and Andrei Gaponov of the U.S.S.R. [10] individually in the late 1950s. The structure of a gyrotron is shown in Fig. 1.3(a), and a cross section in the beam tunnel is shown in Fig. 1.3(b). An annular electron beam is accelerated from a cathode and gyrates in a small orbit around a magnetic field line towards a cavity. In the cavity, the electrons interact with an eigen-mode of the cavity and transform a part of their transverse kinetic energy to the wave. The electrons then leave the cavity and are collected on the right hand side.

Fig. 1.4 shows the dispersion diagram of the interaction between the electron beam and electromagnetic wave in the cavity of gyrotron. The curved line  $\omega = \sqrt{\omega_c^2 + c^2 k_z^2}$  is the dispersion diagram for the wave in the cavity, which can be regarded as a waveguide,  $\omega_c$  is the cutoff frequency. The intercepts indicate where the cyclotron resonances occur. Either backward wave (solid) or forward wave (dashed) oscillation can occur, which depends on relation between the cutoff frequency and the cyclotron frequency. If the cutoff frequency is larger than the cyclotron frequency, backward wave oscillation occurs, and the intercept is at negative  $k_z$ . If the cutoff frequency is smaller, forward wave oscillation occurs, the intercept is at positive  $k_z$ .

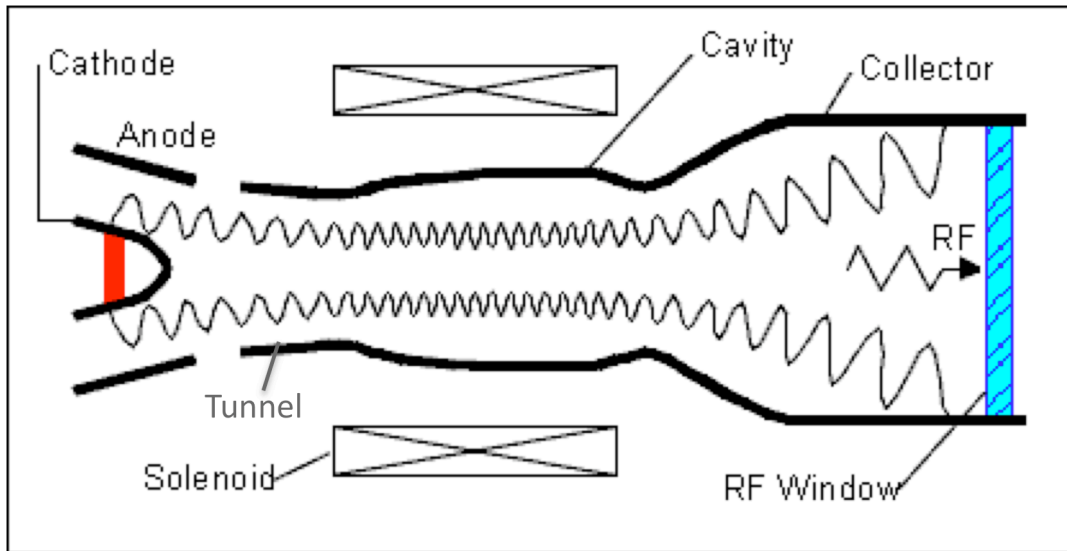


**Fig. 1.3 (a).** Gyrotron structure

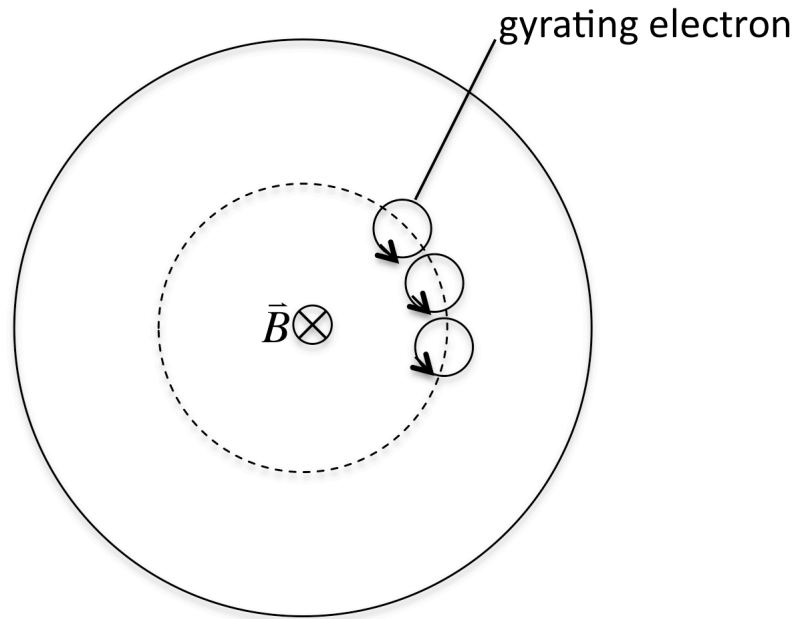


**Fig. 1.3 (b).** A cross section at the end of beam tunnel in gyrotron

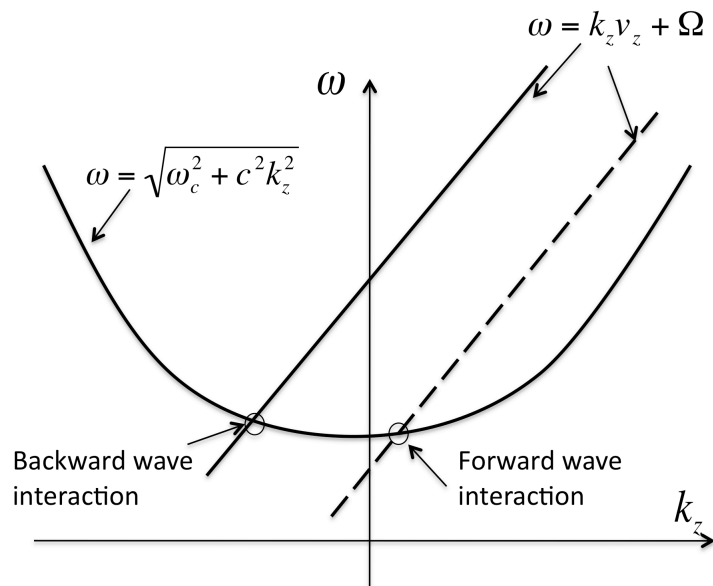


**Fig. 1.4.** Dispersion diagram for the interaction electron beam and electromagnetic wave in the cavity of gyrotron

The gyrotron as a generator of short-wavelength radiation has been well developed since 1960, when the fast-wave ECM (electron cyclotron maser) resonance (early gyrotron) was first experimentally verified in the U.S. and the U.S.S.R. (Refs. 7, 11, 12). Since then, high-power, long-pulse millimeter-wave gyrotrons have been ubiquitously used for electron cyclotron resonance plasma heating and current drive in many plasma installations (tokamaks and stellarators) at various laboratories around the world (see, e.g., Refs. 13-15). Also gyrotrons are used as a rapid heating tool in industry.

In the beam tunnel before the cavity of the gyrotron, the cyclotron resonance condition may also be satisfied. A backward wave can be excited in the tunnel, which will perturb the beam and significantly reduce the efficiency of the gyrotron. This excitation can be suppressed by putting some kind of absorbing material on the inner surface of the tunnel. We calculate the level of the surface impedance needed to suppress this excitation. This is the essence of chapter 3.

The rest of this research thesis is divided into three parts. In section 2, we discuss why we are concerned with the self-fields in orotrons, the basic theory of the orotron, how we include the AC space-charge effect in the start oscillation condition of an orotron, and some simulation results of how the start current varies with different parameters. In section 3, we discuss the backward wave excitation that happens in the beam tunnel of a gyrotron, how to suppress this excitation, the model equations describing the interaction between the electron beam and the EM wave in the gyrotron and some numerical results of the level of surface impedance needed to suppress the instability when only considering the backward wave excitation. In

section 4, we discussed how the velocity spread and space charge effect of the electron beam will affect the backward wave excitation in the beam tunnel of a gyrotron.

## Chapter 2: Self-field in Planar Orotron

### **2.1 Background**

For an orotron to emit stimulated radiation at high frequencies ( $f \sim 1$  THz), a sufficiently large beam current density must be injected. As a result, the effect of space charge has to be taken into consideration when analyzing the device's operation. One important effect is the generation of AC self fields [16]. The AC self fields of the electron beam act to resist the formation of bunches, and consequently the start current is raised. These fields become important at beam densities that are high enough such that the product of the effective beam plasma frequency ( $\omega_{p,eff}$ ) and the transit time for beam particles through the interaction region is of order of unity or greater,  $\omega_{p,eff}L_w/v_{z0} \geq 1$ . Here  $L_w$  is a measure of the interaction length and  $v_{z0}$  is the beam speed. Space charge effects in orotrons were analyzed in Refs. 17, 18 and 19. Basically, the interaction was considered to be with a space charge wave characterized by a single beam plasma frequency. In practice the effective beam plasma frequency is dependent on the presence of metallic surfaces near the beam. In general, a nearby metallic surface will lower the effective plasma frequency [20] from the value determined simply by the beam density,  $\omega_p^2 = 4\pi q^2 n/m$ , where  $q = -e$  is the electron charge,  $n$  is the beam density and  $m$  is the electron mass. Since the electron beam is very close to the grating surface in a high frequency orotron, we can expect that the plasma frequency will be modified in a significant way by the grating. A calculation of this effect is the subject of this thesis.

Two conditions that we investigate are the following. First, some portions of the beam will be much closer to the grating than others, and we can expect that the space charge effect will vary over the cross section of the beam. Second, the grating is not simply a planar conductor, and the geometry of the grooves will affect the space charge field. In particular, the self-fields penetrate to some degree into the grooves. Our analysis of this effect is accomplished by coupling a mode matching calculation of the fields in the grooves to a solution of the fields in the region of the beam.

## 2.2 Basic theory

To place our more detailed calculation in perspective, we first review the calculation of the start current in an orotron under the assumption that the self-fields of the beam are weak. The geometry we consider is shown in Figure 1.2. The beam is confined by a strong magnetic field such that only electron motion along the direction of propagation of the beam (the  $z$ -direction) is allowed, and the beam is planar (independent of  $y$ ). For this basic model we can take the fields in the region above the grating,  $x > 0$ , to have a spatial structure corresponding to a grating with period  $p = 2\pi / k_0$ ,

$$E_z(x, z, t) = \text{Re} \left\{ \int \frac{d\tilde{k}_z}{2\pi} \sum_n \bar{E}_{zn}(\tilde{k}_z, x) \exp \left[ i \left( (\tilde{k}_z + nk_0) z - \omega t \right) \right] \right\}, \quad (2.1a)$$

$$E_x(x, z, t) = \text{Re} \left\{ \int \frac{d\tilde{k}_z}{2\pi} \sum_n \bar{E}_{xn}(\tilde{k}_z, x) \exp \left[ i \left( (\tilde{k}_z + nk_0) z - \omega t \right) \right] \right\}, \quad (2.1b)$$

and

$$B_y(x, z, t) = \text{Re} \left\{ \int \frac{d\tilde{k}_z}{2\pi} \sum_n \bar{B}_{yn}(\tilde{k}_z, x) \exp \left[ i \left( (\tilde{k}_z + nk_0) z - \omega t \right) \right] \right\}. \quad (2.1c)$$

Here, the sum on  $n$  is over spatial harmonics of the field. We assume that the wave number dependence of the  $n=0$  term is determined by the shape and location of the curved mirror that confines the upper boundary of the cavity, and that higher spatial harmonic fields follow this dependence. For example, for a parabolic mirror with large radius of curvature, the spatial dependence of the field will be of the form  $\exp(-z^2 / L_w^2)$  where  $L_w$  is the half-width in  $z$  of the cavity mode. This leads to a wave number dependence of the transformed amplitudes of the form  $\exp(-\tilde{k}_z^2 L_w^2 / 4)$ . The  $x$  dependence of the fields is determined by the vacuum wave equation. We assume that the fundamental,  $n=0$ , spatial harmonic propagates in the  $x$  direction with wavenumbers  $\pm k_x = \pm \sqrt{\omega^2 / c^2 - \tilde{k}_z^2} \approx \pm \omega / c$ , and consists of a superposition of upward (reflected) and downward (incident) propagating waves.

$$\bar{E}_{z0}(\tilde{k}_z, x) = \bar{E}_{inc}(\tilde{k}_z) e^{-ik_x x} + \bar{E}_{refl}(\tilde{k}_z) e^{ik_x x}$$

The last approximation in the definition of  $k_x$  requires that the mode width satisfy  $\omega L_w / c \gg 1$ . In other words, the wavevector of the fundamental harmonic is predominately in the  $\pm x$ -direction. The other spatial harmonics are evanescent with spatial decay rate  $\kappa_n = \sqrt{(\tilde{k}_z + nk_0)^2 - \omega^2 / c^2} \approx |nk_0|$ . Here we have also assumed the first spatial harmonic approximately satisfies the Cherenkov resonance condition  $\omega \approx k_0 v_{z0}$ , where  $v_{z0}$  is the velocity of the injected electron beam. Then, for a nonrelativistic beam  $k_0 \gg \omega / c$ . The shape of the grating determines the relative amplitudes of the different spatial harmonics. In Appendix A we describe a mode matching solution that applies to the case of a grating consisting of rectangular

grooves. This solution will also be applied to our more detailed calculation to be presented subsequently.

The electrons are strongly coupled with the 1<sup>st</sup> spatial harmonic of the EM field. The energy,  $\varepsilon = mv_z^2 / 2$ , and axial position of beam electrons at transverse position  $x$  will then satisfy [21]:

$$\frac{d\varepsilon}{dt} = qv_z \operatorname{Re} \left\{ \int \frac{d\tilde{k}_z}{2\pi} \bar{E}_{z1}(\tilde{k}_z, x) e^{i(k_z z - \omega t)} \right\}, \quad (2.2a)$$

and

$$\frac{dz}{dt} = v_z(\varepsilon). \quad (2.2b)$$

where  $k_z = \tilde{k}_z + k_0$  is the wavenumber of the component of the field that strongly interacts with the beam. Here, we assume that electrons, with charge  $q$ , enter the interaction region uniformly distributed in time and with beam energy  $\varepsilon_b = mv_{z0}^2 / 2$ .

In this case the power extracted from the beam can be written as [4]

$$P_{ext} = \frac{q\omega}{4mv_{z0}^3} \int dx dy J_b(x) \frac{\partial}{\partial \tilde{k}_z} \left| \bar{E}_{z1}(\tilde{k}_z, x) \right|_{\tilde{k}_z = (\omega/v_{z0} - k_0)}^2, \quad (2.3)$$

where  $J_b(x)$  is the injected beam current density. For oscillations to start, the power must balance power lost in the cavity  $P_{lost} = \omega W / Q$  where  $W$  is the stored energy and  $Q$  is the quality factor. The stored energy can be written in terms of the incident wave amplitude for the  $n=0$  spatial harmonic in Eq. (2.1a), because typically the amplitude of this harmonic is much larger than amplitudes of other harmonics. The result for the lost power is

$$P_{lost} = \frac{\omega L_x}{4\pi Q} \int dy \int \frac{d\tilde{k}_z}{2\pi} \left| \bar{E}_{inc}(\tilde{k}_z) \right|^2, \quad (2.4)$$

where  $L_x$  is the separation between the grating and the curved mirror. Since losses occur primarily at the metallic surfaces of the mirror and grating we can express the quality factor in terms of the combined power reflection coefficient for the two surfaces,  $R$  (assumed to be close to unity), or the sum of the effective surface impedances for the two surfaces,

$$\frac{2\omega L_x}{cQ} = (1 - R) = 4 \operatorname{Re} \left( \frac{Z_{s1} + Z_{s2}}{Z_0} \right),$$

where  $Z_{s1,2}$  is the complex surface impedance of the mirror and grating, and  $Z_0$  is the impedance of free space. For a metallic surface with skin depth  $d_s$  we have  $\operatorname{Re}(Z_s / Z_0) = T\omega\delta_s / (2c)$ , where  $T$  is a factor that accounts for the geometry of the surface. For a flat surface  $T=1$ , and for a grooved surface  $T>1$ . Roughly  $T$  increases with the length of the surface per period [22]. This quantity is calculated in Appendix A for the case of rectangular grooves.

Forming the ratio of the two powers defined in Eqs. (2.3) and (2.4) we find that the minimum current density required to start oscillations in the cavity must satisfy

$$\text{Ratio} = \frac{P_{\text{ext}}}{P_{\text{lost}}} = \frac{g(\delta)}{4\beta_0^2(\delta_s/\lambda)} \left( \frac{\alpha^2}{1+T} \right) \int \frac{2k_0 dx J(x) L_w^2}{I_A} e^{-2k_0 x} > 1, \quad (2.5)$$

where  $\alpha^2 = |\bar{E}_{z1}(x=0)|^2 / |\bar{E}_{\text{inc}}|^2$  is a property of the grating that gives the strength of the  $n=1$  spatial harmonic in terms of the incident  $n=0$  wave,  $\beta_0 = v_{z0} / c$ ,  $\lambda = 2\pi c / \omega$ , is the vacuum wavelength,  $I_A = mc^3 / q$  and corresponds to  $1.7 \times 10^4$  Amperes, and  $L_w$  is a characteristic length of the interaction region. The dimensionless gain function  $g(\delta)$  is given by,

$$g(\delta) = L_w^{-2} \frac{\partial}{\partial \tilde{k}_z} \left| \bar{E}_{z1}(\tilde{k}_z, 0) \right|_{\tilde{k}_z = (\omega / v_{z0} - k_0)}^2 / \int \frac{d\tilde{k}_z}{2\pi} \left| \bar{E}_{inc}(\tilde{k}_z) \right|^2 = -(2\pi)^{1/2} \delta \exp(-\delta^2 / 2), \quad (2.6)$$

where  $\delta = L_w(\omega / v_{z0} - k_0)$  is the detuning from Cherenkov resonance normalized to the length of the interaction region. The second equality in (2.6) applies for the case of a parabolic reflecting mirror in which case the field profile has a  $z$ -dependence of the form  $\exp(-z^2 / L_w^2)$ . In the case of the Gaussian field profile gain function has a maximum value  $g_{max}=1.52$  occurring for detuning  $d=-1$  (see Ref. 21, for the case of a flat field profile).

Condition (2.5) can be rewritten as a condition on the current density, assuming it to be relatively constant in  $x$  over the distance  $(2k_0)^{-1}$

$$J[A/cm^2] > 0.039 \left[ \frac{1+T}{\alpha^2} \right] \frac{V[kV] f^{1/2}[THz]}{L_w^2[cm]}. \quad (2.7)$$

Here we assume the conductivity of the metal boundaries to be that of ideal copper, and the skin depth approximately to be  $\delta_s[cm] = 6.52 / f^{1/2}[Hz]$ . The optimum coupling occurs when the grooves are approximately a quarter wavelength deep. In this case,  $\alpha \approx 4/\pi$ . Also, with quarter wavelength depth grooves the factor  $T$  becomes essentially a function of voltage only. As voltage increases, the period of the structure must increase to maintain resonance, and  $T$  decreases. The factors describing the structure are well approximated by the formula:  $(1+T)/\alpha^2 \approx 45.5/(1+2.72V^{1/2}[kV])$ . The result is that for voltages above 1 kV Eq. (2.7) gives a  $V^{1/2}[kV]$  scaling of start current.

We note that condition (2.7) is based on gain from the beam exceeding losses in the wall. In practice we would like to couple power out of the cavity. Thus, the

quality-factor is lowered by the coupling. Finally, Eq. (2.7) represents the condition on current necessary to start oscillations. A higher current density is needed to reach an efficient nonlinear operation point [4, 23]. These last two effects plus effect of the surface roughness on the ohmic losses can be expected to increase the required current density by a factor of approximately 5-10.

Condition (2.7) is based on the interaction of the beam with the vacuum fields of the grating. It will be modified when the beam space charge is taken into consideration, and this effect will be studied in the remainder of the thesis.

### **2.3 Start oscillation condition including AC space charge**

We still assume that the beam interacts primarily with the first spatial harmonic of the grating field. The  $x$ -dependence of this spatial harmonic is no longer determined by the vacuum wave equation. Rather, it satisfies a wave equation that includes the dielectric response of the beam,

$$\frac{d}{dx} \left[ \varepsilon(x, \tilde{k}_z) \frac{d}{dx} \bar{E}_{z1} \right] - k_0^2 \varepsilon(x, \tilde{k}_z) \bar{E}_{z1} = 0, \quad (2.8)$$

where

$$\varepsilon(x, \tilde{k}_z) = 1 - \frac{\omega_p^2(x)}{\left[ \omega - (\tilde{k}_z + k_0)v_{z0} \right]^2}, \quad (2.9)$$

is the local beam dielectric constant. In writing (2.8) and (2.9) we have made a number of approximations and assumptions. First we have assumed that field is primarily electrostatic,  $\omega/(k_0 c) \approx \beta_0 \ll 1$ , and that the continuous wavenumber is small,  $|\tilde{k}_z| \ll k_0$ . This latter condition allows us to drop  $\tilde{k}_z$  except where it occurs in the Cherenkov resonance denominator. Finally, we have assumed that the beam is

confined by a focusing force that is linear in the displacement  $x$  of a beam particle from the  $y$ - $z$  plane, and that this force is exactly balanced by the DC self field in equilibrium. This situation could be realized in a periodic magnetic focusing field in the limit in which the period of the magnetic field  $\lambda_m$  is small:  $\lambda_m \ll 2\pi\Omega_\beta/v_{z0}$ . Generally, for small period, the period-averaged focusing force is proportional to the gradient of the square of the periodic field and hence is linear in displacement from the  $y$ - $z$  plane [24]. This linear focusing force gives rise, in the absence of self fields, to transverse oscillations of beam particles with betatron frequency  $\Omega_\beta$ , that is quadratic in magnetic field strength. If the focusing force balances the self field we have  $\omega_p = \Omega_\beta$  and the requirement on the period becomes  $\lambda_m \ll 2\pi\Omega_\beta/v_{z0} \leq L_w$ . Here the last inequality results from the requirement that AC space charge effects not be too strong. Thus, the requirement is that the period must be smaller than the interaction length. A second situation in which linear focusing is realized is with a solenoidal magnetic focusing field if the cathode is in field free region. In this case, by conservation of the  $y$ -component of canonical momentum, it can be shown that in the uniform field region the focusing force is linear in displacement and proportional to  $-m\Omega^2x$  where  $\Omega = qB/mc$  is the cyclotron frequency. Balancing this force against the self-field gives  $\omega_p^2 = \Omega^2$ . The required magnetic field strength to achieve this balance can be related to the current density,  $B[kG] = 0.18J^{1/2}[A/cm^2]/V^{1/4}[kV]$ , (often a safety factor is applied to this formula). The assumption of a linear focusing force results in the dielectric constant appearing twice in Eq. (2.8) describing the perpendicular and longitudinal response of the beam. In the case in which the beam is focused by a strong solenoidal magnetic field with immersed cathode ( $\omega_p^2 > \Omega^2$ ),

and motion in the x direction is suppressed, the first occurrence of the dielectric constant  $\epsilon$ , in Eq. (2.8) would be replaced by unity.

The main effect of the presence of the beam on the solution of Eq. (2.8) is that the field near the surface of the grating must now contain a mixture of the spatially growing and evanescent solutions,

$$\bar{E}_{z1} = \left( \bar{E}_{(-)} e^{-k_0 x} + r(\tilde{k}_z) \bar{E}_{(-)} e^{k_0 x} \right), \quad (2.10a)$$

$$\bar{B}_{y1} = \frac{i\omega}{k_0 c} \left( \bar{E}_{(-)} e^{-k_0 x} - r(\tilde{k}_z) \bar{E}_{(-)} e^{k_0 x} \right), \quad (2.10b)$$

Here  $r(\tilde{k}_z)$  describes the effect of the beam on the fields, with the vacuum case corresponding to  $r=0$ . If we take the beam to be of uniform density for  $x_1 < x < x_1 + \Delta$ , and of zero density otherwise, we arrive at the expression

$$r = \frac{1 - \epsilon^2}{1 + 2\epsilon Y_\Delta^{-1} + \epsilon^2} \exp(-2k_0 x_1)$$

where  $Y_\Delta = [1 - \exp(-2k_0 \Delta)] / [1 + \exp(-2k_0 \Delta)]$ .

We now wish to find the effect of the beam on the rate of growth of the cavity fields. That is we wish to relate the modification of the first spatial harmonic fields in Eqs.(2.10), back to the fundamental spatial harmonic fields which essentially describe the cavity mode fields. Realizing that the fundamental and first spatial harmonic fields are linearly related by the properties of the grating does this,

$$\bar{E}_{z0} \Big|_{x=0} = i \left( X_{00} \bar{B}_{y0} + X_{01} \bar{B}_{y1} \right)_{x=0}, \quad (2.11a)$$

and

$$\bar{E}_{z1} \Big|_{x=0} = i \left( X_{10} \bar{B}_{y0} + X_{11} \bar{B}_{y1} \right)_{x=0}. \quad (2.11b)$$

Here  $X_{ij}$  are the elements of a reactance matrix that are found by solving the vacuum Maxwell's equations for the fields in the grooves and for the fields above the grating for all spatial harmonics except the fundamental and the first. This calculation for a rectangular grooved grating is described in Appendix A. The matrix elements depend on the dimensions of the grating and the frequency of the radiation. They are properties of the vacuum structure. The relation between electric and magnetic first spatial harmonic fields is given in Eqs. (2.10). A similar equation can be written for the fundamental electric and magnetic fields,

$$\bar{E}_{z0} = \left( \bar{E}_{inc} e^{-ik_x x} + \rho(\tilde{k}_z) \bar{E}_{inc} e^{ik_x x} \right), \quad (2.12a)$$

$$\bar{B}_{y0} = \left( \bar{E}_{inc} e^{-ik_x x} - \rho(\tilde{k}_z) \bar{E}_{inc} e^{ik_x x} \right), \quad (2.12b)$$

where  $\rho(\tilde{k}_z)$  is the complex amplitude reflection coefficient for the grating, and we have assumed  $k_x c / \omega \approx 1$ .

Solving Eqs. (2.10-2.12), we arrive at an expression for the reflectivity of the grating including the effect of the beam,

$$\rho(\tilde{k}_z) = -\frac{1 - i(\hat{X} + \delta X)}{1 + i(\hat{X} + \delta X)}, \quad (2.13)$$

where

$$\hat{X} = X_{00} - \frac{X_{01} X_{10}}{[X_{11} + ck_0/\omega]}, \quad (2.14a)$$

$$\delta X = -X_{01} X_{10} \left\{ \left[ X_{11} + \frac{ck_0}{\omega} \left( \frac{1-r}{1+r} \right) \right]^{-1} - \left[ X_{11} + \frac{ck_0}{\omega} \right]^{-1} \right\}. \quad (2.14b)$$

The reflection coefficient for the grating including the effect of the beam can in principle have magnitude greater than unity describing the power extracted from the

beam. We write the reflection coefficient in the form  $\rho(\tilde{k}_z) = \exp[i\phi_0 + \eta(\tilde{k}_z)]$ , where  $\phi_0$  is the reflection phase in the limit of no beam ( $r=0$ ), and  $\eta(\tilde{k}_z)$  is the correction introduced by the interaction with the beam. In Appendix B we show that the start oscillation condition can be determined by balancing the reflection gain resulting from wave interaction with the beam against the reflection losses at the two metal surfaces, in a wavenumber averaged sense

$$\text{Re} \left\{ \int d\tilde{k}_z \left| \bar{E}_{inc}(\tilde{k}_z) \right|^2 \eta(\tilde{k}_z) \right\} \geq 2 \text{Re} \left\{ \frac{Z_{s1} + Z_{s2}}{Z_0} \right\} \int d\tilde{k}_z \left| \bar{E}_{inc}(\tilde{k}_z) \right|^2 \quad (2.15)$$

We can evaluate  $\eta$  in the limit in which the coupling between the fundamental and first spatial harmonic is weak,

$$\eta(\tilde{k}_z) = \frac{2i}{1 + X_{00}^2} X_{01} X_{10} \left\{ \left[ X_{11} + \frac{ck_0}{\omega} \frac{1+r}{1-r} \right]^{-1} - \left[ X_{11} + \frac{ck_0}{\omega} \right]^{-1} \right\}. \quad (2.16)$$

Using the definitions of  $r$  and  $\varepsilon$ , Eq. (2.16) can be seen to be the ratio of polynomials in  $\tilde{k}_z$ . All that is required in Eq. (2.15) is the real part of the integral, and this can be found from the residues of the poles of  $\eta$ . These correspond to the zeros of

$$\left[ X_{11} + \frac{ck_0}{\omega} \frac{1+r}{1-r} \right],$$

which is quadratic in  $\varepsilon$ . Thus, the zeros are determined by two solutions for  $\varepsilon$ , and as a result four solutions for  $\tilde{k}_z$ . The four solutions correspond to fast and slow surface space charge waves, one pair for each surface in the beam.

$$\tilde{k}_{z1,2} = \frac{\omega}{v_{z0}} \pm \frac{\omega_p}{v_{z0}} \frac{1}{\sqrt{1 - \varepsilon_+}}$$

$$\tilde{k}_{z3,4} = \frac{\omega}{v_{z0}} \pm \frac{\omega_p}{v_{z0}} \frac{1}{\sqrt{1 - \epsilon_-}}$$

Here

$$\epsilon_{\pm} = \frac{-(1 + Y_1)(1 + \zeta_1) \pm \sqrt{[(1 - Y_1)(1 - \zeta_1)]^2 + 4(1 - Y_{\Delta}^2)(1 + \zeta_1 Y_1)(Y_1 + \zeta_1)}}{2Y_{\Delta}(\zeta_1 + Y_1)} \quad (2.17)$$

where  $\zeta_1 = (\omega X_{11})/(ck_0)$  is in the range of  $[0, 2]$  by varying the depth and width of the grating, and  $Y_1 = [1 - \exp(-2k_0 x_1)]/[1 + \exp(-2k_0 x_1)]$ .

The factors  $\epsilon_{\pm}$  determine the space charge reduction factors for the space charge waves supported by the beam. The effect of the grating enters through the surface reactance  $X_{11}$ . The case of a planar conducting surface corresponds to  $\zeta_1 = 0$  ( $X_{11} = 0$ ). In the limit in which the beam is thick,  $Y_{\Delta} \rightarrow 1$ , the two solutions can be found simply,  $\epsilon_{+} = -1$  and  $\epsilon_{-} = -(1 + Y_1 \zeta_1)/(Y_1 + \zeta_1)$ . These correspond to surface waves on the lower and upper edges of the beam respectively. Plots of the reduction factors [16]

$$r_{sc,\pm} = (1 - \epsilon_{\pm})^{-1/2}, \quad (2.18)$$

versus beam width appear in Figure 2.1. We note that for beams satisfying  $k_0 \Delta > 1$  the reduction factor falls in a relatively narrow range  $0.6 < r_{sc} < 0.9$ .

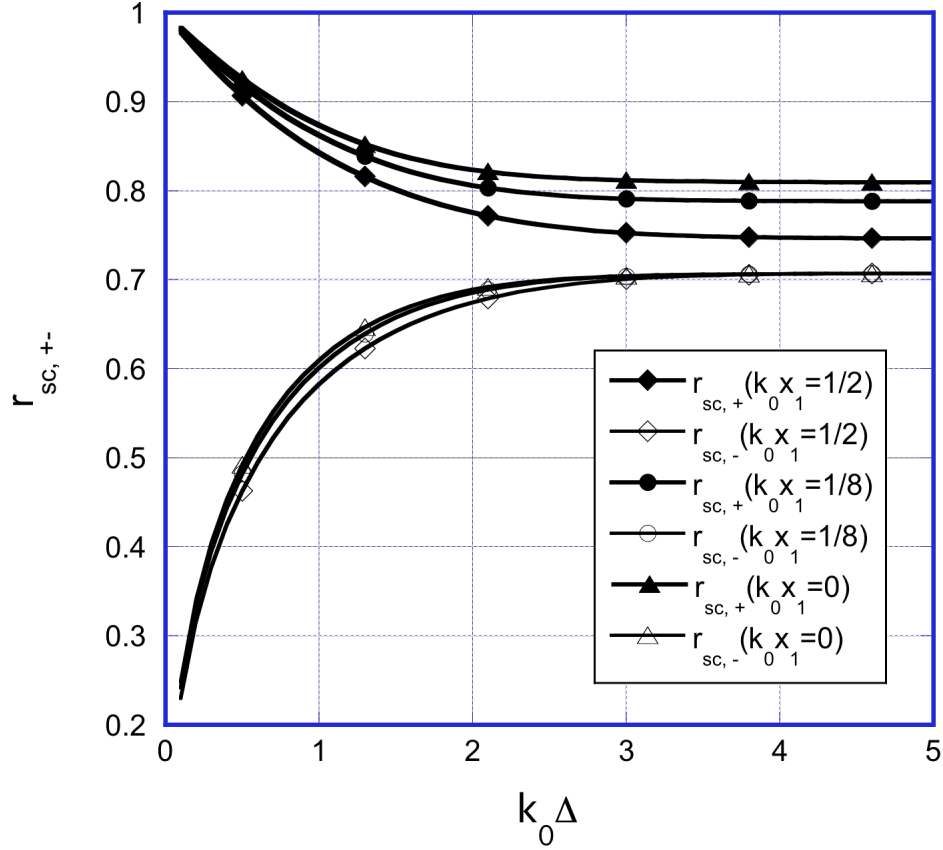


**Fig. 2.1.** Space-Charge Factor ( $r_{sc}$ ) (defined in Eqs. (2.17) and (2.18)) as function of beam width ( $k_0\Delta$ ) for different fixed  $k_0x_1 = 0, 1/8, 1/2$  when  $V_b=3$  kV

## **2.4 Results and analysis**

In this section, we evaluate the start current numerically by evaluating the left and right hand sides of Eq. (2.15). In particular, we define the *Ratio* to be the left hand side divided by the right hand side. This ratio represents the amount of gain relative to wall losses. If wall losses are the only source of losses, oscillations start when

$Ratio > 1$ . We will plot curves for the amount of current needed to reach several values of  $Ratio$ . In this way one can consider the effect of other sources of loss, as well as the requirement to reach a sufficiently large nonlinear oscillation.

We first consider an orotron operating at  $f=0.5$  THz, the half-width of the interaction length is  $L_w=0.5$  cm, and the walls are considered to be ideal copper. The width and depth of the grating surface are half of the period of the grating and a quarter of the wavelength, respectively. (Details are in Appendix A.) The electron beam is considered to be broad ( $k_0\Delta \gg 1$ ), and close to the grating surface ( $k_0x_1 \ll 1$ ). This situation can be expected to produce the lowest start current density values.

Figure 2.2 shows the current density required to produce  $Ratio$ -values of 1, 5, and 10 as predicted by the simple theory, and the theory including self-fields and transverse motion. The simple theory curves are well represented by Eq. (2.7) with the voltage dependent expression  $(1+T)/\alpha^2 \approx 45.5/(1+2.72V^{1/2}[kV])$ . At high voltages the effect of self-fields is unimportant and the simple theory, which assumes infinitely strong confining field gives a start current value that is about twice that of the theory that includes transverse motion. This is because the gain in the latter case includes the effect of both longitudinal and transverse bunching. At lower voltages the effect of space charge becomes more important. As can be seen, depending on the  $Ratio$ -value, there is an optimum voltage where the start current is minimized. This is consistent with the previous studies of Ref. 17 and 18.

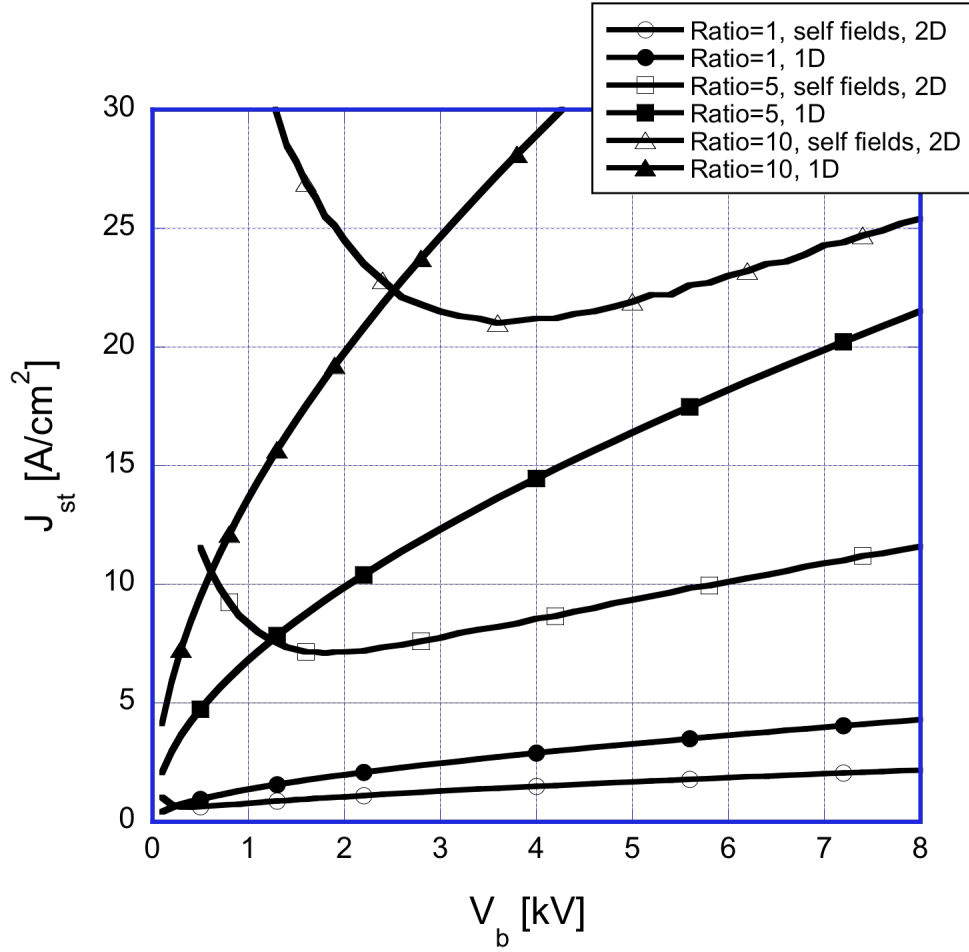


**Fig. 2.2.** Plot of start current density ( $J_{st}$ ) versus beam voltage ( $V_b$ ) for copper-wall devices producing radiation at  $f=0.5$  THz. The curves with solid symbols correspond to the simple, one-dimensional model with no self-fields. The curves with open symbols correspond to the theory including two-dimensional motion and self-fields.

In Figure 2.3 we show the same data for a longer interaction length ( $L_w=2.0$  cm), compared with the case ( $L_w=0.5$  cm). As expected the start current values are substantially lower. Two factors need to be kept in mind. The first is that the

efficiency tends to drop as the interaction length increases. Phase trapping arguments indicate that saturated efficiency should scale as the reciprocal of the number of the grating periods. Further, the alignment and transport of the beam become more critical as the interaction length increases. Because of the exponential dependence of the first spatial harmonic field on distance from the grating, the useful thickness of the beam is a small fraction of the period. Maintaining this distance from the grating for several centimeters will be a technological challenge. Also, operation of the orotron with a longer interaction space is more sensitive to electron velocity spread [23].

In Figure 2.4, the interaction length is fixed ( $L_w=0.5$  cm), and start current density is plotted as a function of the operating frequency ( $f$ ) for different values of beam voltage ( $V_b$ ). The frequency varies in the range from 0.2 to 2 THz, and the beam voltage is set to be 3kV and 10 kV. As shown, start-current density increases when frequency gets higher. From Figure 2.3, we know that when  $V_b=3$ kV the space-charge effect plays an important role, but it does not at  $V_b=10$  kV. Comparing the plots for  $Ratio=10$ , we can see that at higher frequencies self field effects play a more important role, which explains why the start current for  $V_b=3$  kV is larger than that for  $V_b=10$  kV.

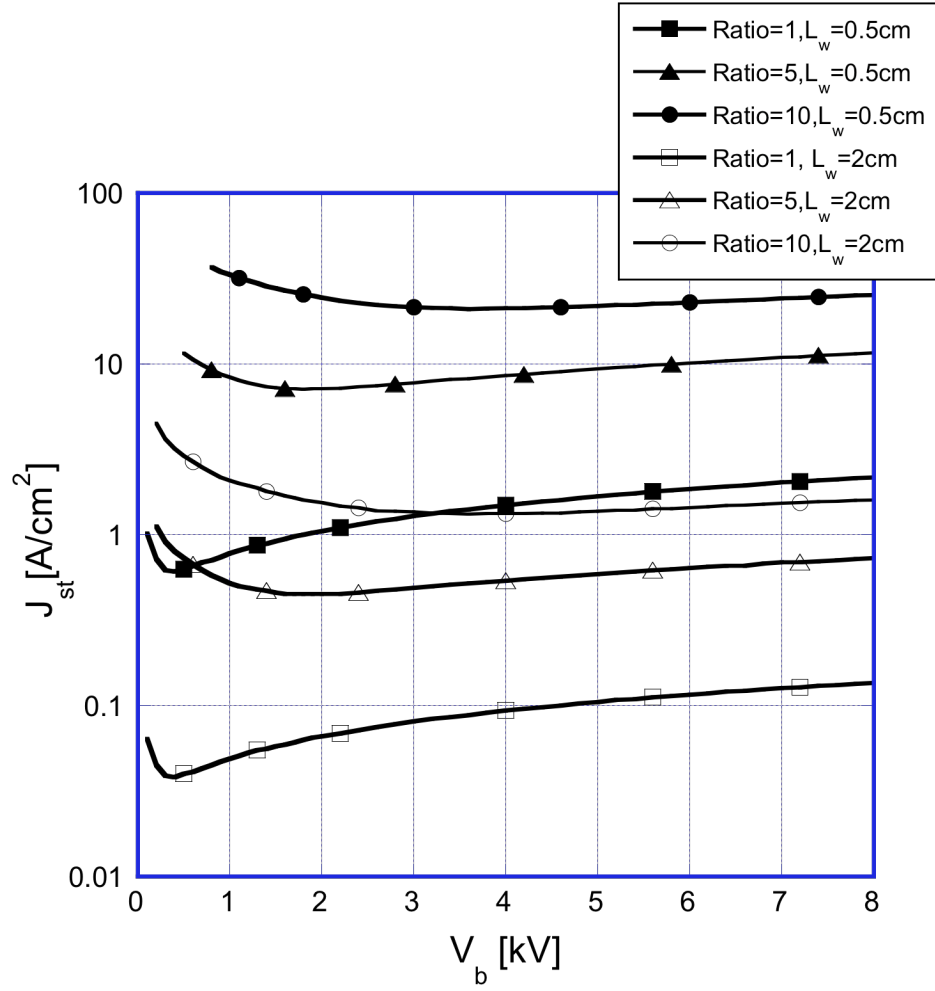


**Fig. 2.3.**  $J_{st}$  versus  $V_b$  for the theory includes two-dimensional motion and self-fields when  $L_w=2$ cm and  $L_w=0.5$  cm. The radiation frequency is kept at  $f=0.5$  THz.

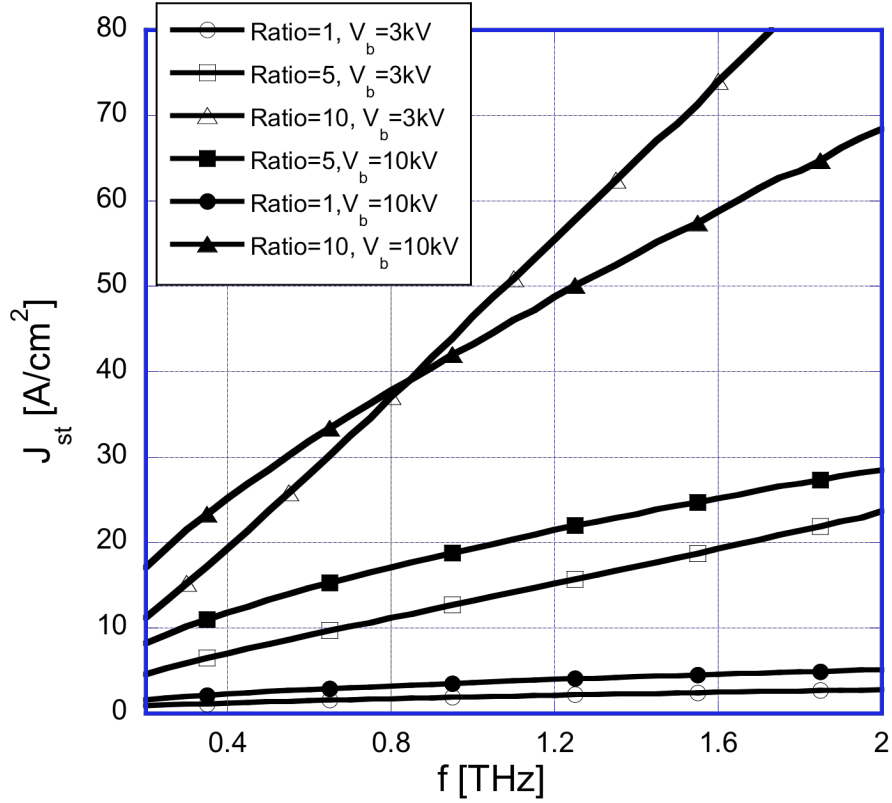


**Fig. 2.4.**  $J_{st}$  versus  $f$  [0.2 THz-2 THz] with  $L_w=0.5$  cm fixed and voltages 3 kV and 10 kV.

Figure 2.5 shows the effect caused by varying the width of the beam ( $\Delta$ ) and the distance between the beam and the grating surface ( $x_l$ ). For instance, let  $k_0\Delta = 1$ ,  $k_0x_l = 1/8$ . The interaction length is again  $L_w=0.5$  cm, with radiation frequency at  $f=0.5$  THz. We see that the start current increases with beam-grating distance and decreases with beam width. The first relation comes from the exponential decay of the field away from grating surface. The second relation is because the absorption of

the incident and reflected waves by the beam increases as the beam gets wider, which will cause the absorption drop.

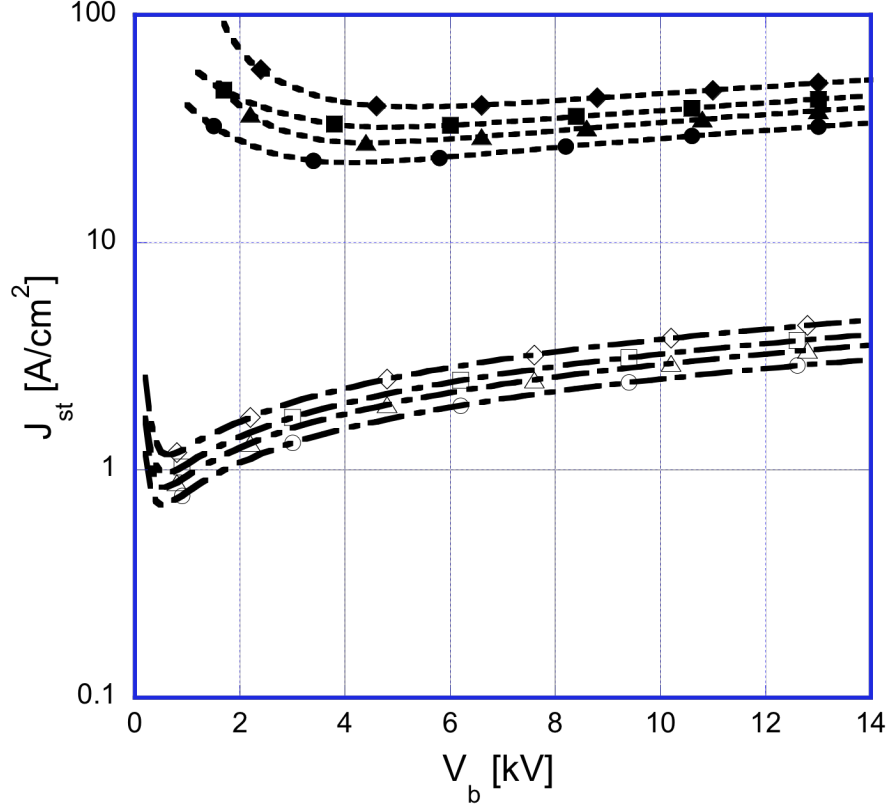


**Fig. 2.5.**  $J_{st}$  versus  $V_b$ , when  $L_w=0.5$  cm,  $f=0.5$  THz. The upper dashed lines are for Ratio=10, and the lower solid ones corresponds to Ratio=1. For both sets of plots, from circle to diamond marked (upward) the lines in turn correspond to  $k_0\Delta = \infty$ ,

$$k_0x_1 = 0; k_0\Delta = \infty, k_0x_1 = 1/8; k_0\Delta = 1, k_0x_1 = 0; k_0\Delta = 1, k_0x_1 = 1/8.$$

We compare our calculated start currents with the experimental results of Ref. 4, for a set of applied beam voltages and frequencies (between 60 GHz and 70 GHz) in

Table 1. Here the period of the grating is fixed to be 0.43 mm, the depth and width of each groove is 0.88 mm and 0.15 mm; the size of injected electron beam is 10 mm×0.3 mm. The cavity mode dimensions are 10 mm in length, 20 mm in height, and the quality factor  $Q= 5000$ . In this device, there was a strong confining solenoidal magnetic field, so the simple, one-dimension theory should be more appropriate. Further, the beam had an estimated 1% energy spread, which would reduce gain for a structure such as this one with 25 grating periods. The observed start currents are about five times that predicted by the one-dimension theory based on a cold beam. (See column 3 of Table 1.) The authors of Ref. 4 attribute some of the difference to beam energy spread. However, we note that the interaction is very sensitive to the  $x_1$ -the distance between the beam and the grating. The results of Table 1 are for  $x_1 = 0$ , (i.e. the beam touches the grating). If we increase  $x_1$  to a value  $x_1=0.06$  mm, then the simple theory gives a start current that is comparable to the measured value. In any event, our calculations show that for this low frequency device, self -field effects do not play an important role. However, at frequencies in the THz region, self-field effects are important.

V ( KV )	f (GHz)	Ist/2(mA) simple	Ist (mA) Self-field	Ist10(mA) Self-field	Is(mA) experiment
2.008	60.76	4.3	4.5	44.7	68
2.14	62.75	4.4	4.5	45	75
2.35	65.85	4.4	4.5	45.6	78
2.44	66.92	4.5	4.8	46.2	58
2.471	67.46	4.5	4.8	46.2	70
2.74	70.76	4.7	4.8	47.7	82

**Table 1** Calculated and experimental start currents [4] for a set of beam voltages and frequencies

## **2.5 Conclusions and future work**

The start current for an orotron is affected by the AC self fields of the electron beam. These fields can be thought of as space-charge waves on the beam. The frequency of the space-charge waves is affected by the geometry of the beam and the location of the nearby grating. We have calculated the start current as function of various parameters. Our general finding, which is in qualitative agreement with the previous theories [17, 18], is that the self fields lead to an optimum voltage at which start current is minimum. This optimum voltage is in the range of 2-6 kV for generation at THz frequencies.

## Chapter 3: Formulation of Backward wave excitation

### 3.1 Background

High-power, long-pulse millimeter-wave gyrotrons are used for electron cyclotron resonance plasma heating and current drive in many plasma installations (tokamaks and stellarators) at various laboratories around the globe (see, e.g., Refs. 13-15). One of the problems hindering efficient operation of these gyrotrons is excitation of spurious backward waves in beam tunnels. Such excitation, and resulting lower gyrotron efficiency, has been observed in a number of experiments (see, e.g., Refs. 25 and 26).

The beam tunnel is the region between the electron gun and the cavity and is schematically shown in Fig. 3.1. Here backward waves may be excited in the region between two planes denoted in Fig. 3.1 by  $z=z_o$  and  $z=z_s$ . The excitation takes place when the resonance condition between the cyclotron frequency of electrons and the Doppler-shifted wave frequency is satisfied. For the resonance at the fundamental cyclotron harmonic, this condition can be written as

$$\omega - k_z v_z \approx \Omega/\gamma \quad (3.1)$$

In Eq. (3.1),  $\omega$  and  $k_z$  are the wave frequency and axial wave number of a  $TE_{m,p}$  mode, respectively,  $v_z$  is the electron axial velocity,  $\Omega_0 = qB_0/mc$  is the nonrelativistic cyclotron frequency,  $q$  and  $m$  are the electron charge and mass and  $B_0$  is the strength of the magnetic field,  $\gamma = (1 - v^2/c^2)^{-1/2}$  is the relativistic factor,  $v$  is the electron speed,  $c$  is the speed of light. The axial wave number is given by  $k_z = \pm \sqrt{\omega^2 - \omega_c^2}/c$ , where the cut-off frequency is  $\omega_c = c j'_{m,p}/R(z)$ , here  $j'_{m,p}$  is the  $p$ -

th zero of the derivative of the  $m$ -th Bessel function and  $R(z)$  is the wall radius, and the  $\pm$  sign denotes whether the wave is forward (+) or backward (-).

In the beam tunnel region shown in Fig. 3.1 a number of the quantities in Eq. (3.1) vary with axial distance. The axial dependence of the wall radius makes the cutoff frequency axially dependent. As a consequence, the axial wave number varies in  $z$  as well. Also, the axial tapering of the external magnetic field  $B_0(z)$  not only changes the electron cyclotron frequency, but also affects the electron axial velocity, because the electron orbital momentum  $p_{\perp}$  varies in accordance with the invariant  $p_{\perp}^2/B = \text{const}$  [12]. Thus, all quantities except for  $\omega$  in Eq. (3.1) vary with axial distance.

The dispersion curves for the waveguide mode and the Doppler shifted cyclotron frequency are shown in Fig. 3.2 for two axial positions in the beam tunnel. The intersections of the two curves satisfy Eq. (3.1). At the plane  $z=z_1$  (Fig. 3.2 (a)) the cyclotron resonance interaction takes place at frequencies far from cutoff, while at the plane  $z=z_2$  (Fig. 3.2(b)) the wave frequency is close to the cutoff. When the wave is excited near the cutoff frequency, it is necessary to take into account the electron beam interaction with both forward and backward wave components of the excited electromagnetic field because the axial wave number (and hence the Doppler term) in this case are small. Then, the wave excitation in the framework of the linear theory in an untapered configuration can be described by a fourth-order dispersion equation with proper boundary conditions [27]. In contrast, in the case of wave excitation far from cutoff, the Doppler term is significant, so the interaction with the forward wave component of an electromagnetic field has a non-resonant nature and, hence, can be

neglected that reduces the problem to the cubic dispersion equation [27-31]. As shown in Ref. 28 (see also references therein), under certain conditions, this dispersion equation can be reduced to the cubic dispersion equation derived for linear-beam traveling-wave devices by J. Pierce [32] whose study for the case of backward waves was performed by H. Johnson [33].

The effect of tapered parameters on the operation of gyro-devices has been investigated in a number of contexts. Previous studies of tapering have focused on the effects on start conditions and efficiency of relatively weak tapering in magnetic field and wall radius in gyro-oscillators [34] and gyro-BWO's [35]. By "weak" we mean that the relative spatial variation of the cyclotron frequency or Doppler shift is much less than unity. The effect of strong tapering of wall radius and magnetic field on gain and bandwidth of gyro-amplifiers was considered in Ref. 36, while the effect of strong tapering on the electrostatic cyclotron instability was considered in Ref. 37. The effect of wall radius tapering on the nonstationary behavior of gyro-BWO's was considered in Ref. 38. In this case, wall radius tapering at the end of the gyro-BWO induced a reflection launching a forward wave which modified the nonlinear behavior of the oscillator. In contrast, in our present analysis the wall radius tapering is gradual and does not induce strong reflections. On the other hand, the wall tapering is strong in the sense that the axial wave number of the waveguide mode becomes large enough to make the Doppler shift frequency comparable to the mode frequency. The tapering of the magnetic field is strong in the same sense, viz, changes the cyclotron frequency are comparable to the wave frequency. Generally these changes serve to define an interaction length and hence determine the start current.

In what follows we present a small-signal theory describing the self-excitation conditions for backward waves in beam tunnels of the type shown in Fig. 3.1 whose walls can be covered with a lossy dielectric for suppressing these backward waves. Section II contains the formulation of the problem. There, a general set of equations is given for the excitation of the gyro-BWO in a beam tunnel having tapered parameters. In Section 3.3 we present results of numerical studies of solution of the equations and determine the amount of attenuation in the tunnel walls needed to suppress the backward waves. The results are discussed and the requirements on lossy materials necessary for suppressing unwanted backward waves are given. Section 3.4 contains a summary and discussion of modifications to the theory that may affect the predictions.

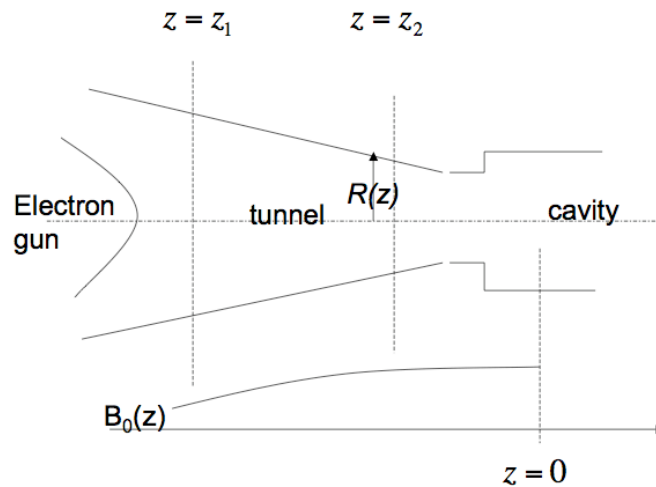


**Fig. 3.1.** Structure of the beam tunnel of gyrotron

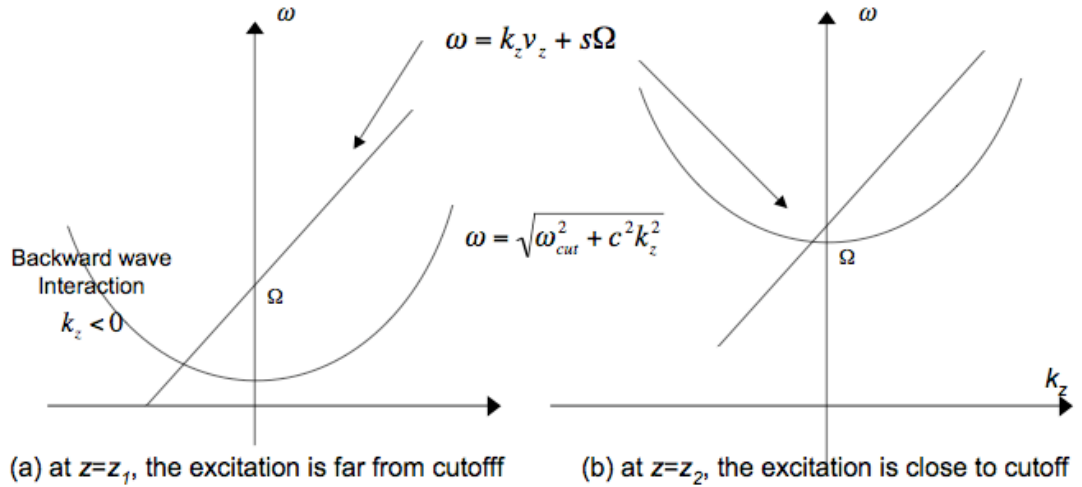


**Fig. 3.2.** Dispersion diagram of forward and back ward wave interaction when the excitations are far away (a) and close to (b) the cutoff.

### 3.2 Formula of the backward wave excitation

In general, to describe the excitation of electromagnetic waves by an electron beam one needs equations for electron motion and equations for excitation of the electromagnetic field. We use both second order non-normalized differential equation set Eqs (3.9) and first order normalized differential equation set Eqs. (3.13) for each the case, when the excitation is close to and far from the cutoff.

#### **3.2.1 Model Equations**

In general, to describe the excitation of electromagnetic waves by an electron beam one needs equations for electron motion and equations for excitation of the electromagnetic field. For the field equations we use the generalized telegraphist's equations [39], in which Maxwell's equations are recast in the form of a set of equations for voltages and currents on a coupled set of transmission lines. Here we

include the perturbed beam current and use the generalized telegraphist's equation that describe the effect of the electron beam on the electromagnetic wave. Following Ref. 40 we use electrostatic units (esu-Gaussian) to express Maxwell's Equations. Assume the electromagnetic field can be written as

$$E(r,t) = \Re\{(E_T(r,t) + E_z(r,t)\hat{z})\exp(-i\omega t)\}, \quad (3.2a)$$

$$B(r,t) = \Re\{(B_T(r,t) + B_z(r,t)\hat{z})\exp(-i\omega t)\}, \quad (3.2b)$$

where  $\vec{E}_T$  and  $\vec{B}_T$  are the transverse fields, and  $E_z$  and  $B_z$  are longitude components. The transverse components of electromagnetic field can be written as a sum over waveguide modes as,

$$E_T = \sum_k V_k(z,t)e_k(r_T,z) \quad (3.3a)$$

$$B_T = \sum_k I_k(z,t)b_k(r_T,z) \quad (3.3b)$$

where  $V_k$ ,  $I_k$  are the complex voltage and current amplitudes.  $\vec{e}_k$  and  $\vec{b}_k$  are the eigenmodes of a waveguide with the local radius of the beam tunnel. The subscript  $k$  here denotes the mode. In our case,  $k$  stands for a combination of (m,p) for mode  $TE_{mp}$ . From Maxwell's equation, we write the generalized telegraphist's equations for the TE modes as:

$$\frac{2}{c} \frac{\partial V_k}{\partial t} = \Gamma_k V_k - \frac{\partial I_k}{\partial z} - S_{Tk} \quad (3.4a)$$

$$ik_0 I_k = \frac{\partial V_k}{\partial z}. \quad (3.4b)$$

where  $S_{Tk} = (4\pi/c) \int \vec{J}_T \cdot \vec{e}_k^* da$ , in which the integral is over cross section of the beam tunnel,  $\vec{J}_T$  is the transverse current density at frequency  $\omega$ , and  $k_0 = \omega/c$ . In the

quantity  $\Gamma_k = ik_0(1 - k_k^2/k_0^2)$  both the real and imaginary parts of  $k_k = \omega_c/c + ik_i$  vary with  $z$ . The imaginary part  $k_i$  is a consequence of the finite conductivity of a lossy material applied on the inner surface of the beam tunnel. In writing Eqs.(3.4) we have neglected the coupling between modes under the assumption that the wall radius is gradually tapered.

From the relativistic motion equation of an electron

$$\frac{d\vec{p}}{dt} = q \left( E(\vec{r}, t) + \frac{\vec{v}}{c} \times B(\vec{r}, t) \right) + \frac{q}{c} \vec{v} \times \vec{B}_0, \quad (3.5)$$

where  $\vec{p} = \gamma m \vec{v}$  is the relativistic momentum of electron,  $\vec{v}$  is the velocity of the injected electron,  $\vec{B}_0$  is the external guiding magnetic field, we can obtain the following equations for electron motion in the preserve of a TE mode in the beam tunnel [40]:

$$\frac{\partial(\gamma\beta_\perp)}{\partial z} = \frac{1}{\beta_z} \Re \left\{ (\gamma\beta_\perp)^{s-1} \exp(-is\phi) \times \sum (V_k - \beta_z I_k) F_{\perp ks} \right\} + \frac{\gamma\beta_\perp}{2} \frac{\partial \ln B_0}{\partial z}, \quad (3.6a)$$

$$\frac{\partial \phi}{\partial z} = \frac{1}{\beta_z} \left( \frac{k_0}{s} - \frac{\Omega_0}{\gamma c} \right) + \frac{1}{\gamma\beta_z\beta_\perp} \times \Im \left\{ (\gamma\beta_\perp)^{s-1} \exp(-is\phi) \sum (V_k - \beta_z I_k) F_{\perp ks} \right\}, \quad (3.6b)$$

$$\frac{\partial(\gamma\beta_z)}{\partial z} = -\frac{\gamma\beta_\perp^2}{2\beta_z} \frac{\partial \ln B_0}{\partial z}. \quad (3.6c)$$

In Eqs.(3.6)  $V_k$  and  $I_k$  are normalized to  $q/mc^2$ ,  $\phi = \xi + \omega t/s + \theta_0$ ,  $\xi$  is the gyro-phase, i.e. the velocity of electron can be written as  $\vec{v} = v_\perp (\vec{x} \cos \xi + \vec{y} \sin \xi) + v_z \vec{z}$ , and  $F_{\perp ks}$  is the coupling coefficient between the electromagnetic fields and electrons, defined as

$$F_{\perp ks} = F_{\perp m, p} = -c_{m, p} k_{m, p} e^{i(m+1)\theta_0} J_{m+1}(k_{m, p} x_0) \frac{1}{2} e^{i\frac{\pi}{2}},$$

where  $x_0$  and  $\theta_0$  are the guiding center radius and azimuth, and

$$c_{m,p} = \frac{1}{\sqrt{\pi(j_{m,p}'^2 - m^2)} J_m(j_{m,p}')}. \quad (3.6)$$

Then the  $S_{Tk}$  in Eq. (3.4) can be written as

$$S_{Tk} = 8\pi(I/I_A)F_{\perp ks}^* \langle (\gamma\beta_{\perp} \exp(i\phi))^s / (\gamma\beta_z) \rangle, \quad (3.7)$$

where  $I_A = mc^3/q$  and corresponds to  $1.7 \times 10^4$  Amperes. The average on the right hand side of Eq. (3.7) is over electron trajectories. Also for TE modes in Eq. (6a)-(6b)  $\beta_k I_k$  is much smaller than  $V_k$ , so it can be omitted.

To simplify this set of equations, we define  $\gamma\beta_{\perp} = R_B^{1/2} \rho_{\perp}$ , where  $\gamma = ((\gamma\beta_{\perp})^2 + (\gamma\beta_z)^2)^{1/2} + 1$  and  $R_B(z) = B_0(z)/B_{0\max}$ . We also assume, consistent with our use of Eqs.(3.4), that the transverse fields in Eq. (3.3) are dominated by a single mode. We obtain a new set of equations for new variables  $\rho_{\perp}$ ,  $\gamma$  and  $\phi$  for a specific mode as follows:

$$\frac{\partial \rho_{\perp}}{\partial z} = \frac{\gamma \rho_{\perp}^{(s-1)} R_B^{s/2-1}}{\rho_z} \Re \{ F_{\perp ks} V_k \exp(-is\phi) \}, \quad (3.8a)$$

$$\frac{\partial \gamma}{\partial z} = \frac{\gamma \rho_{\perp}^s R_B^{s/2}}{\rho_z} \Re \{ F_{\perp ks} V_k \exp(-is\phi) \}, \quad (3.8b)$$

$$\frac{\partial \phi}{\partial z} = \frac{1}{\rho_z} \left( \frac{\gamma k_0}{s} - \frac{\Omega_0}{c} \right) + \frac{\gamma \rho_{\perp}^{s-2} R_B^{s/2-1}}{\rho_z} \Im \{ F_{\perp ks} V_k \exp(-is\phi) \}. \quad (3.8c)$$

where  $\rho_z(\gamma, \rho_{\perp}, z) \cong \sqrt{2(\gamma-1) - \rho_{\perp}^2 R_B}$ , which is a good approximation when the beam voltage ( $V_b$ ) is low ( $V_b \ll 511\text{KV}$ ).

Equations (3.8a)-(3.8c) and Eqs.(3.4a) and (3.4b) constitute a nonlinear, self-consistent set that describes excitation of modes in the beam tunnel by the electron

beam. To solve this equation set, we need boundary conditions, which for electrons are initial values describing the injected electron  $\rho_{\perp}(z_o) = \rho_{\perp 0}$ ,  $\gamma(z_o) = \gamma_0$ ,  $\phi(z_o) = \phi_{00}$ . Also, we will assume that the interaction takes place between  $z_o$  and  $z_s$ , and that the wave excited in this region satisfies outgoing conditions at these points:  $dV_k/dz|_{z=z_o} = ik_z(z_o)V_k(z_o)$ , and  $dV_k/dz|_{z=z_s} = ik_z(z_s)V_k(z_s)$ . Here  $k_z(z_o)$  represent the wave number of a backward wave at  $z_o$  ( $k_z(z_o) < 0$ ), and  $k_z(z_s)$  represent the wave number of a forward wave ( $k_z(z_s) > 0$ ) or an evanescent wave at  $z = z_s$ .

Using the small signal model, we write  $\rho_{\perp} = \rho_{\perp 0} + \delta\rho_{\perp}$ ,  $\gamma = \gamma_0 + \delta\gamma$  and  $\phi = \phi_0 + \delta\phi$ , where quantities with a subscript zero apply to the case of no electromagnetic wave and  $(\delta\gamma, \delta\rho_{\perp}, \delta\phi)$  are the perturbations induced by the wave. We then obtain the following equations, for 0<sup>th</sup> order,  $\rho_{\perp 0} = const$ ,  $\gamma_0 = const$ , and

$$\frac{d\phi_0}{dz} = \frac{1}{\rho_{z0}} \left( \frac{\gamma_0 k_0}{s} - \frac{\Omega}{c} \right). \quad (3.9a)$$

For the 1<sup>st</sup> order, we obtain

$$\frac{\partial \delta\rho_{\perp}}{\partial z} = \frac{\gamma_0 \rho_{\perp 0}^{(s-1)} R_B^{s/2-1}}{\rho_{z0}} \Re \left\{ F_{\perp ks} \exp(-is\phi_0) V_k \right\}, \quad (3.9b)$$

$$\frac{\partial \delta\gamma}{\partial z} = \frac{\gamma_0 \rho_{\perp 0}^s R_B^{s/2}}{\rho_{z0}} \Re \left\{ F_{\perp ks} \exp(-is\phi_0) V_k \right\}, \quad (3.9c)$$

and

$$\frac{\partial \delta\phi}{\partial z} = \frac{\delta\gamma k_0}{s\rho_{z0}} - \frac{\delta\gamma - \rho_{\perp 0} R_B \delta\rho_{\perp}}{\rho_{z0}^3} \left( \frac{\gamma_0 k_0}{s} - \frac{\Omega_0}{c} \right) + \frac{\gamma_0 \rho_{\perp 0}^{s-2} R_B^{s/2-1}}{\rho_{z0}} \Im \left\{ F_{\perp ks} \exp(-is\phi_0) V_k \right\}, \quad (3.9d)$$

with the wave equation being given by

$$\left(-i\frac{1}{k_0}\frac{\partial^2}{\partial z^2}-\Gamma_k\right)V_k = -8\pi\frac{I}{I_A}F_{\perp ks}^*\frac{\rho_{\perp 0}^s R_B^{s/2}}{\rho_{z0}} \times \left\langle \exp(is\phi_0) \left( s\frac{\delta\rho_{\perp}}{\rho_{\perp 0}} - \frac{\delta\gamma - \rho_{\perp 0}R_B\delta\rho_{\perp}}{\rho_{z0}^2} + is\delta\phi \right) \right\rangle. \quad (3.9e)$$

On the right hand side of Eq. (3.9e), the average is still over the electron trajectories. In practice, this means average over different initial phases. By writing  $\phi_0 = \phi_{00} + \hat{\phi}_0$ , where  $0 \leq \phi_{00} < 2\pi$  is the value of  $\phi_0$  at the entrance of tunnel, we can take the average as over  $\phi_{00}$ . Then Eq. (3.9a) can be written as

$$\frac{d\hat{\phi}_0}{dz} = \frac{1}{\rho_{z0}} \left( \gamma_0 k_0 - \frac{\Omega_0}{c} \right) \quad (3.10)$$

with the initial condition  $\hat{\phi}_0(z_0) = 0$ . Further, each perturbed quantity in Eq. (3.9) is proportional to  $\exp(-i\phi_{00})$ . Thus, by defining  $(\delta\hat{\phi}, \delta\hat{\gamma}, \delta\hat{\rho}_{\perp}) = \langle (\delta\phi, \delta\gamma, \delta\rho_{\perp}) e^{i\phi_{00}} \rangle$ , we reduce Eq.(3.9a)-(3.9d) to a set of equations for variables that are independent of the initial phase  $\phi_{00}$  :

$$\hat{\phi}_0 = \int_0^z dz \frac{1}{\rho_{z0}} \left( \gamma_0 k_0 - \frac{\Omega_0(z)}{c} \right) \quad (3.11a)$$

$$\frac{\partial\delta\hat{\rho}_{\perp}}{\partial z} = \frac{\gamma_0}{2\sqrt{R_B}\rho_{z0}} \left( F_{\perp ks} \exp(-i\hat{\phi}_0) V_k \right) \quad (3.11b)$$

$$\frac{\partial\delta\hat{\gamma}}{\partial z} = \frac{\gamma_0\rho_{\perp 0}\sqrt{R_B}}{2\rho_{z0}} \left( F_{\perp ks} \exp(-i\hat{\phi}_0) V_k \right) \quad (3.11c)$$

$$\frac{\partial\delta\hat{\phi}}{\partial z} = \frac{\delta\hat{\gamma}k_0}{\rho_{z0}} - \frac{\delta\hat{\gamma} - \rho_{\perp 0}R_B\delta\hat{\rho}_{\perp}}{\rho_{z0}^3} \left( \gamma_0 k_0 - \frac{\Omega_0}{c} \right) + \frac{\gamma_0}{2i\rho_{\perp 0}\rho_{z0}\sqrt{R_B}} \left( F_{\perp ks} \exp(-i\hat{\phi}_0) V_k \right) \quad (3.11d)$$

Given that all perturbed quantities in Eqs. (3.9) are proportional to  $\exp(-is\phi_{00})$ , the average over values of  $\phi_{00}$  can be carried out. Basically, the result of the average is to remove the brackets from Eq. (3.9e),

$$\left(-i\frac{1}{k_0}\frac{\partial^2}{\partial z^2}-ik_0\left(1-\frac{\omega_{cut}^2}{\omega^2}\right)\right)V_k=-8\pi\frac{I}{I_A}\frac{\rho_{\perp 0}\sqrt{R_B}}{\rho_{z0}}F_{\perp ks}^*\exp(i\hat{\phi}_0)\times\left(\frac{\delta\hat{\rho}_{\perp}}{\rho_{\perp 0}}-\frac{\delta\hat{\gamma}-\rho_{\perp 0}R_B\delta\hat{\rho}_{\perp}}{\rho_{z0}^2}+i\delta\hat{\phi}\right)\quad (3.11e)$$

The initial conditions for this equation set at the entrance of the beam tunnel are:  $\delta\rho_{\perp}(z_{st})=0$ ,  $\delta\gamma(z_{st})=0$ ,  $\delta\phi(z_{st})=0$ , and  $V_k(z_{st})=1$ ,  $dV_k(z_{st})/dz=-ik_z(z_{st})V_k(z_{st})$ . Here we assume the initial wave amplitude of the excited wave to be 1, as this quantity is arbitrary in the small signal limit. Eqs.(3.11) form a set of self consistent equations for the interaction between electromagnetic field and electron beam, which we can solve. The growth rate is determined when boundary condition are applied at  $z=z_{st}$

### 3.2.2 Normalized equations far from cut-off frequency

When the operation is far from the cutoff, the interaction of the wave with the forward wave is smaller compared to interaction with the backward wave, so it can be neglected. This is demonstrated in the following for the normalized equation.

By assuming that the operation is not far away from the cutoff frequency so that  $\rho_z$  is approximately constant, and guiding magnetic field is constant ( $R_B=1$ ), we normalize Eqs. (3.8) in the way same as in Ref. 41. Substituting relation  $R_B\rho_{\perp 0}\delta\rho_{\perp}=\delta\gamma$ , which could be seen by combining Eq. (3.11b) and Eq. (3.11c), normalized electron rotational energy  $w=p_{\perp}^2/p_{\perp 0}^2=2(\gamma_0-\gamma)/\beta_{\perp 0}^2\gamma_0=-2\delta\gamma/\beta_{\perp 0}^2\gamma_0$ , normalized axial coordinate  $\varsigma=(\beta_{\perp 0}^2/2\beta_{z0})k_0z$  and normalized wave amplitude  $F=2\gamma_0^{s-1}\beta_{\perp 0}^{s-4}F_{\perp ks}V_k/k_0$  into Eqs. (3.9b) and (3.9d), the normalized equations could be written as

$$\frac{\partial w}{\partial \zeta} = -2\Re\{F e^{-is\phi_0}\}, \quad (3.12a)$$

$$\frac{\partial(s\delta\phi)}{\partial \zeta} = -w + s\Im\{F e^{-is\phi_0}\}. \quad (3.12b)$$

Also by substituting  $\bar{h} = 2\beta_{z0}k_z/\beta_{\perp 0}^2 k_0$ , and normalized injected current density  $\hat{I} = 64\pi I/I_A |F_{\perp ks}/k_0|^2 \beta_{\perp 0}^{2(s-4)} \beta_{z0}$  into Eq.(3.9e), the normalized beam-wave interaction equation will have the following form,

$$\frac{d^2 F}{d\zeta^2} + \bar{h}^2 F = -i\hat{I} \left\langle e^{is(\phi_0 + \delta\phi)} \left(1 - \frac{s\omega}{2}\right) \right\rangle. \quad (3.12c)$$

We define a new phase variable  $\theta$ , which relates with  $\phi$  in Eq. (3.6b) by  $\theta = \theta_0 + \delta\theta = s\phi = s(\phi_0 + \delta\phi)$ , also from Eq. (3.8a) we could have that  $s\phi_0 = s\phi_{00} + \Delta\zeta$  and  $\theta_0 = s\phi_{00}$ , so  $\delta\theta = s\delta\phi + \Delta\zeta$ , where

$$\Delta = \frac{2}{\beta_{\perp 0}^2} \left(1 - \frac{s\Omega_0}{\gamma_0 \omega}\right). \quad (3.12)$$

We could get the set of normalized equations as following,

$$\frac{\partial w}{\partial \zeta} = -2\Re\{F e^{-i(\theta_0 + \Delta\zeta)}\} \quad (3.13a)$$

$$\frac{\partial \delta\theta}{\partial \zeta} = -w + \Delta + s\Im\{F e^{-i(\theta_0 + \Delta\zeta)}\} \quad (3.13b)$$

$$\frac{d^2 F}{d\zeta^2} + \bar{h}^2 F = -i\hat{I} \left\langle e^{i(\theta_0 + \delta\theta)} \left(1 - \frac{s\omega}{2}\right) \right\rangle \quad (3.13c)$$

This set of equations is consistent with the second order equations in Ref. 12 for the case when the operating is close to the cutoff.

For the situation that the radius of the tunnel is constant and the external magnetic field is fixed, let  $F = f e^{i\Delta\zeta}$  in Eqs. (3.13), then

$$\frac{d^2 F}{d\zeta^2} = e^{i\Delta\zeta} \left( \frac{d^2 f}{d\zeta^2} + 2i\Delta \frac{df}{d\zeta} - \Delta^2 f \right) \quad (3.14)$$

Substituting this into Eq. (3.13c), we get

$$\frac{d^2 f}{d\zeta^2} + 2i\Delta \frac{df}{d\zeta} + (\bar{h}^2 - \Delta^2) f = -i\hat{I} \left\langle e^{i\theta_0} \left( i\delta\theta - \frac{sw}{2} \right) \right\rangle. \quad (3.15)$$

In the left hand side of Eq. (3.15)

$$\bar{h}^2 - \Delta^2 = - \left( \frac{2}{\beta_{\perp 0}} \right)^2 \frac{(\omega - k_z v_{z0} - s\Omega_0/\gamma_0)(\omega + k_z v_{z0} - s\Omega_0/\gamma_0)}{\omega^2} \quad (3.16)$$

When the backward wave excitation condition is satisfied, i.e.  $|\omega + k_z v_{z0} - s\Omega_0/\gamma_0|/\omega$  is small, then  $(\omega - k_z v_{z0} - s\Omega_0/\gamma_0)/\omega = -2k_z v_{z0}/\omega$ . So we have

$$\bar{h}^2 - \Delta^2 = - \left( \frac{2}{\beta_{\perp 0}} \right) \frac{(\omega + k_z v_{z0} - s\Omega_0/\gamma_0)}{\omega} \cdot 4 \frac{\beta_{z0}}{\beta_{\perp 0}^2} \frac{k_z}{k_0} \quad (3.17)$$

If the operation is far from the cutoff, i.e.  $|\omega - s\Omega_0/\gamma_0| \cdot L/v_{z0} \gg \pi$ , so  $|\Delta| \gg |df/d\zeta|/f$ , we could omit the second order derivative in Eq.(3.15). So the Eq. (3.15) could be rewritten as

$$\frac{df}{d\zeta} - i\tilde{\Delta} f = \tilde{I} \left\langle e^{i\theta_0} \left( i\delta\theta - \frac{sw}{2} \right) \right\rangle, \quad (3.18a)$$

where  $\tilde{\Delta} = 2(-\omega - k_z v_{z0} + s\Omega_0/\gamma_0)/\beta_{\perp 0}^2 \omega$  and  $\tilde{I} = \beta_{\perp 0}^2 / 4\beta_{z0} \cdot k_0/k_z \hat{I}$ .

Also by substituting  $f = Fe^{-i\Delta\zeta}$  into Eqs.(3.13a) and (3.13b), we could get

$$\frac{dw}{d\zeta} = -2\Re\{Fe^{-i\theta_0}\}, \quad (3.18b)$$

$$\frac{d\delta\theta}{d\zeta} = -w + s\Im\{Fe^{-i\theta_0}\}. \quad (3.18c)$$

Eqs.(3.18) form a set of first order normalized equations for the backward wave excitation in the beam tunnel of gyrotron, which are also consistent with the equations in Ref. 41.

For a more general gyro-BWO for the situation that the operation is far from cutoff with slightly tapered parameters the set of three first-order ordinary differential equations forms a self-consistent set of equations containing a small number of parameters [35] (let  $s = 1$ ):

$$\frac{dw}{d\zeta} = -2(1-w)^{1/2} \operatorname{Re}(F e^{-i\vartheta}), \quad (3.19a)$$

$$\frac{d\vartheta}{d\zeta} = w + (1-w)^{-1/2} \operatorname{Im}(F e^{-i\vartheta}), \quad (3.19b)$$

$$\frac{dF}{d\zeta} - i\Delta F = I_0 \langle (1-w)^{1/2} e^{i\vartheta} \rangle. \quad (3.19c)$$

Here Eqs. (3.19a) and (3.19b) represent equations for electron rotational energy  $w = p_{\perp}^2 / p_{\perp 0}^2$  and gyrophase with respect to the wave phase  $\vartheta = \theta - (\omega t - k_z z)$  (these equations are averaged over fast electron gyrations),  $\zeta = (\beta_{\perp 0}^2 / 2\beta_{z0}) (\omega z / c)$  is the normalized axial coordinate (here  $\beta_{\perp 0}$  and  $\beta_{z0}$  are initial orbital and axial velocities of electrons normalized to the speed of light). Eq. (3.19c) is equation describing the wave excitation in the case of operation far from cutoff when the second-order wave equation can be reduced to the first-order one (as explained in Introduction). This equation is written for the dimensionless wave amplitude  $F$ . The parameter  $\Delta$  in its right-hand side is the normalized cyclotron resonance detuning

$$\Delta = \frac{2}{\beta_{\perp 0}^2} \frac{\omega - k_z v_{z0} - \Omega_0}{\omega}. \quad (3.20)$$

In the right-hand side of Eq. (3.19c)  $I_0$  is the normalized beam current, which will be specified below and angular brackets denote averaging over initial gyrophases of electrons at the entrance  $\vartheta_0$ . The boundary conditions to Eq. (3.19a)-(3.19c) describe the absence of electron modulation in energies and phases at the entrance [  $w(0)=1$ ,  $\vartheta(0)=\vartheta_0$  uniformly distributed between 0 and  $2\pi$  ] and zero amplitude of a backward wave at the right end of the interaction region  $F(\zeta_{end})=0$ . As follows from the consideration of the beam tunnel, the cyclotron resonance detuning Eq. (3.20) depends on the axial coordinate because  $k_z$  and  $\Omega_0$  are axially dependent (in Eq. (3.20)  $\Omega_0$  and  $v_{z0}$  are determined for an electron beam with velocities and energies non-perturbed by electromagnetic waves). When a lossy material is put on the wall of a beam tunnel, the axial wave number in Eq. (3.20) is a complex value and both, the real and imaginary parts of it can be functions of the axial coordinate.

Equations Eqs. (3.19a)-(3.19c) are given for the case when the axial wavenumber is not too small and not too large. The meaning of this statement is the following: as was just mentioned, the axial wavenumber should be not too small in order for interaction with the forward wave to be non-resonant and, hence, neglect it. At the same time, this axial wavenumber should not be too large that allows one to neglect a so-called recoil effect, i.e. changes in the electron axial velocity in the process of radiating electromagnetic waves [30-31,12]. Introducing  $n = k_z / (\omega / c)$ , i.e. the axial wavenumber normalized to  $\omega / c$ , one can present the corresponding conditions as  $2n(\omega L / c) \gg 1$  (for neglecting the forward wave interaction) and  $n(\beta_{\perp 0}^2 / 2\beta_{z0}) \ll 1$

(for neglecting recoil effect). As one can see, when the interaction length is long enough, both conditions can be easily satisfied.

To determine the self-excitation conditions for backward wave excitation it is necessary to solve linear Eqs. (3.19a-3.19c) together with corresponding boundary conditions. The linearization implies small perturbations in the electron energy and phase caused by the wave:  $w = 1 + \tilde{w}$ ,  $\vartheta = \vartheta_0 + \tilde{\vartheta}$ . Then, linear equations for  $\bar{w} = \langle \tilde{w} e^{i\vartheta_0} \rangle$ ,  $\bar{\vartheta} = \langle \tilde{\vartheta} e^{i\vartheta_0} \rangle$  and  $F$  follow from Eqs. (3.19a- 3.19c):

$$\frac{d\bar{w}}{d\zeta} = F, \quad (3.21a)$$

$$\frac{d\bar{\vartheta}}{d\zeta} = -\bar{w} - \frac{i}{2} F, \quad (3.21b)$$

$$\frac{dF}{d\zeta} - i\Delta(\zeta)F = I_0(\zeta) \left( \frac{\bar{w}}{2} + i\bar{\vartheta} \right). \quad (3.21c)$$

These three first-order differential equations can be directly solved with the boundary conditions  $\bar{w}(\zeta_{st}) = \bar{\vartheta}(\zeta_{st}) = 0$  and  $F(\zeta_{st}) = 1$ . (The absolute value of the wave amplitude at the entrance does not matter in the framework of the small-signal theory.) These equations should be solved for various values of the detuning  $\Delta$  and beam current parameter  $I_0$  and just those values of these parameters which yield zero amplitude of a wave in a certain cross-section determine solution of the problem. In the case of constant detuning and beam parameter, Eqs. (3.21) can be reduced to the dispersion equation of the gyro-BWO which, in turn, at small values of the beam current parameter can be reduced [12] to the dispersion equation of the linear-beam backward-wave oscillator [28]. As known [28], the variables in this case can be

normalized to the Pierce gain parameter whose role in our notations is played by the normalized beam current parameter. Then, the starting value of the normalized length  $l_{st} = I_0^{1/3} \zeta_{end,st}$  can be determined as the function of the attenuation parameter and other parameters of the system.

### **3.3 Results and Analysis**

#### **3.3.1 Results by solving the normalized first order equations**

By using the first order differential equations (3.21), we assume the oscillation is far from the cut off frequency along the whole axis. While, at part of the beam tunnel the oscillation is close to the cut off, which we will take into consideration later in the next section

Intuitively, the amplitude of the excited wave grows from zero in both negative and positive z directions. So we assume the boundary condition for excited wave as

$$V_k(z_{ex}) = 0. \quad (3.22)$$

For a fixed value of surface impedance, we search for the solution to Eqs.(3.21) satisfying Eq. (3.22) by varying the frequency,  $z_{ex}$  is the axial position where the excitation happens.

Let us start presentation of our results from considering a simple case of a gyro-BWO with constant parameters operating far from cutoff. In this case, solution of Eqs.(3.21) yields the following dependence of the starting length of the beam current.

Fig. 3.3 gives the normalized start length  $\zeta_{st} = (\beta_{\perp 0} / 2\beta_{z0})(\omega/c)z_{ex}$  as function of normalized beam current density

$$I_0 = 4 \frac{eI_b}{mc^3} \frac{J_{m\pm 1}^2(j'_{m,p} R_b/R)}{(j'_{m,p} - m^2)J_m^2(j'_{m,p})} \frac{\kappa^{-2} (1 - n\beta_{z0})^3}{n \gamma_0 \beta_{\perp 0}^4} \quad (3.23)$$

for different  $\Delta_i = 2k_{z_i}v_{z0}/(\omega\beta_{\perp 0}^2)$ , which is the imaginary part of  $\Delta$  (defined in Eq. (3.12)) caused by putting materials with different  $k_{z_i}$  on the inner surface of tunnel. Here  $R_b$  is the radius of the electron guiding center. We can see from Fig. 3.3 that the normalized starting length is inversely proportional to the normalized beam current, which is caused by the fact that for higher beam current the excitation is easier. Also starting length for higher  $\Delta_i$  is longer, which indicates that for higher surface impedance the excitation is harder. So our assumption that the backward wave excitation can be suppressed by applying high enough surface impedance on the inner surface of the beam tunnel, is right.

For the specific 170GHz gyrotron in Ref. 25, whose parameters are  $B=6.6\text{T}$ ,  $R = 14.25\text{mm}$ , beam radius  $r_b = 9\text{mm}$  beam energy  $V_{beam} = 80\text{kV}$ , and pitch factor  $\alpha = v_{\perp}/v_z = 1.3$ . For the TE 24, 6 mode we can show the dimensional minimum interaction length needed for the excitation is plotted as a function of the current density of the injected electron beam for different surface impedances are plotted in figure 3.4.

The different curves correspond to different values of surface impedance on the waveguide wall. Here  $Z_s/Z_0$  is the ratio of the surface impedance of the wall to the impedance of free space. Non-zero impedance corresponds to the presence of lossy materials in the wall. The solid curve shows the expected scaling of start length with beam current  $L_{st} : I^{-1/3}$  [30].

Figure 3.1 shows the typical structure of the beam tunnel in a gyrotron. The radius

of the wall is tapered and the strength of the external guiding magnetic field varies. This effect is taken into our consideration. Here we still use the parameters from Ref. [25], beam radius  $R[mm] = 14.25 - 0.06 \times z$ ,  $z$  [mm] is 0 at the end of the beam tunnel, and the distribution of magnetic field is  $B[T] = 6.64 \left( 1.0 - 0.9e^{-6(\omega/c \cdot z)^2} \right)$

We see from Fig. 3.2 that because the tapering of the wall radius and variation of the guiding magnetic field, the approximate excitation condition  $\Omega > \omega_c(z)$  depends on axial position. We plot  $(\Omega - \omega_c)/c$  versus  $z$  for several TE modes in Fig. 3.5. We see that the TE 24, 6 mode has a relatively large interaction length, and is more likely to be unstable. Fig. 3.6 is the starting length as function of injected beam current for the gyrotron [25] with profiles of magnetic field and tapering of wall radius.

From Fig. 3.4 and 3.6, we see that the larger the injected current density, the more likely the backward wave will be excited. But this excitation can be suppressed by including a lossy material on the wall of the beam tunnel. Our analysis shows how much surface impedance we need to put on the wall to suppress the excitation. For the case in Ref. 25  $I_b=40A$ , we see that  $Z_s/Z_0=0.085$  or lower surface impedance is enough.

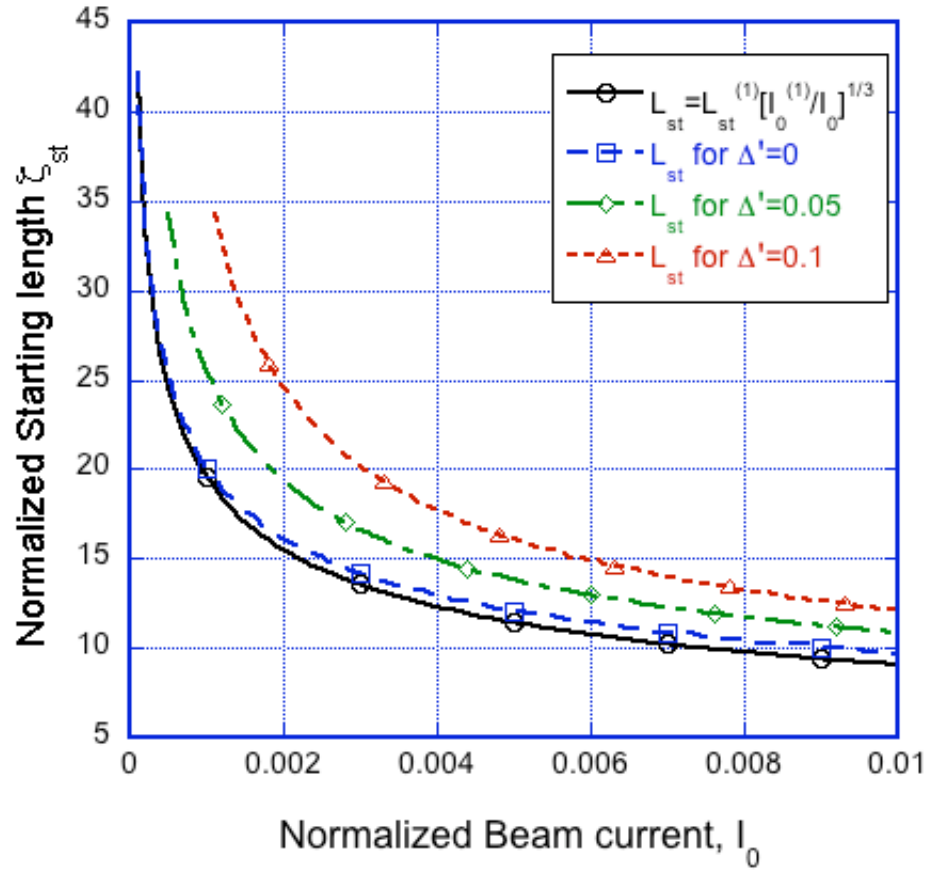
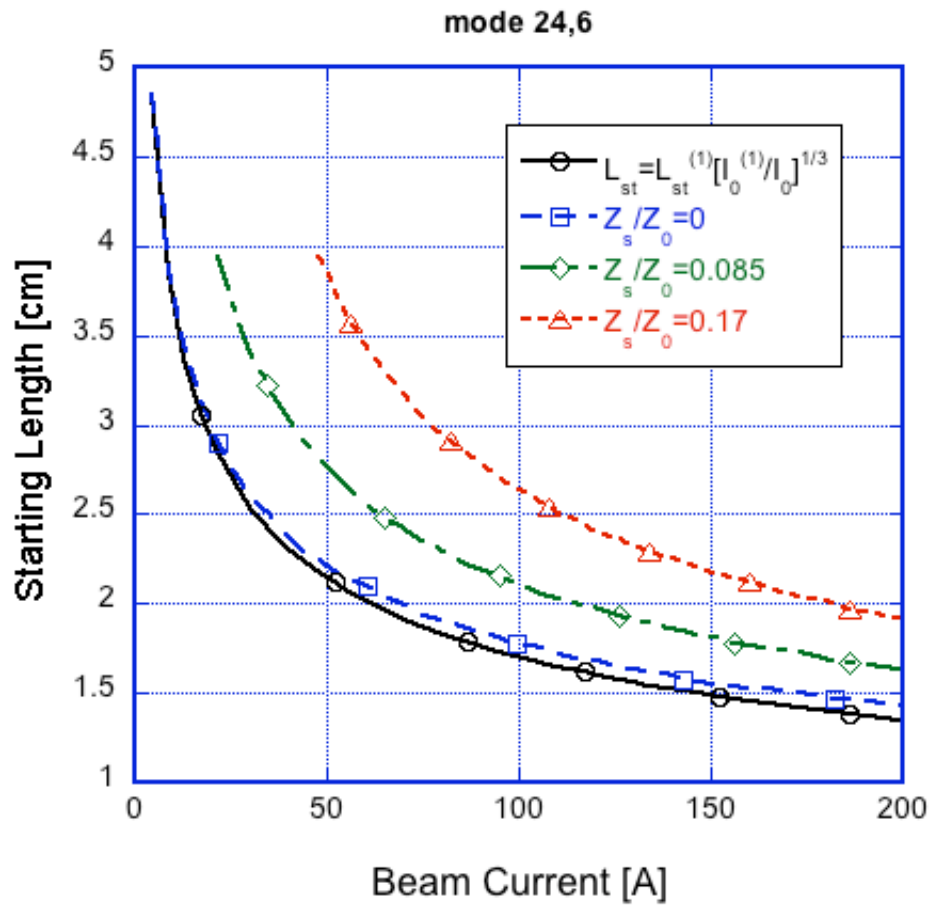


Fig. 3.3 normalized starting interaction length as function of normalized beam current of different  $\Delta_i$



**Fig. 3.4.** Start interaction length is plotted as function of beam current assuming that there is no tapering of the wall and constant magnetic.

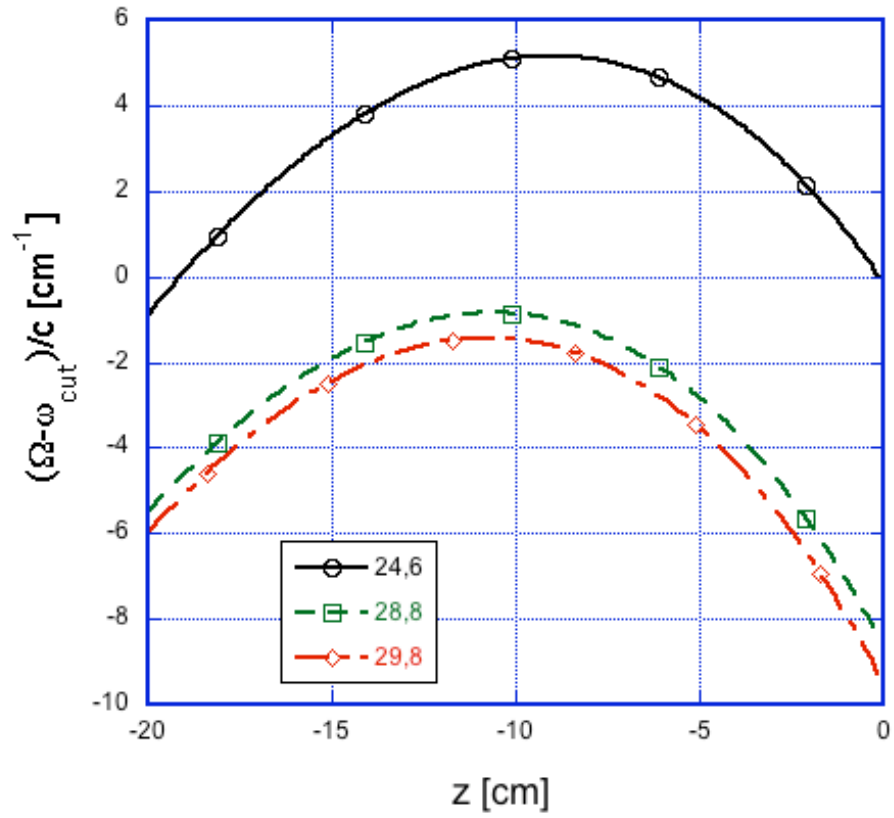


Fig. 3.5.  $(\Omega - \omega_{cut})/c$  is plotted versus  $z$  for different modes. Only when it is positive, can wave excitation happen.

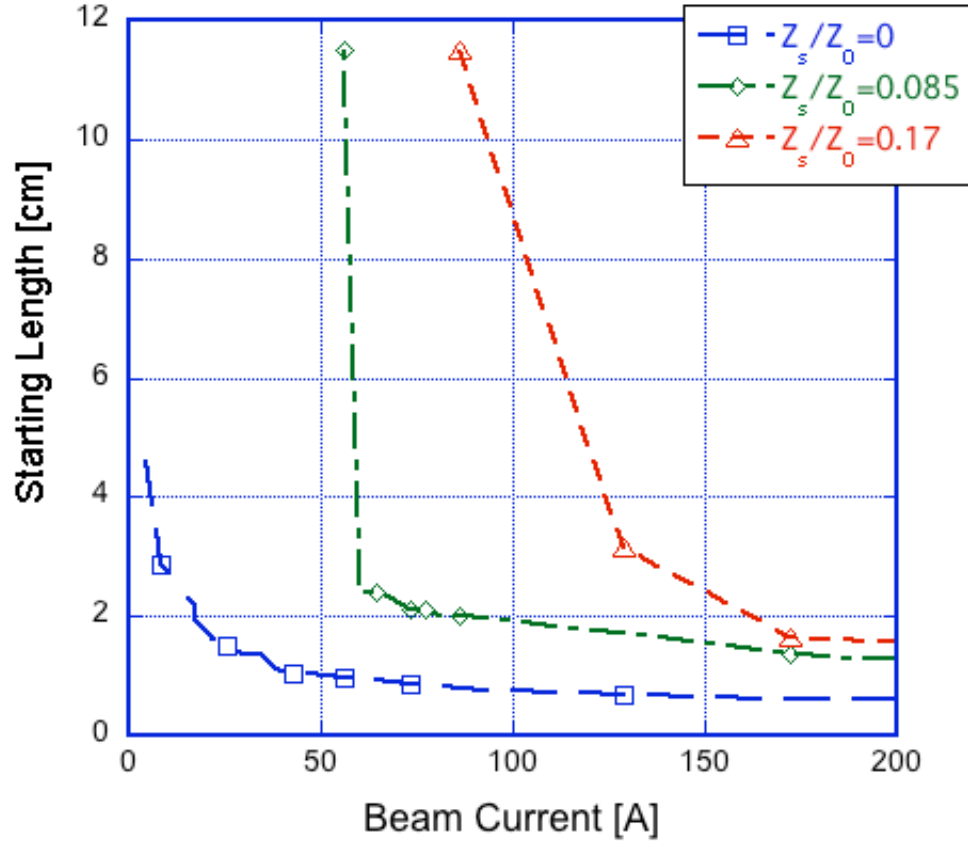
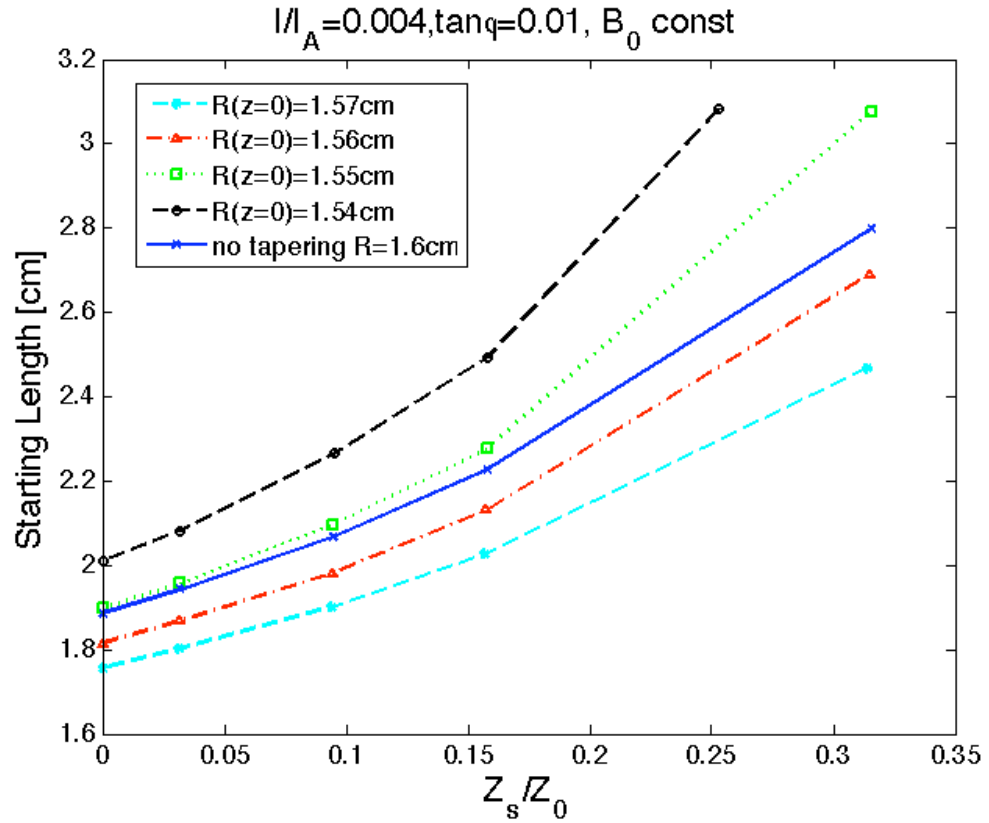


Fig. 3.6. Start interaction length as function of beam current includes the effect of the wall tapering and varying of magnetic field

### 3.3.2 Results by solving the second order equations

When the operation is close to the cut-off frequency, the forward wave will be excited together with the backward wave. Here we assume that the injected beam current is  $I = 68A$ , external magnetic field is constant with  $B_0 = 6.65T$  and tapering angle of the tunnel radius is  $\tan\phi = 0.01$ . Eq. (3.11) is solved for different values of cavity radius by applying Eq. (3.22) as the boundary condition.



**Fig. 3.7.** Starting length as function of surface impedance for different tapering, with fixed magnetic field ( $B_0 = 6.65T$ ).

Starting length as function of surface impedance is plotted in Fig. 3.7. The blue line is for constant tunnel radius as  $R_w = 1.6\text{cm}$ . From Fig. 3.7, we know that by increasing the surface impedance of the surface, the starting length is longer, i.e. the unstable excitation is easier to be suppressed. The excited wave is possibly backward wave, forward wave excitation, or both. We can also see for larger tunnel radius, the starting length is shorter, so excitation is more likely happen.

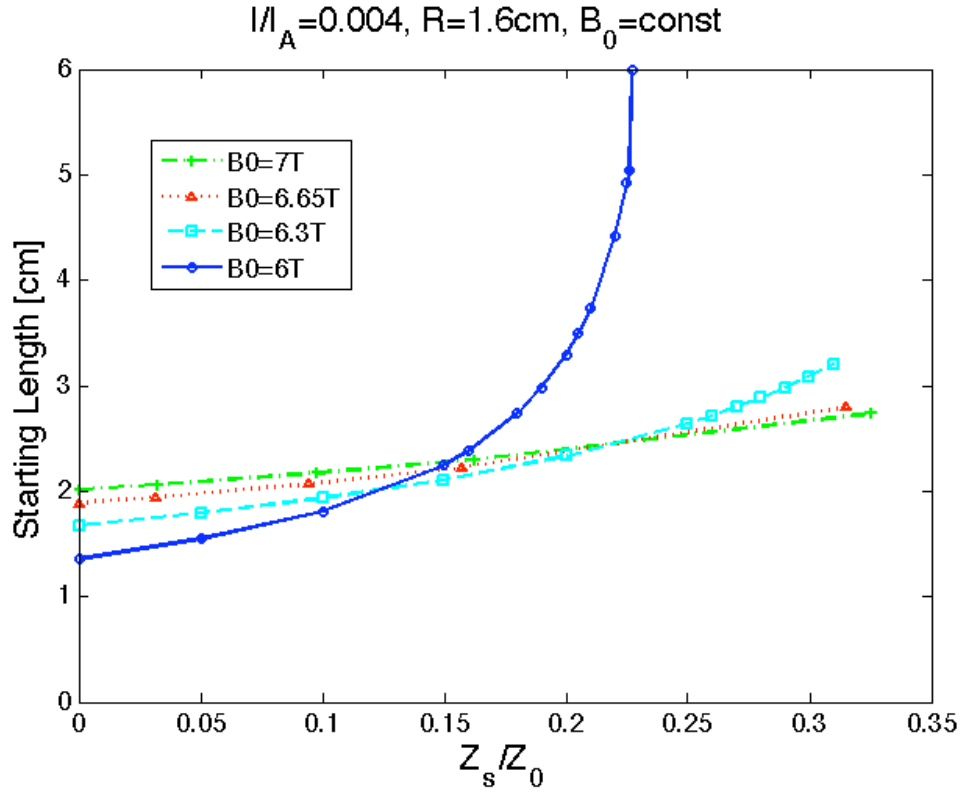


**Fig. 3.8**, Starting length as function of surface impedance for different magnetic fields, with fixed tunnel radius ( $R_w = 1.6\text{cm}$ ).

Assuming that the tunnel radius is constant ( $R_w = 1.6\text{cm}$ ), the starting length is plotted as function of surface impedance for several fixed magnetic field values in Fig. 3.8. We can see that for a fixed magnetic field ( $B_0 = 6\text{T}$ ) there exists a certain surface impedance value where the excitation can be suppressed. The surface impedance needed to suppress the excitation is proportional to the external magnetic field. This is not consistent with our expectations for backward wave excitation. For backward wave, the cyclotron resonant frequency is closer to the cutoff frequency

(Fig. 3.2) for smaller magnetic field. Thus, higher surface impedance is needed to suppress the excitation. But lower surface impedance is needed for forward wave. To see the transition from backward wave excitation to forward wave excitation clearly, we plot the starting length as function of the magnetic field for fixed surface impedance in Fig. 3.9.

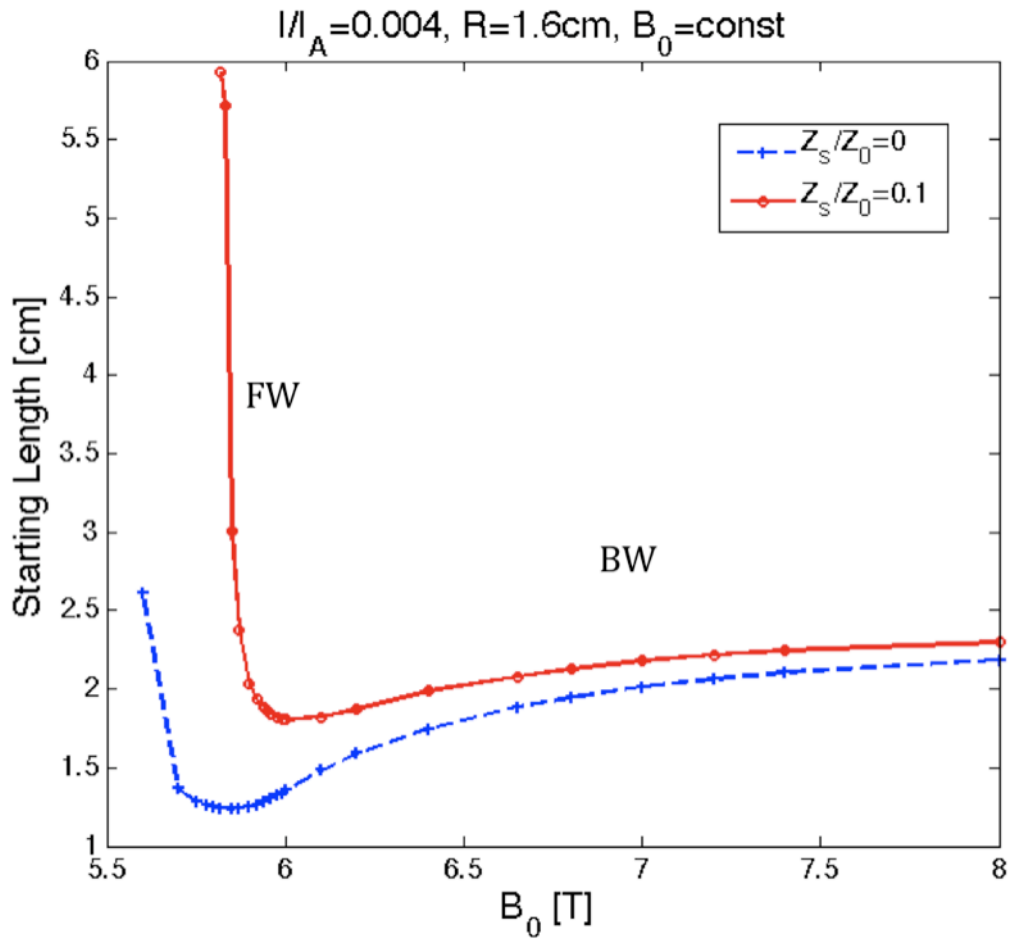


**Fig. 3.9.** Starting length as function of external magnetic field for different surface impedance when the tunnel radius is fixed ( $R_w = 1.6\text{cm}$ ).

### 3.3.3 Boundary condition modifications to the model

Eq. (3.22) is an approximation to the real boundary condition. It doesn't really satisfy the boundary condition of the wave in the beam tunnel or cavity. So instead, we can solve the problem by applying the following boundary condition. At the entrance of the tunnel ( $z_i$ ) the excited wave is propagating in backward direction, so it satisfies the  $\left(\frac{dV_k}{dz} + i|k_z|V_k\right)\Big|_{z=z_i} = 0$ . The remaining boundary condition that must be satisfied is the condition that the mode is outgoing or evanescent at  $z = z_s$ ,

$$C(\omega, Z_s) = \left(\frac{dV_k}{dz} / V_k\right)\Big|_{z=z_s} - ik_z(z_s) = 0. \quad (3.24)$$

Here we have indicated that the quantity  $C$  depends implicitly on the frequency ( $\omega$ ) and surface impedance ( $Z_s$ ). The surface impedance determines  $k_i$  which is the imaginary part of  $k_k$  in Eq. (3.4a) in the following way [42]:

$$k_i = \frac{Z_s}{Z_0 R(z) \sqrt{1 - \omega_c^2 / \omega^2}} \left( \frac{\omega_c^2}{\omega^2} + \frac{m^2}{j_{m,p}^2 - m^2} \right) \quad (3.25)$$

for the mode  $TE_{m,p}$ , where  $Z_0 = 376.7\Omega$  is the impedance of free space.

Equations (3.11a)-(3.11e) form a set of self-consistent equations for the interaction between the electromagnetic field and the electron beam, which we solve. We initialize the perturbed variables according to Eqs. (3.12), and integrate Eqs. (3.11a)-(3.11e) forward in  $z$  from  $z = z_0$  to the point  $z_s$ , where we evaluate the complex quantity  $C(\omega, Z_s)$ . Finding a solution then becomes a two dimensional search for parameter values that give  $C(\omega, Z_s) = 0$ . Our procedure for doing this is described in the next section.

First we compare our calculation with previous work such as the Gyro-BWO in Ref. 43 shown in the Fig. 3.10 with magnetic field  $B_0 = 14.52kG$ , beam voltage  $V_b = 100kV$ , pitch factor  $\alpha = 1.0$  and guiding center at  $r_c = 0.09cm$ . The excited field profile from our simulation is shown in Fig. 3.11 (a) comparing with the profile in Ref. 43 in Fig. 3.11 (b). The start current from our calculation is  $I_{st} = 0.0226A$  with unstable mode frequency at  $f = 33.25GHz$ , which is very close to the current  $I_{st} = 0.03A$  with  $f = 33.30GHz$  from Ref. 43.

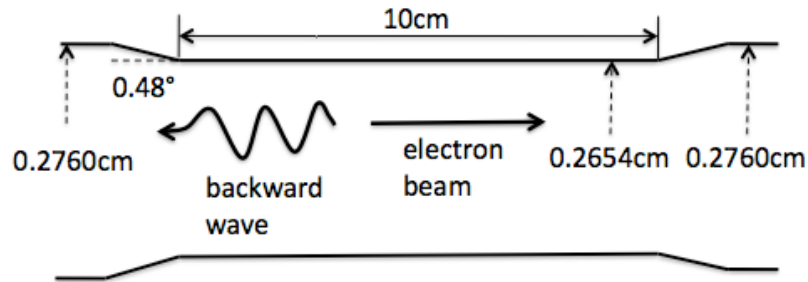
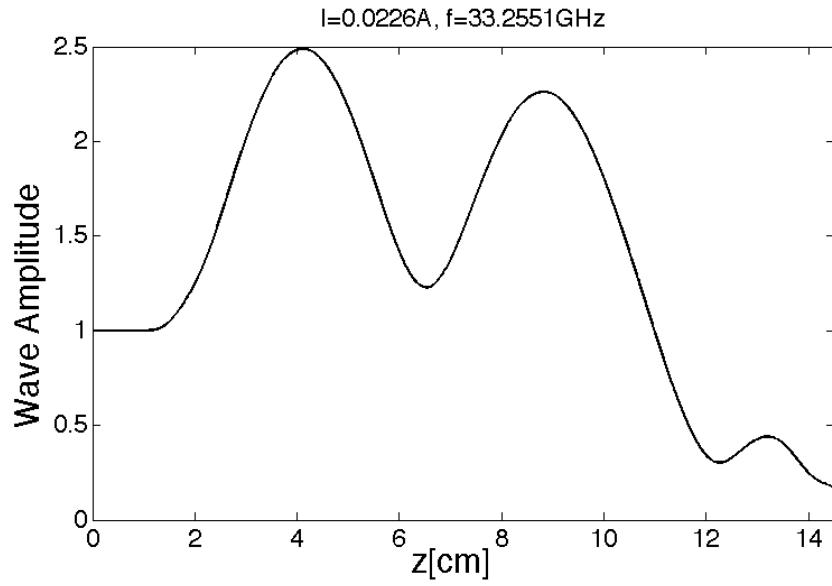
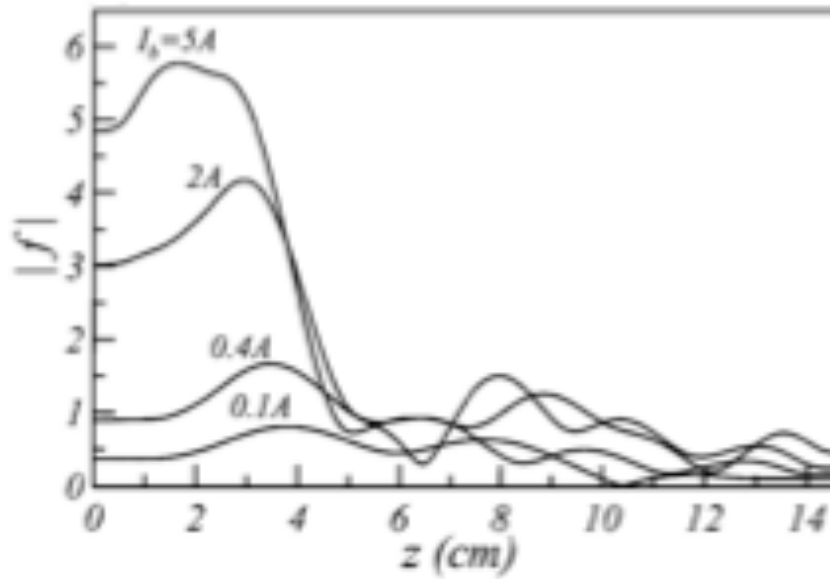


**Fig. 3.10.** Structure of Gyro-BWO in Ref. 43



(a) Field profile from our simulation



(b) Field profile from Ref. 43

**Fig. 3.11.** Stimulated backward wave profile in Gyro-BWO

In the following, we report numerical solutions of the system in MKSA units, Eqs. (3.11) and describe the method by which we impose the boundary condition, Eq. (3.24). Equation (3.24) is a complex transcendental equation for the unknown oscillation frequency  $\omega$ . For a given set of physical parameters there may or may not be solutions of Eq. (3.24) that correspond to instability  $\text{Im}(\omega) > 0$ . To determine if such solutions are present we use the Nyquist analysis [44]. That is we numerically evaluate  $C(\omega, Z_s)$  for a set of  $\omega$  values, that encircle the upper half  $\omega$ -plane. In practice this reduces to evaluating  $C(\omega, Z_s)$  for values of  $\omega$  along the real  $-\omega$  axis. We then plot the corresponding values of  $C$  in the complex plane and determine the net encirclement of the origin  $C = 0$ . This indicates the number of solutions of  $C = 0$  with  $\text{Im}(\omega) > 0$ .

As an example we consider the beam tunnel of a gyrotron operating at 170GHz. The beam voltage and current are 80KV and 50A, the pitch factor is 1.3, the beam radius is 9mm, and the length of the beam tunnel is 18cm. For this gyrotron we model the profile of the magnetic field to be  $B(z) = B_0 \left(1 - 0.5(z/L_B)^2\right)$ , where  $z = 0$  corresponds to the center of the cavity where  $B_0 = 6.64\text{T}$  and  $L_B = 22.36\text{cm}$ . The wall radius in the beam tunnel is given by  $R = R_0 - t_w(z - z_s)$ , where  $R_0 = 1.425\text{cm}$  and  $t_w = 0.06$ . Here  $z_s$  is the point where the wall radius equals  $R_0$ . These parameters correspond roughly to those of Ref. 25. Figs. (3.12a) (3.12b) and (3.12c) show the locus of  $C(\omega, Z_s)$  values computed for the  $\text{TE}_{24,6}$  mode for three increasing values of surface impedance:  $Z_s = 10.40\Omega$ ,  $10.59\Omega$  and  $12.92\Omega$  respectively. In Fig. (3.12a), with the lowest surface impedance the  $C(\omega, Z_s)$  curve encircles the origin twice

indicating the presence of two unstable modes. In Fig. (3.12b), the curve passes through the origin indicating the presence of a marginally stable mode, while in Fig. (3.12c) there is no encirclement of the origin indicating the beam tunnel is stable for this mode. Thus, use of the Nyquist analysis enables us to find the critical values of surface impedance needed to stabilize a particular mode, in this case,  $Z_s = 10.59\Omega$ . Further, by noting the frequency at which  $C(\omega, Z_s)$  passes through the origin, as in Fig. (3.12b), we can determine the frequency of the excited mode at marginal stability.

The presence of the multiple loops in the  $\rho(\omega, Z_s)$  curve indicates the presence of multiple axial modes in our system of equations. These multiple modes stem from the fact that the beam tunnel is long when measured in the gyration length  $L_\Omega = v_z / \Omega_0$ . For the gyrotron we considered here,  $L_\Omega \cong 0.08\text{cm}$ . So the number of electron orbits  $N = \Omega_0 T = \Omega_0 z_D / v_z \cong 225$ , where  $T$  is the travel time of the electron in the beam tunnel. The sensitivity of the frequency and the critical surface impedance to the point at which we apply the boundary conditions is illustrated in Fig. 3.13. Here we have plotted in Fig. (3.13a) the critical surface impedance and in Fig. (3.13b) the mode frequency as a function of the length of our simulation domain,  $z_D = z_s - z_o$ . As can be seen in the regions  $8 < z_D < 9.5\text{ cm}$ , the curves are not smooth due to mode hopping. This is made more clear in the inset of Fig. (3.13a), where the detailed structure of curves is resolved. Similar structure occurs for all values of  $z_D$ , but is not plotted. However, in spite of the small oscillations, the marginally stable solution generally falls in a narrow range of frequencies,  $159 < f < 160.5\text{GHz}$  with a critical surface impedance  $Z_s \approx 30\Omega$ . Thus, we can consider the results for specific parameters, in

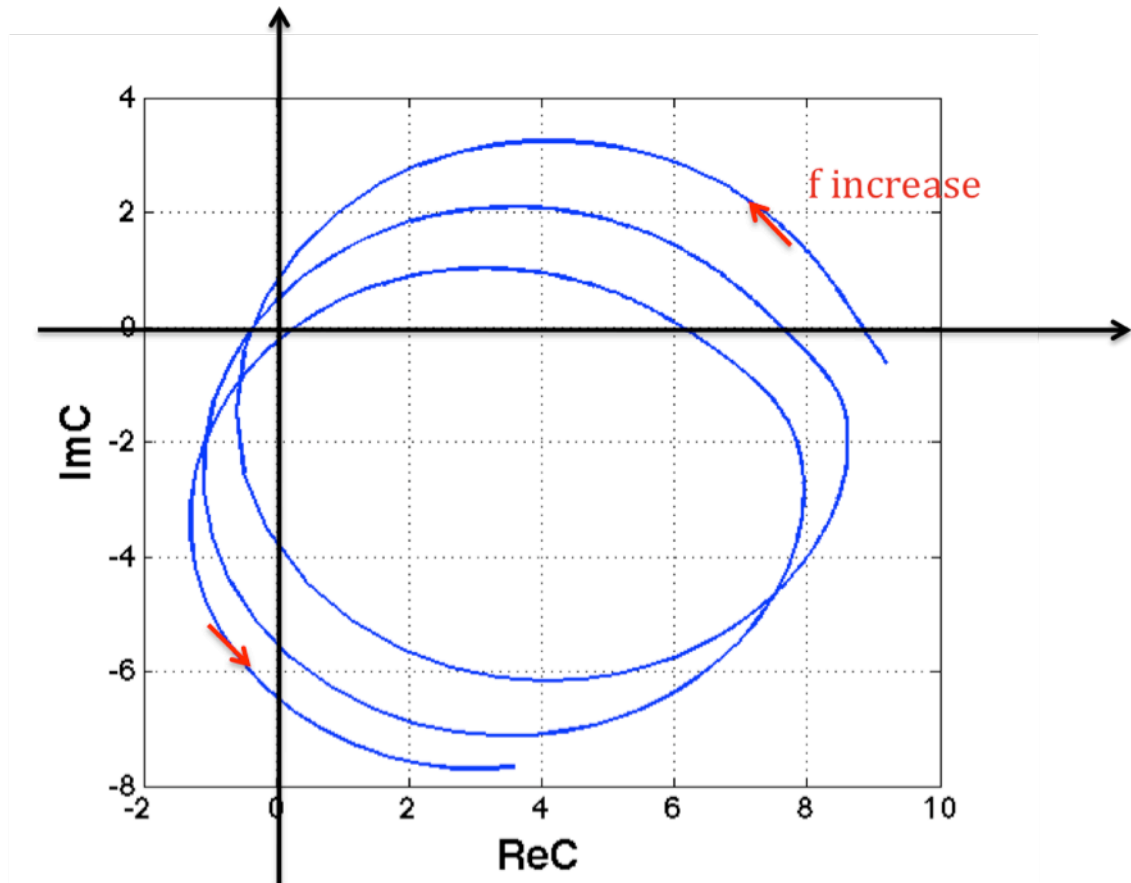
particular the beam tunnel length, to apply in practice. Further, it is likely that the small oscillations would disappear if the beam were given a spread in velocities.

In Fig. 3.14, we plot the critical surface impedance as function of external magnetic field ( $B_0$ ) for different values of injected beam current ( $I_{beam}$ ) and pitch factor ( $\alpha$ ) for the gyrotron structure in Ref. 25. Here we have taken  $z_D = 18\text{cm}$ , which corresponds to essentially the entire beam tunnel length. In Ref. 25 the beam current used was 50A and  $\alpha = 1.3$ . For these beam current and  $\alpha$  we found that the tunnel was stable with zero surface impedance. To find instability we increased the beam current and  $\alpha$  values, in excess of those used in the experiment. Specifically, we consider values of current  $I_{beam} = 51, 68, 102\text{A}$ , and values of pitch factor  $\alpha = v_{\perp}/v_z = 1.3$  and 1.5. We see that for the  $\text{TE}_{24,6}$  mode the hardest to stabilize oscillations occur for  $B_0 \sim 6.3\text{T}$ . The optimal  $B_0$  value for the gyrotron in Ref. 25 is  $B_0 = 6.64\text{T}$ , which is not the most unstable value according to our calculations.

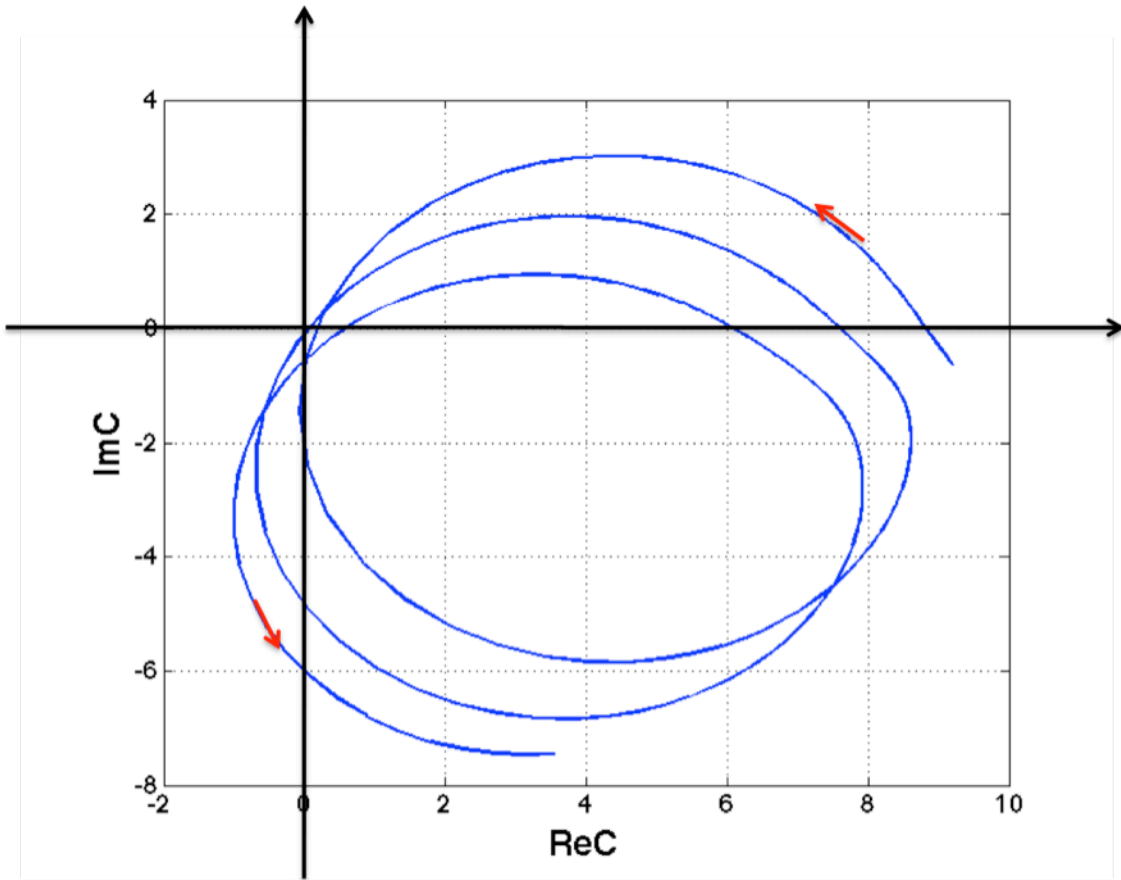
For the case of the highest current  $I_{beam} = 102\text{A}$ , which is much higher than the current value  $I_{beam} = 50\text{A}$  in Ref. 25, an isolated region of stability appears around  $B_0 = 6.0\text{T}$ . To investigate this we show in Fig. 3.15, the mode frequency at marginal stability vs magnetic field strength. We note that there is a mode transition around  $B_0 = 6.06\text{T}$ . The frequency jumps by about 1.5GHz. Note, this jump is much larger than the small jumps depicted in Fig.3.13. This changing of modes is responsible for the isolated region of stability.

Figures 3.13, 3.14 and 3.15 apply to the  $\text{TE}_{24,6}$  mode. Other modes have similar cutoff frequencies and may be excited. In Fig. 3.16 we plot the critical surface impedance for three representative modes. We see that the critical surface impedance

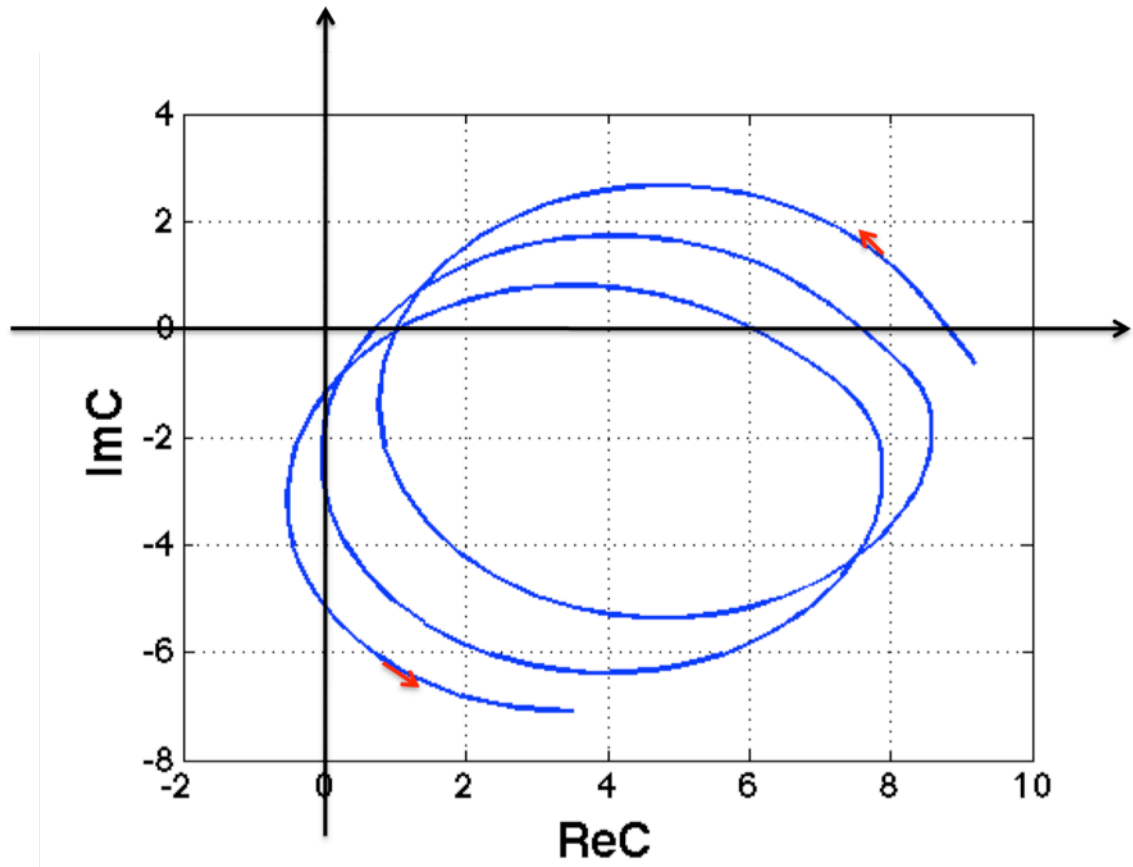
for these modes is in the same range as that of the  $TE_{24,6}$ . At  $B_0 = 6.25T$  the mode frequencies at the marginally stable modes are as follows: 160.852GHz ( $TE_{24,6}$ ), 160.865GHz ( $TE_{22,7}$ ) and 160.855GHz ( $TE_{20,7}$ ). We have similarly studied the  $TE_{20,8}$ ,  $TE_{16,7}$ ,  $TE_{12,10}$  and  $TE_{8,12}$  modes and found the ones shown in Fig. 3.16 to be most unstable.



(a) for  $Z_s = 10.40\Omega$

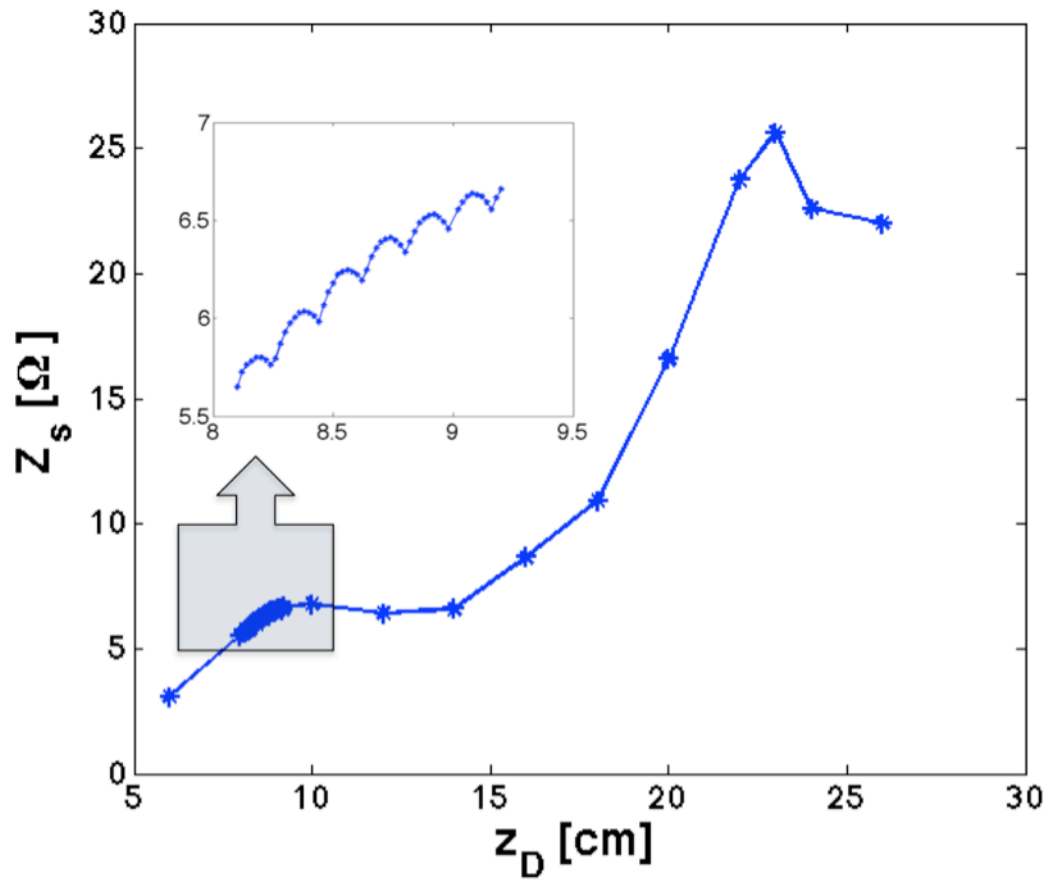


(b) for  $Z_s = 10.59\Omega$

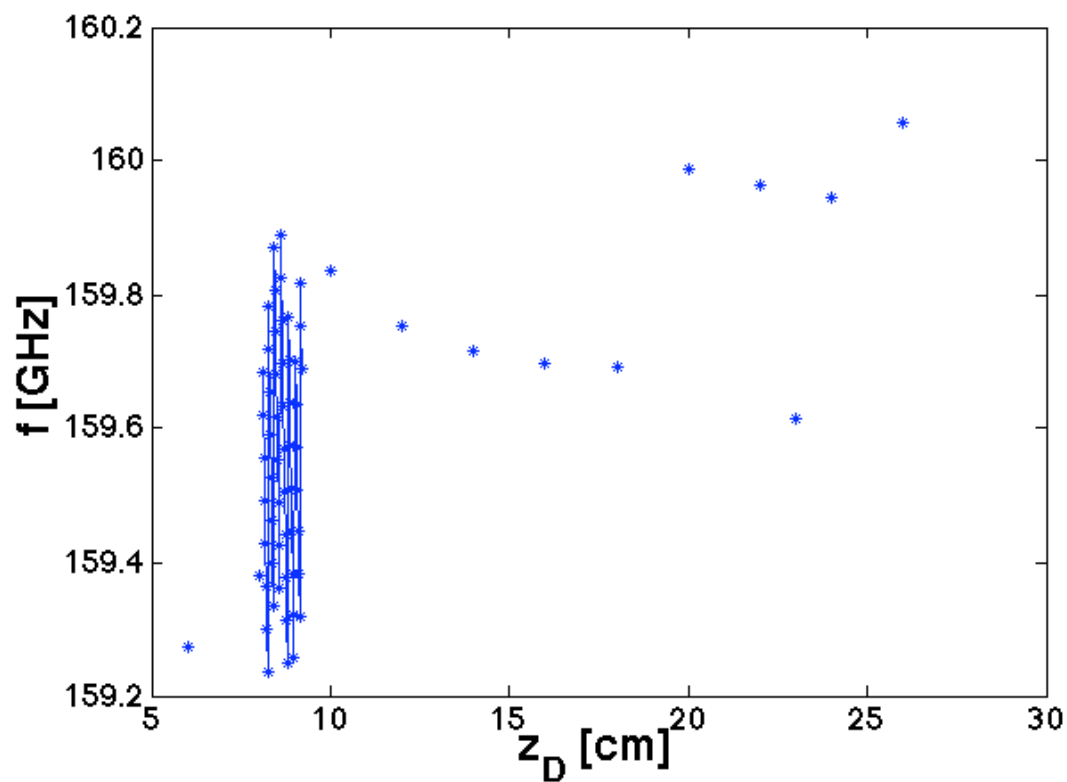


(c) for  $Z_s = 10.92\Omega$

**Fig. 3.12.** An example of  $\rho$  is plotted in complex plane by varying the frequency, which is for the gyrotron in Ref. 25 for different surface impedance.



(a)



(b)

**Fig. 3.13.** For the gyrotron structure in Ref. 25, the surface impedance (a) and frequency (b) are plotted as a function of the length of the tunnel.

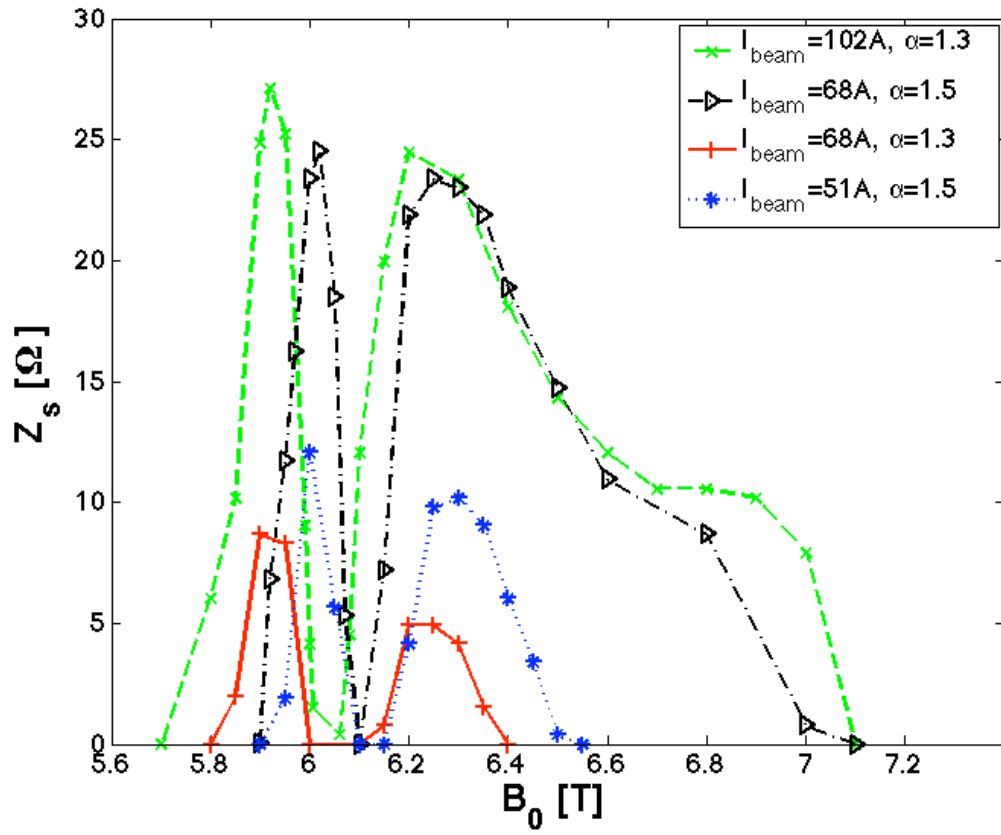


**Fig. 3.14.** Surface impedance needed to suppress the excitation for mode TE 24, 6 in the beam tunnel as function of the external magnetic field for different values of injected beam current and pitch factor for the gyrotron in Ref. 25.

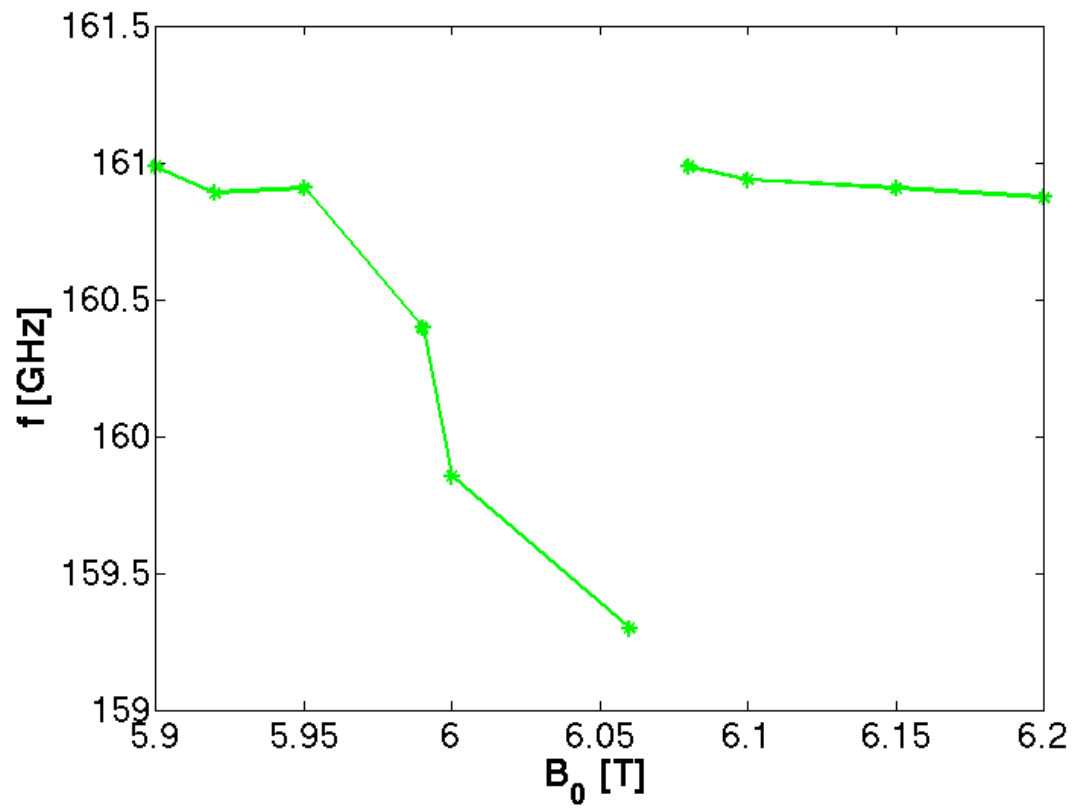


**Fig. 3.15.** Frequency of the unstable excitation for mode TE 24, 6 for the gyrotron in Ref. 25 with injected beam current  $I_{beam} = 102A$  and pitch factor  $\alpha = 1.3$ .

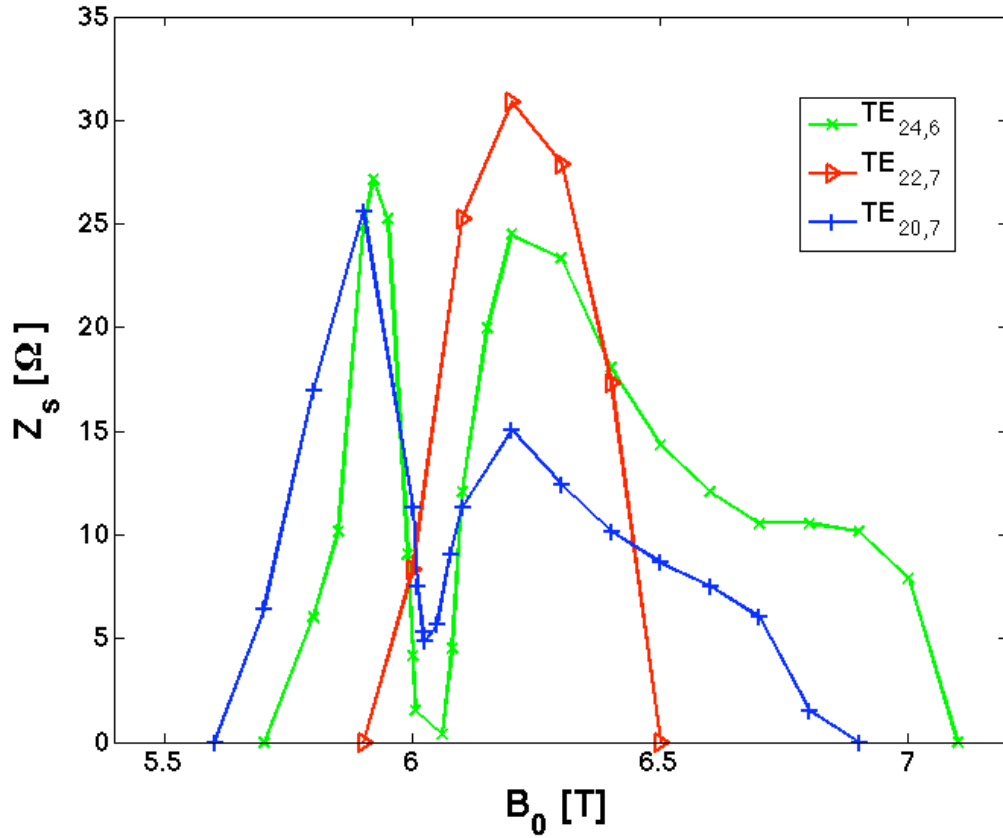


**Fig. 3.16.** Surface impedance needed to suppress the excitation in the beam tunnel as function of the external magnetic field for different modes for the gyrotron in Ref. 25 (It is assumed that injected beam current  $I_{beam} = 102A$  and pitch factor  $\alpha = 1.3$ ).

### 3.4 Conclusions

For the parameters and geometry considered, backward waves in a beam tunnel with a smooth wall will be stabilized if the surface impedance satisfies  $Z_s > 30\Omega$ . At the frequencies of interest,  $f \sim 160GHz$ , a coating material with a bulk conductivity  $\sigma = 57S/m$  will provide adequate surface impedance. Silicon carbon is a good example of the absorber. The most unstable modes are the ones whose cut-off frequency matches the cyclotron frequency at the point of minimum radius in the

beam tunnel. Note that the study of the effect of attenuation on the starting conditions in the gyro-BWO with constant parameters [41] shows that, when the attenuation is strong enough, the backward wave excitation becomes impossible at arbitrary beam currents.

The present small signal theory has made a number of approximations that need to be investigated for their validity. First we have neglected spreads in velocity. These are not expected to be significant as excited modes are close to the cut-off where the strongest interaction occurs. (Note that the effect of the axial velocity spread on the backward-wave excitation conditions in one specific design of a W-band gyro-BWO was studied in Ref. 45 where it was shown how this effect is increasing with the frequency departure from the cutoff.) Second, we have neglected the linear coupling between the modes that occurs when the wall is tapered. This effect has been shown to be important in the output taper of gyrotrons where it affects mode purity [46]. Finally, we have considered interaction between the beam and TE modes only. This neglects the so called electrostatic cyclotron maser instability [37] which may be important in beam tunnels and could interact with the BWO instability. Consideration of these last two effects will be the subject of next chapter.

## Chapter 4: Velocity Spread and Space Charge Effect in Gyrotron Beams

Two important effects were omitted from consideration in the previous chapter. These are velocity spread and the effect of AC space charge. In real magnetron injection guns electrons are to a good approximation monoenergetic. However, due to variation in electric field near the cathode, electrons have a distribution of values of their pitch factor  $\alpha = v_{\perp}/v_z$ . Typically, the spread in pitch angles is such that when the beam reaches the cavity there is a 5-10% spread in the relative value at  $v_{\perp}$ . The precise value of spread is hard to predict because it is affected by misalignments, surface roughness and nonuniform emission of the cathode, which are not easily quantified. A velocity spread of this level has modest effect on the operating mode because, in the cavity, the operating mode is near cut-off and has a small axial wavenumber. Thus there is little disruption of the cyclotron resonance due to Doppler shift. The same may not be true in the beam tunnel where potential BWO modes have considerable Doppler shift.

A second effect not considered is AC space charge. The instability considered in the previous section involved an electromagnetic field that was represented as a backward propagating TE mode. The bunched spiraling electron beam also produces an electrostatic field that, through the negative mass effect, can enhance bunching. In fact, the beam can be unstable in the absence of a backward wave due to the electrostatic cyclotron maser instability [48-51]. This mode is convectively unstable.

We will study the interaction of this mode with the BWO studied in the previous section.

In this chapter, we first repeat in section 4.1 our analysis for the CPI gyrotron as in Chapter 3. Later, in section 4.2, we include velocity spread into our calculation, and compare with the situation without spread. In the last section, the electrostatic instability in the gyrotron beam is considered.

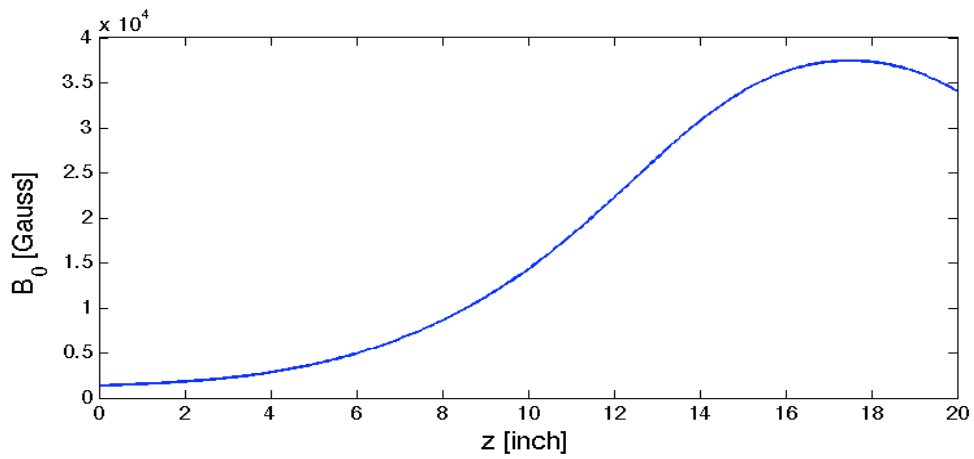
#### **4.1 CPI Gyrotron**

Our previous calculations are based on the structure of the JAERI 170GHz Gyrotron in Ref. 25, but at this point we change our focus to the CPI 95GHz Gyrotron [26]. The aim of CPI is to generate an output power at the 2 MW level with a 75 A beam current, but at this power level the efficiency appears to be limited by backward wave oscillation. We assume the beam tunnel to be a smooth wall, then the backward wave excitation in the beam tunnel is essentially the same as the JAERI Gyrotron. So we repeat our previous analysis in chapter 3 for the CPI Gyrotron in this section. The operating mode of the CPI Gyrotron is  $TE_{22,6}$ , with the magnetic field profile as in Fig. 4.1, beam tunnel shown in Fig. 4.2, and pitch factor  $\alpha = 1.62$  in the cavity.

The beam tunnel profile and three different possible beam positions ( $r_{\max}$ ,  $r_{\text{guide}}$ ,  $r_{\min}$ ) along the axis are shown in Fig. 4.2 together with the location of the coupling zeros (coupling coefficient equals zero) for the  $TE_{19,2}$  and  $TE_{8,5}$  modes. The coupling coefficient is defined in Eq. (4.1) as the strength of the coupling between the electron beam and backward wave,

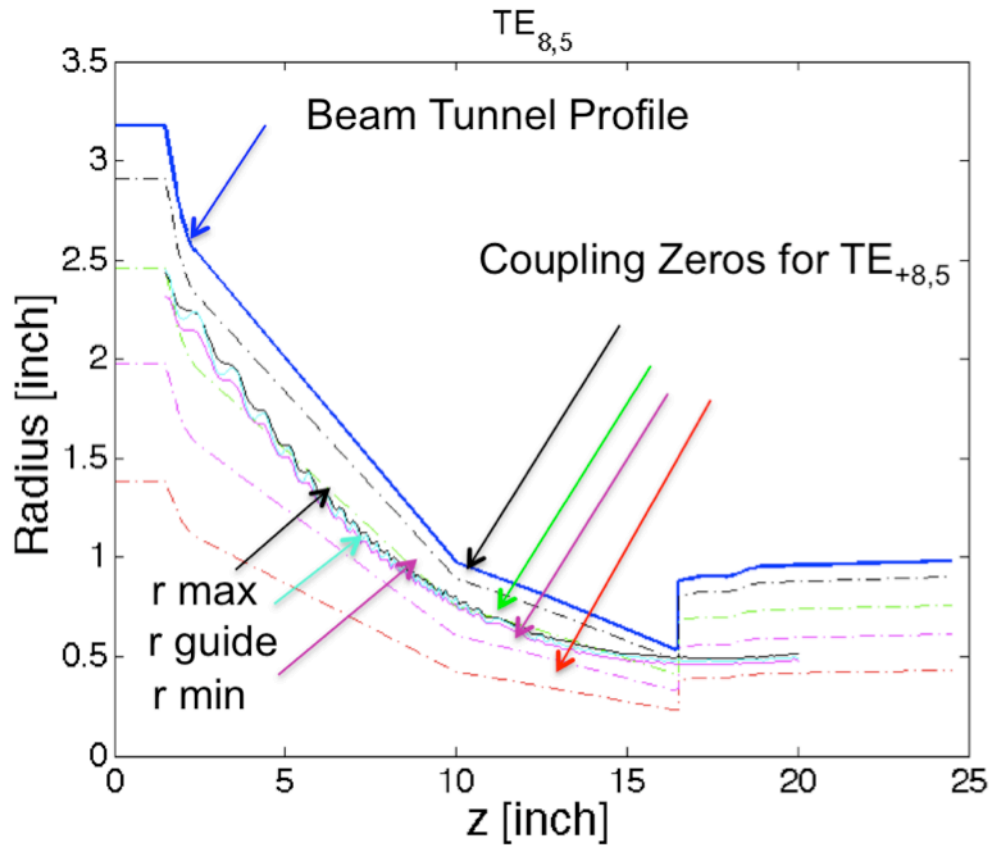
$$CouplingCoeff = \left[ \frac{J_{m+1}(j'_{m,n} r_b / R(z))}{J_m(j'_{m,n})} \right] \frac{1}{\pi(j'_{m,n}{}^2 - m^2)}, \quad (4.1)$$

where the positive and negative sign denotes the different direction of mode rotation relative to the electron gyration.

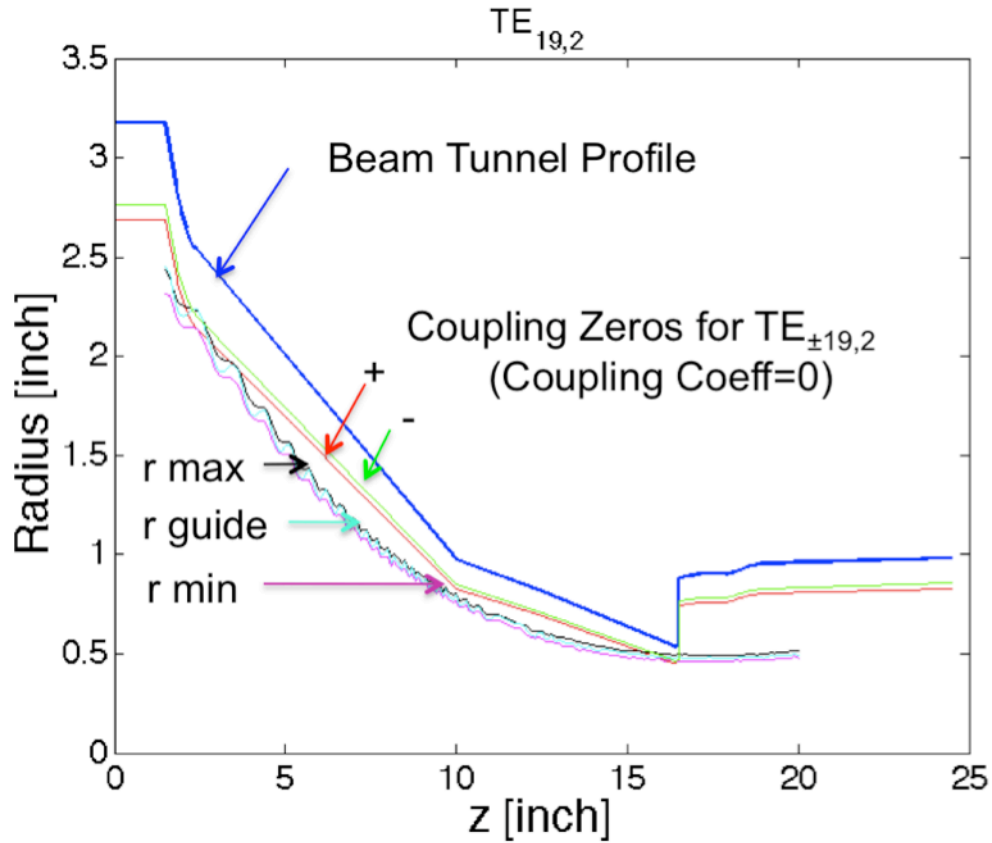


External Magnetic field profile

Fig. 4.1 Magnetic field profile of CPI Gyrotron



(a) Possible beam position and coupling zeros in the beam tunnel for mode  $TE_{8,5}$



(b) Possible beam position and coupling zeros in the beam tunnel for mode  $TE_{19,2}$

Fig. 4.2 Beam position and coupling zeros in the beam tunnel

The most unstable mode for each azimuthal index when the beam is at  $r_{\max}$  is listed in Fig. 4.3 along with its radial mode number. Here, instead of calculating the surface impedance needed to suppress a mode for a fixed injected beam current, we calculate the start current needed to excite an unstable mode with zero surface impedance. From the simulation we conclude that modes with eigenvalues close to 25.5 are more unstable than others. In Fig. 4.4, we plot the start current (a) as frequencies (b) of the modes listed in Fig. 4.3 for different beam positions. The unstable modes are in the range 85-90 GHz. In general, the start currents are much

larger than the nominal beam current (75A). Based on this one would assume that backward waves were stable in the CPI gyrotron. This will change when we introduce space charge effects. We can see from Fig. 4.4 that the  $TE_{19,2}$  has the smallest start current  $I_{st} = 93.5A$ , so it is the most unstable mode in the beam tunnel of the CPI Gyrotron. We indicated the unstable modes with negative azimuthal index for different beam positions in Fig. 4.4, others with positive index. The different beam positions lead to the largest start current variation for the  $TE_{8,5}$  mode and smallest variation for the  $TE_{19,2}$ . To analyze the cause of the variation of start current with different beam positions for different modes, we plot the coupling coefficients for different beam positions as function of  $z$  for the  $TE_{8,5}$  (a) and the  $TE_{19,2}$  (b) modes in Fig. 4.5. There is large difference in the integrated along  $z$  coupling coefficient for different beam positions for the  $TE_{8,5}$  mode, while only a small difference for the  $TE_{19,2}$  mode. Thus, variations in start current with beam radius for the  $TE_{8,5}$  and  $TE_{19,2}$  modes are caused by the different coupling coefficients.

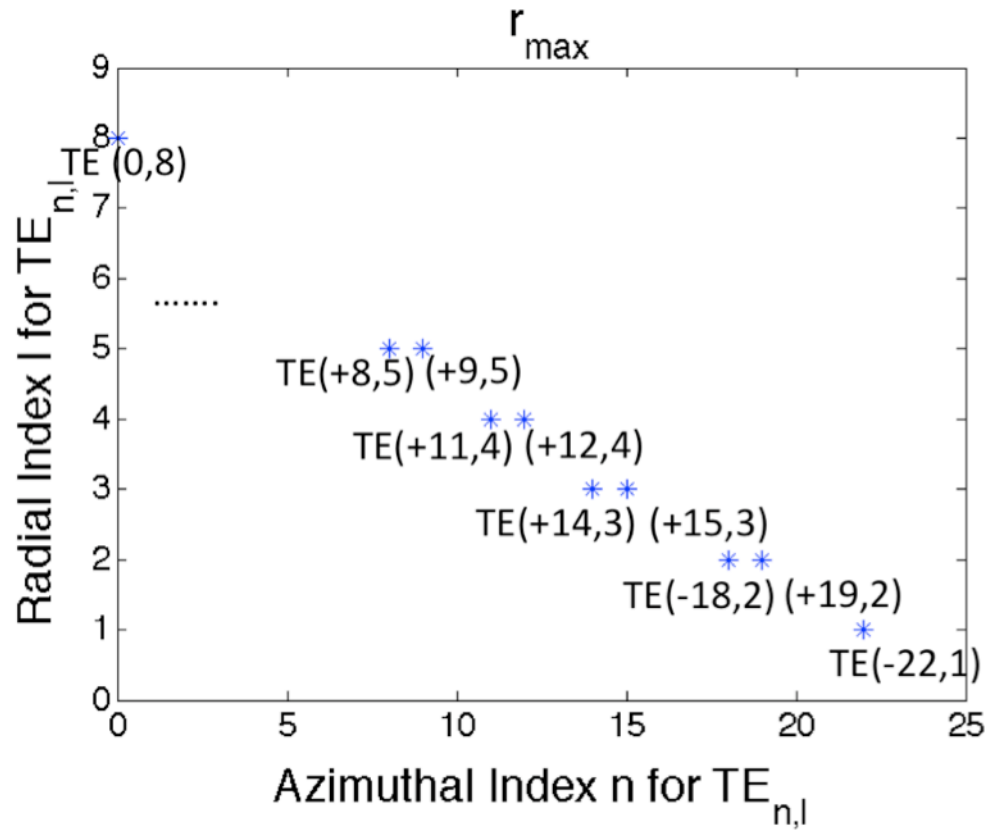
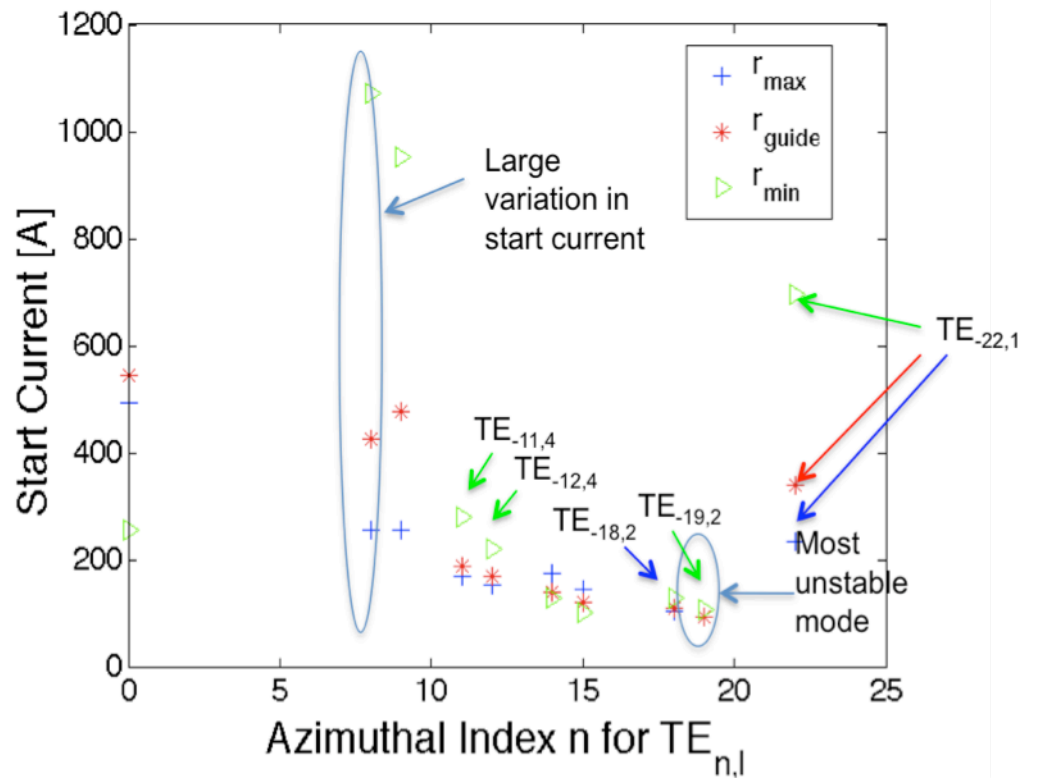
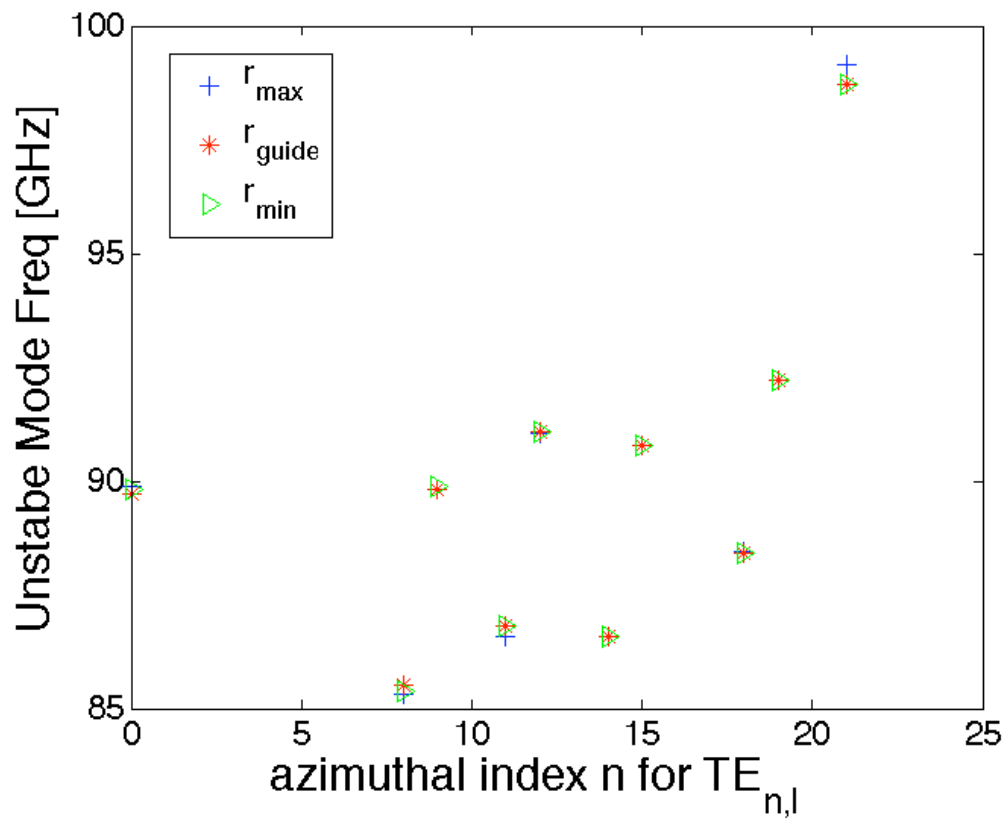


Fig. 4.3. Most unstable modes: their eigennumbers vary from 24.5 and 26.5.

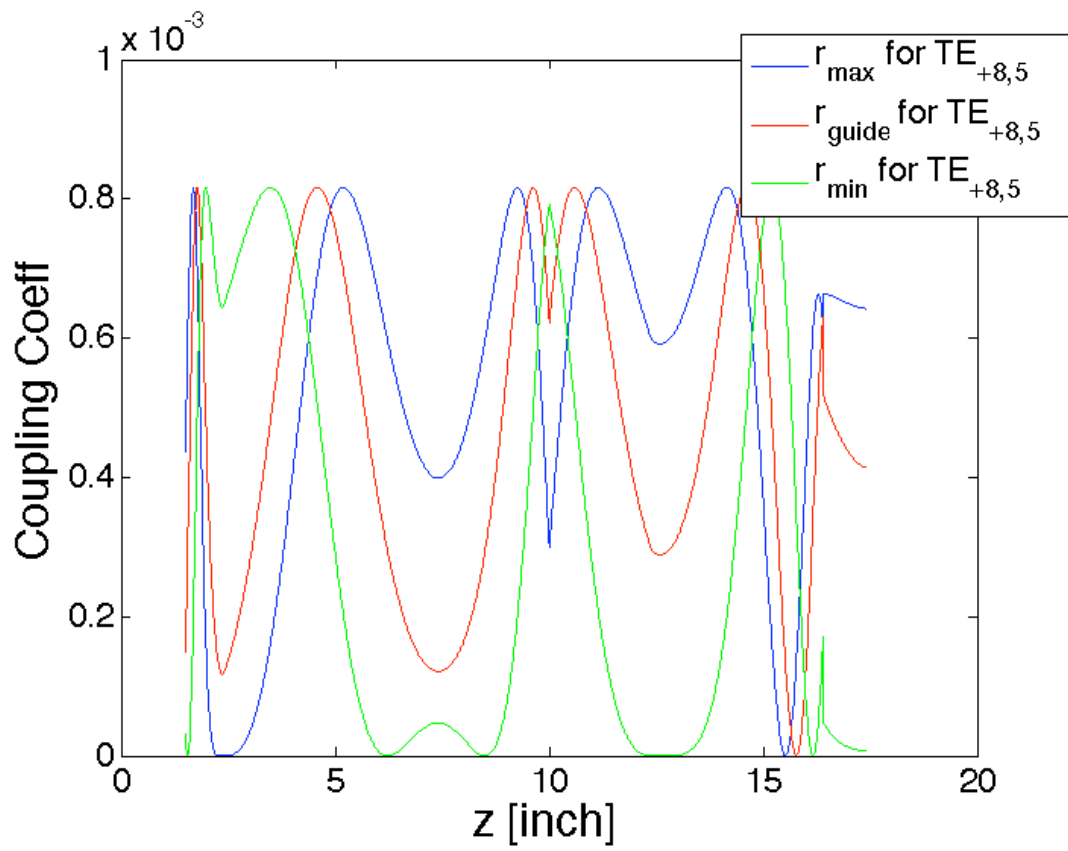


(a) Start current of most unstable modes

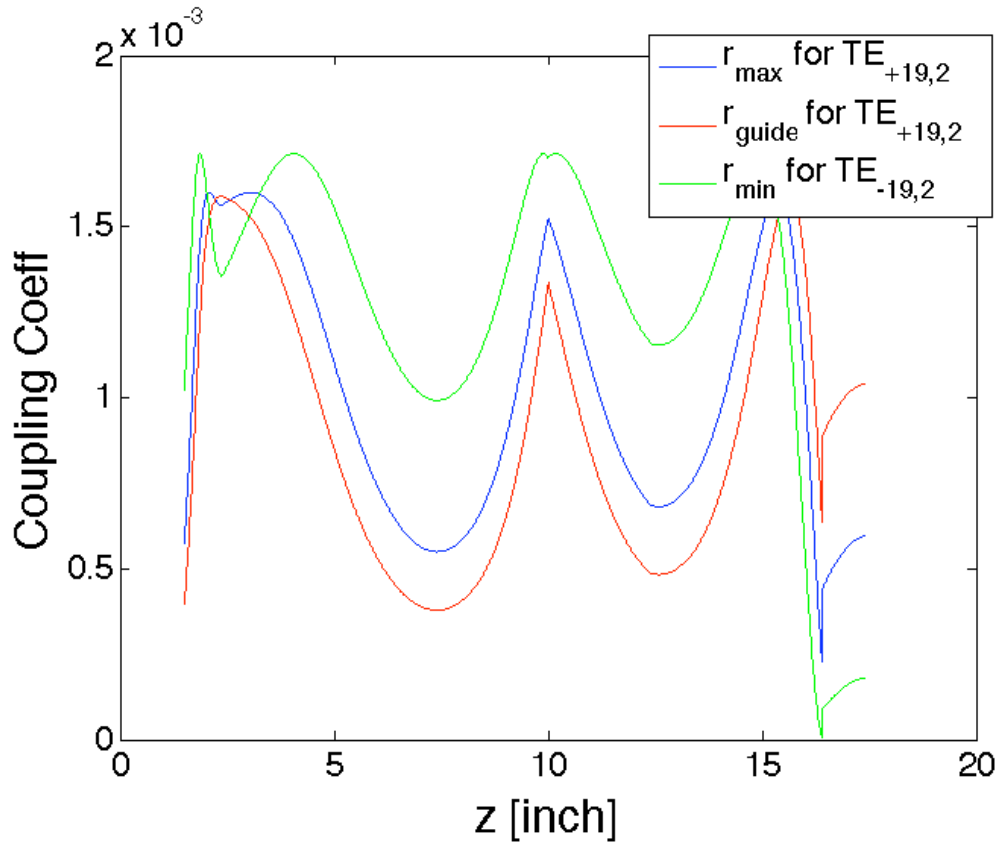


(b) Frequencies of most unstable modes

Fig. 4.4 Start current and frequencies of most unstable modes



(a)  $TE_{8,5}$



(b)TE<sub>19,2</sub>

Fig. 4.5. Coupling coefficients along z-axis for modes TE<sub>8,5</sub> and TE<sub>19,2</sub>

From our calculations so far, we could conclude that for the beam parameters of the CPI Gyrotorn, a current under 80A will not excite backward waves in the beam tunnel. However, when space charge effects are considered this will change.

#### 4.2 Velocity Spread

In gyrotrons, the source of electrons is usually a magnetron injection gun, which provides an annular electron beam that is monoenergetic, but has a spread in pitch angle, i.e. a spread in  $v_{\perp}/v_z$ . It was found in Ref. 47 that velocity spread weakens the

interaction between electrons and backward waves. Thus, the start current should increase when velocity spread is included.

To bring velocity spread into our calculation, the equations of motion Eq. 3.5 need to be solved for an ensemble of particles with different initial velocities. The wave equation Eq. 3.4 (a) needs to be modified to include a sum of contributions from different electrons  $\sum_i w_i S_{Tki}$ , where  $w_i$  is the weight of electrons with velocity  $\mathbf{v}_i$  and  $\sum_i w_i = 1$ . The equations of motion with velocity spread become

$$\hat{\phi}_0 = \int_0^z dz \frac{1}{\rho_{z0}} \left( \gamma_0 k_0 - \frac{\Omega_0(z)}{c} \right) \quad (4.2a)$$

$$\frac{\partial \delta \hat{\rho}_{\perp i}}{\partial z} = \frac{\gamma_0}{2\sqrt{R_B} \rho_{z0i}} \left( F_{\perp ks} \exp(-i\hat{\phi}_0) V_k \right) \quad (4.2b)$$

$$\frac{\partial \delta \hat{\gamma}_i}{\partial z} = \frac{\gamma_0 \rho_{\perp 0i} \sqrt{R_B}}{2\rho_{z0i}} \left( F_{\perp ks} \exp(-i\hat{\phi}_0) V_k \right) \quad (4.2c)$$

$$\frac{\partial \delta \hat{\phi}_i}{\partial z} = \frac{\delta \hat{\gamma}_i k_0}{\rho_{z0i}} - \frac{\delta \hat{\gamma}_i - \rho_{\perp 0i} R_B \delta \hat{\rho}_{\perp i}}{\rho_{z0i}^3} \left( \gamma_0 k_0 - \frac{\Omega_0}{c} \right) + \frac{\gamma_0}{2i\rho_{\perp 0i} \rho_{z0i} \sqrt{R_B}} \left( F_{\perp ks} \exp(-i\hat{\phi}_0) V_k \right) \quad (4.2d)$$

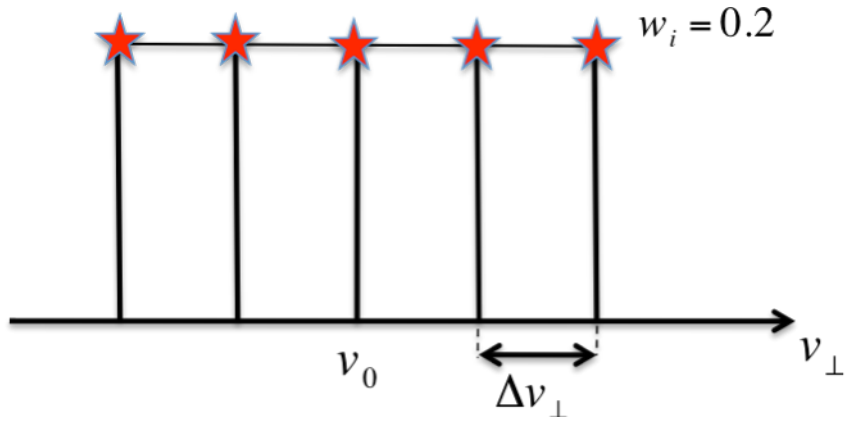
for each electrons, and the wave equation becomes

$$\left( -i \frac{1}{k_0} \frac{\partial^2}{\partial z^2} - ik_0 \left( 1 - \frac{\omega_{cut}^2}{\omega^2} \right) \right) V_k = -8\pi \frac{I}{I_A} \frac{\rho_{\perp 0i} \sqrt{R_B}}{\rho_{z0i}} F_{\perp ks}^* \exp(i\hat{\phi}_0) \sum_i w_i \left( \frac{\delta \hat{\rho}_{\perp i}}{\rho_{\perp 0i}} - \frac{\delta \hat{\gamma}_i - \rho_{\perp 0i} R_B \delta \hat{\rho}_{\perp i}}{\rho_{z0i}^2} + i\delta \hat{\phi}_i \right), \quad (4.2e)$$

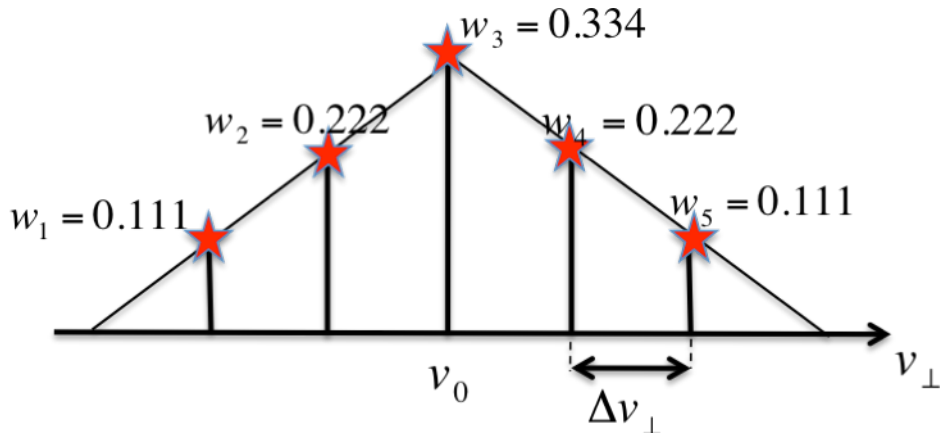
where  $\rho_{\perp 0i} = \gamma v_{\perp 0i} / c \sqrt{R_B}$  and  $\rho_{z0i} = \gamma v_{z0i} / c$  are for electrons with velocity  $\mathbf{v}_i$ .

Two example distribution functions for the perpendicular velocity (uniform and triangular) are shown in Fig. 4.6. We sample the distribution function at five equally spaced points. The root mean square (RMS variation of  $v_{\perp}$ ) is used to denote the

spread in velocity. Thus, for different values of RMS spread, the spaces  $\Delta v_{\perp}$  between spread velocities are different. For uniform distribution, and with five points the space between points is  $\Delta v_{\perp}/v_{\perp 0} = 0.0354$  for 5% velocity spread, and  $\Delta v_{\perp}/v_{\perp 0} = 0.0433$  for triangular. We found that with 15 interpolated points our calculations for uniform ( $\Delta v_{\perp}/v_{\perp 0} = 0.0012$  for 5% RMS spread) and for triangular ( $\Delta v_{\perp}/v_{\perp 0} = 0.0015$  for 5% RMS spread) are close.



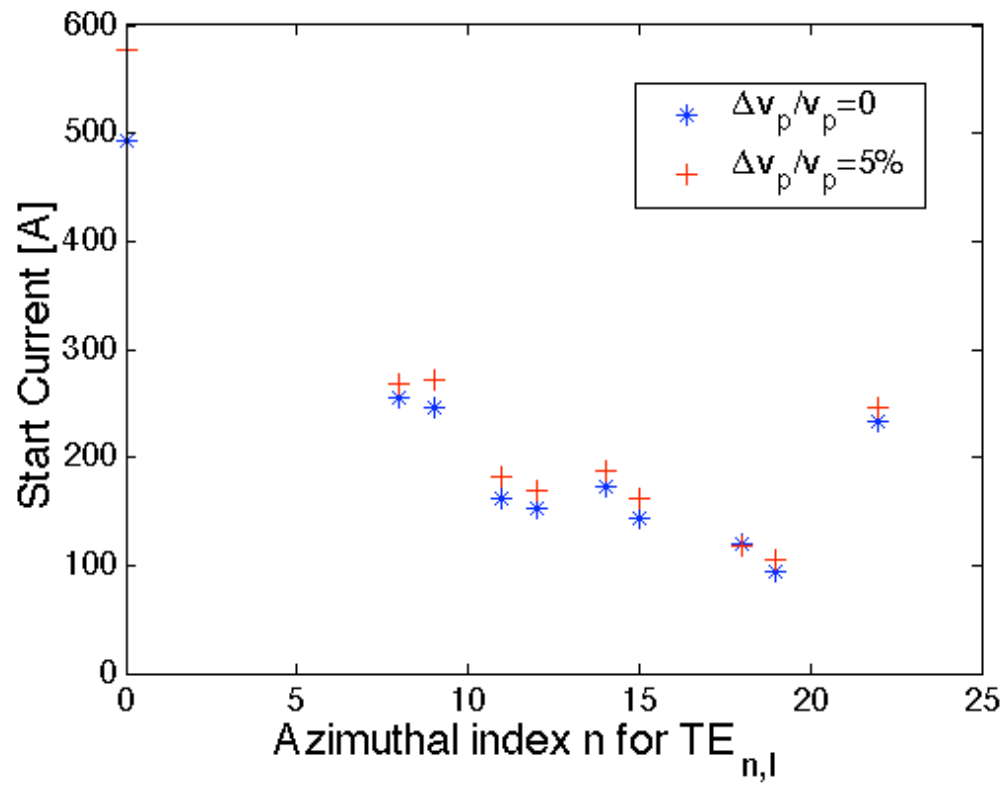
(a) Uniform distribution



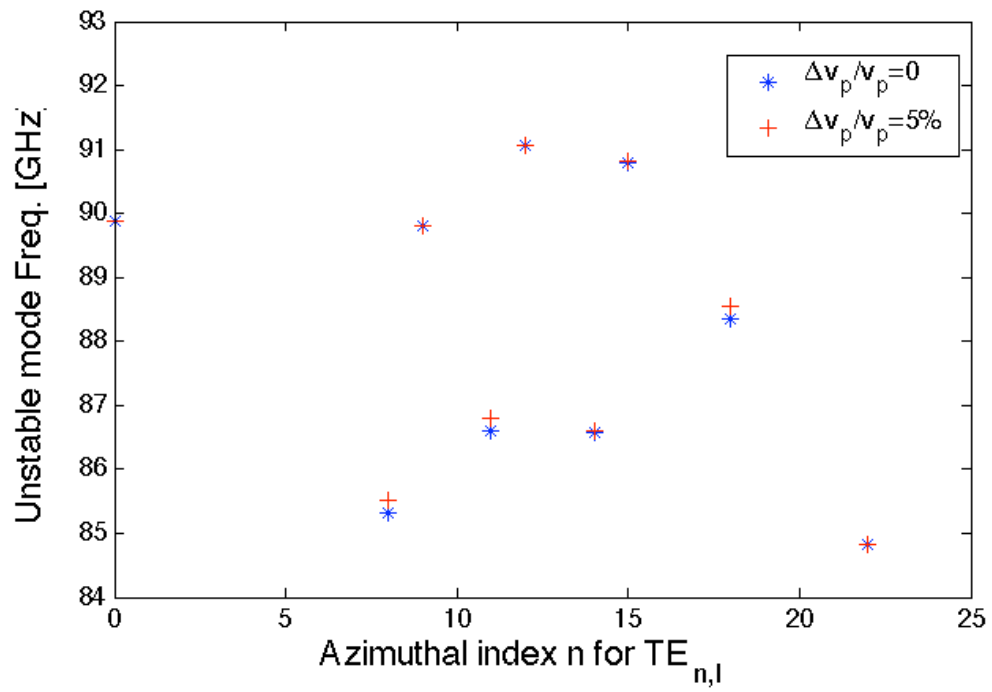
(b) Triangular distribution

Fig. 4.6. Velocity Spread distribution

The start current and frequency of the most unstable mode with 5% velocity spread is compared with cold beam in Fig. 4.7 when the beam guiding center at  $r_{\max}$ . We see that 5% velocity spread increases the start currents, but not much. The unstable frequencies remain the same. This is consistent with the conclusion in Ref. 47, where most growth of start current caused by the velocity spread is near the cutoff frequency. The start current is not sensitive to velocity spread, because  $k_z \approx 0$  there. The start current and most unstable mode frequencies as functions of the percentage of velocity spread for TE<sub>19,2</sub> mode are plotted in Fig. 4.8. We see that the start current increases as velocity spread increasing. A velocity spread of 12% doubles the start current needed to excite the instability in the tunnel. The most unstable mode frequency also increases as velocity spread increasing, but the varying amount is very small. The most unstable mode frequency for TE<sub>19,2</sub> is still around 92GHz.



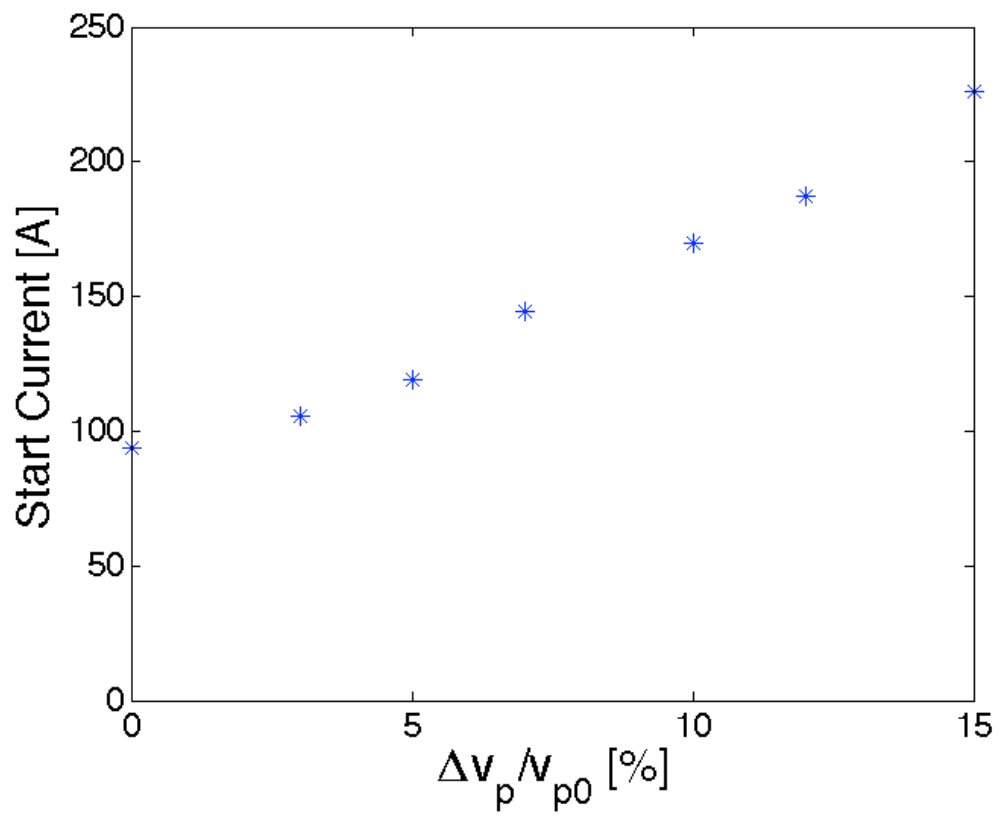
(a) Start current of the most unstable modes



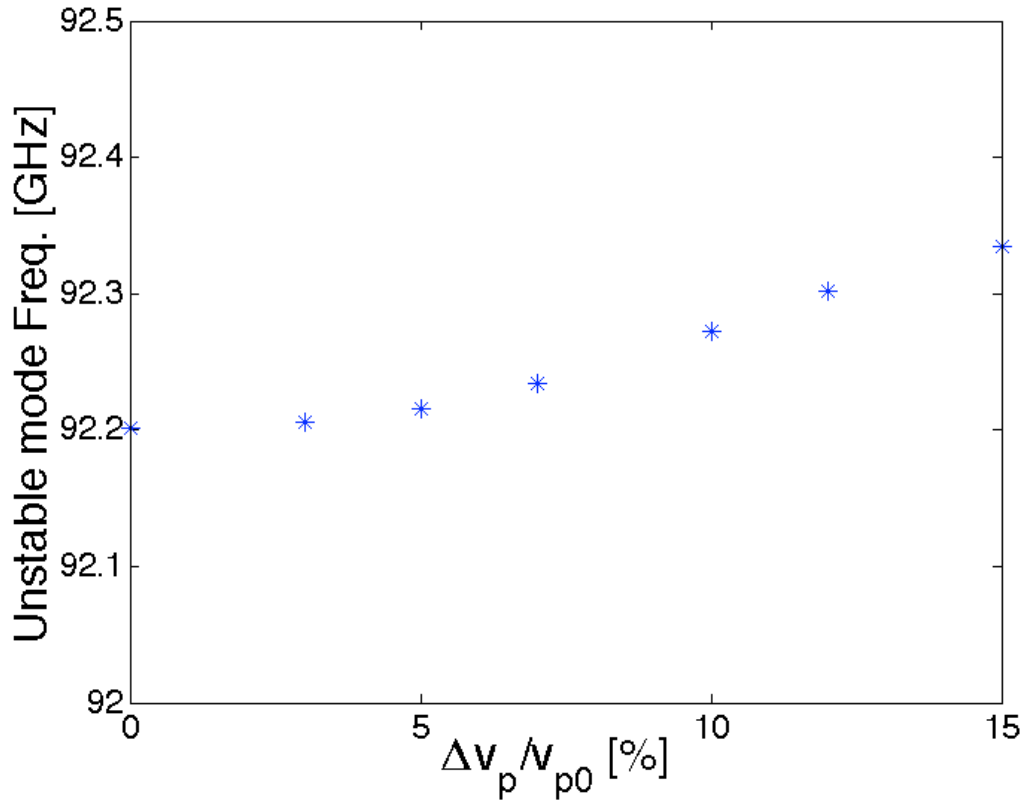
(b) Frequencies of most unstable modes

Fig. 4.7 Start current and frequencies of most unstable modes

for 5% velocity spread and no velocity spread



(a) Start current for beam with velocity spread



(b) Frequencies of most unstable modes

Fig. 4.8. Start current and frequencies as function of velocity spread for TE<sub>19,2</sub> mode

### **4.3 Coupling to the Electrostatic Cyclotron Maser Instability**

The spiraling electron beam, when it becomes bunched, produces a time dependent density perturbation and an associated electrostatic field. The analogous field, in the case of linear beam devices, gives rise to beam plasma waves that resist the formation of bunches. This was the phenomena studied in chapter 2. However, for a spiraling beam, due to the relativistic negative mass effect, the electrostatic field can enhance bunching. The associated unstable waves are known as the electrostatic

cyclotron maser instability, and they were originally studied by Hirshfield [48] and Charbit et.al [49]. Later, Chen and Chu [50] modeled the linear instability by monoenergetic electrons and Bonderson and Antonsen [51] pointed out the importance of an inhomogeneous magnetic field in stabilizing the perturbations.

The electrostatic cyclotron maser instability is convectively unstable. That is, the unstable perturbations propagate with the beam as they grow. Thus, previous studies [27, 48-51, 52-53] have focused on whether small levels of noise introduced near the cathode will be amplified to high enough level to degrade the beam by the time the beam reaches the cavity. Since the noise level is low, a large amplification is required to disrupt the beam, and due to the magnetic field inhomogeneity this level of amplification usually doesn't occur.

Considered here is a new phenomena, the coupling of backward waves with the electrostatic cyclotron maser instability. This coupling can result in absolute, rather than convective instability. The backward wave carries the signal from the cavity region to the cathode where the beam is perturbed. The perturbations are amplified as the beam propagates from the cathode to the cavity region where the backward wave is excited. Thus, there is a feedback loop that can give rise to absolute instability.

#### **4.3.1 Motion Equation**

The equations of motion are modified due to the presence of an additional component of electric field [37, 54]. The following modifications of the space charge effect can be made to the differential equations of  $\gamma v_{\perp}$  and  $\phi$ : [54]

$$\frac{d(\gamma v_{\perp})}{dt} = \dots + \frac{q}{2m} [\cos \phi E_{\phi}^s + \sin \phi E_{\phi}^c], \quad (4.3a)$$

$$\frac{d\phi}{dt} = \dots + \frac{q}{2m\gamma v_{\perp}} [-\cos \phi E_{\phi}^c - \sin \phi E_{\phi}^s], \quad (4.3b)$$

where  $E_{\phi}^s$  and  $E_{\phi}^c$  are the electrostatic contributions to the electric field, defining as

$$E_{\phi}^s = \frac{m \omega_p^2}{q \Omega_0} \sum_{\text{electrons}} w_p \sin \phi' \gamma' v'_{\perp}, \quad (4.4a)$$

$$E_{\phi}^c = \frac{m \omega_p^2}{q \Omega_0} \sum_{\text{electrons}} w_p \sin \phi' \gamma' v'_{\perp}. \quad (4.4b)$$

The sum is over all electrons,  $w_p$  is the weight of each electron ( $\sum_p w_p = 1$ ). By

transforming the derivatives with respect to  $t$  to derivatives with respect to  $z$ , and by substituting Eq. (4.4), we arrive at the following equations:

$$\begin{aligned} \frac{d(\gamma \beta_{\perp})}{dz} &= \dots + \frac{1}{v_z} \frac{d(\gamma v_{\perp}/c)}{dt} \\ &= \dots + \frac{1}{\beta_z} \frac{q}{2mc^2} [\cos \phi E_{\phi}^s + \sin \phi E_{\phi}^c] \end{aligned} \quad (4.5a)$$

$$\begin{aligned} \frac{d\phi}{dz} &= \dots + \frac{1}{v_z} \frac{d\phi}{dt} \\ &= \dots + \frac{1}{\gamma \beta_{\perp} \beta_z} \frac{q}{2mc^2} [-\cos \phi E_{\phi}^c - \sin \phi E_{\phi}^s] \end{aligned} \quad (4.5b)$$

We define a new space charge field amplitude, as

$$\varepsilon_{\phi}^{s,c} = \frac{q}{2mc^2} E_{\phi}^{s,c} = \frac{\omega_p^2}{2c\Omega_0} \sum_{\text{electrons}} w_p \begin{pmatrix} \sin \phi' \\ \cos \phi' \end{pmatrix} \gamma' \beta'_{\perp}, \quad (4.6)$$

the equations become

$$\frac{d(\gamma\beta_{\perp})}{dz} = \dots + \frac{1}{\beta_z} [\cos\phi\epsilon_{\phi}^s - \sin\phi\epsilon_{\phi}^c], \quad (4.7a)$$

$$\frac{d\phi}{dz} = \dots - \frac{1}{\gamma\beta_z\beta_{\perp}} [\cos\phi\epsilon_{\phi}^c + \sin\phi\epsilon_{\phi}^s]. \quad (4.7b)$$

By substituting the trigonometric relations  $\cos\phi\langle\sin\phi'\rangle - \sin\phi\langle\cos\phi'\rangle = \langle\sin(\phi' - \phi)\rangle$ ,

$\cos\phi\langle\cos\phi'\rangle + \sin\phi\langle\sin\phi'\rangle = \langle\cos(\phi' - \phi)\rangle$ , Eqs. (4.7) become

$$\begin{aligned} \frac{d(\gamma\beta_{\perp})}{dz} &= \dots + \frac{1}{\beta_z} \frac{\omega_p^2}{2c\Omega_0} \sum_{electrons} w_p \sin(\phi' - \phi) \gamma' \beta'_{\perp} \\ &= \dots - \frac{1}{\beta_z} \frac{\omega_p^2}{2c\Omega_0} \sum_{electrons} w_p \gamma' \beta'_{\perp} \Re\{ie^{i(\phi' - \phi)}\} \end{aligned} \quad (4.8a)$$

$$\begin{aligned} \frac{d\phi}{dz} &= \dots - \frac{1}{\gamma\beta_{\perp}\beta_z} \frac{\omega_p^2}{2c\Omega_0} \sum_{electrons} w_p \cos(\phi' - \phi) \gamma' \beta'_{\perp} \\ &= \dots - \frac{1}{\gamma\beta_{\perp}\beta_z} \frac{\omega_p^2}{2c\Omega_0} \sum_{electrons} w_p \gamma' \beta'_{\perp} \Im\{ie^{i(\phi' - \phi)}\} \end{aligned} \quad (4.8b)$$

By defining a complex space charge amplitude

$$K = \left( \frac{i\omega_p^2}{2c\Omega_0} \right) \langle \gamma\beta_{\perp} e^{i\phi} \rangle, \quad (4.9)$$

the equations can be further simplified as:

$$\frac{d(\gamma\beta_{\perp})}{dz} = \dots - \frac{1}{\beta_z} \Re\{K e^{-i\phi}\} \quad (4.10a)$$

$$\frac{d\phi}{dz} = \dots - \frac{1}{\gamma\beta_{\perp}\beta_z} \Im\{\mathbf{K}e^{-i\phi}\}. \quad (4.10b)$$

The change in particle energy can be related directly to the change in magnetic moment and  $\beta_{\perp}$  [55]. Thus yields,

$$\frac{\partial\gamma}{\partial z} = \dots \frac{\omega}{\Omega_0} R_B(\gamma\beta_{\perp}) \frac{\partial(\gamma\beta_{\perp})}{\partial z} \quad (4.11)$$

Adding Eq. (3.6) with Eq. (4.10), the differential equations of motion become with  $s = 1$ ,

$$\frac{\partial(\gamma\beta_{\perp})}{\partial z} = \frac{1}{\beta_z} \Re\{(V_k F_{\perp k} - \mathbf{K})\exp(-i\phi)\} + \frac{\gamma\beta_{\perp}}{2} \frac{\partial \ln B_0}{\partial z}, \quad (4.12a)$$

$$\frac{\partial\phi}{\partial z} = \frac{1}{\beta_z} \left( \frac{k_0}{s} - \frac{\Omega_0}{\gamma c} \right) + \frac{1}{\gamma\beta_z\beta_{\perp}} \Im\{(V_k F_{\perp ks} - \mathbf{K})\exp(-i\phi)\}, \quad (4.12b)$$

Then the normalized differential equations for  $\rho_{\perp}$ ,  $\gamma$  and  $\phi$  are

$$\frac{\partial(\rho_{\perp})}{\partial z} = \frac{\gamma}{\rho_z \sqrt{R_B}} \Re\{(V_k F_{\perp k} - \mathbf{K})\exp(-i\phi)\}, \quad (4.13a)$$

$$\frac{\partial\gamma}{\partial z} = \frac{\sqrt{R_B} \rho_{\perp} \gamma}{\rho_z} \Re\left\{ \left( V_k F_{\perp k} - \frac{\omega}{\Omega_0} K \right) \exp(-i\phi) \right\}, \quad (4.13b)$$

$$\frac{\partial\phi}{\partial z} = \frac{1}{\rho_z} \left( \gamma k_0 - \frac{\Omega_0}{c} \right) + \frac{\gamma}{\rho_z \rho_{\perp}} \Im\{(V_k F_{\perp k} - K)\exp(-i\phi)\}. \quad (4.13c)$$

By applying the same small signal model to Eq. (4.13) and averaging over the unperturbed electron trajectories as we did in Chapter 3, the equations Eq. (4.13) become

$$\frac{\partial \hat{\rho}_{\perp}}{\partial z} = \frac{\gamma_0}{2\sqrt{R_B} \rho_{z0}} (F_{\perp ks} V_k - \mathbf{K}) \exp(-i\hat{\phi}_0) \quad (4.14a)$$

$$\frac{\partial \delta \hat{\gamma}}{\partial z} = \frac{\sqrt{R_B}}{2} \frac{\rho_{\perp 0} \gamma_0}{\rho_{z0}} \left( F_{\perp ks} V_k - \frac{\omega}{\Omega_0(z)} K \right) \exp(-i \hat{\phi}_0) \quad (4.14b)$$

$$\frac{\partial \delta \hat{\phi}}{\partial z} = \frac{\delta \hat{\gamma} k_0}{\rho_{z0}} - \frac{\delta \hat{\gamma} - \rho_{\perp 0} R_B \delta \hat{\rho}_{\perp}}{\rho_{z0}^3} \left( \gamma_0 k_0 - \frac{\Omega_0}{c} \right) + \frac{\gamma_0}{2i \rho_{\perp 0} \rho_{z0} \sqrt{R_B}} (F_{\perp ks} V_k - K) \exp(-i \hat{\phi}_0), \quad (4.14c)$$

where the expression for  $K$  defined in Eq. (4.9) becomes

$$K = \frac{i \omega_p^2}{2c \Omega_0} \sqrt{R_B} \rho_{\perp 0} \exp(i \hat{\phi}_0) \left( \frac{\delta \hat{\rho}_{\perp}}{\rho_0} + i \delta \hat{\phi} \right) \quad (4.15)$$

The above equations together with Eq. (3.11e), describe the interaction of the space charge and backward wave excitation in the beam tunnel of a gyrotron.

### 4.3.2 Space-charge spatial growth

To analyze the space-charge effect on the beam only, we turn off the backward wave temporarily, i.e.  $V_k = 0$ , also set  $\gamma \omega - \Omega_0 = 0$ . Assuming the third term in Eq. (4.14c) is small compared to the first term and substituting  $K$  with Eq. (4.15), the equations of motion Eq. (4.14) become

$$\delta \hat{\gamma} = \frac{\rho_{\perp 0} R_B}{\gamma_0} \delta \hat{\rho}_{\perp} \quad (4.16a)$$

$$\frac{\partial \delta \hat{\rho}_{\perp}}{\partial z} = -\frac{\gamma_0 \rho_{\perp 0}}{2 \rho_{z0}} \frac{i \omega_p^2}{2c \Omega_0} \left( \frac{\delta \hat{\rho}_{\perp}}{\rho_{\perp 0}} + i \delta \hat{\phi} \right) \quad (4.16b)$$

$$\frac{\partial \delta \hat{\phi}}{\partial z} = \delta \hat{\gamma} \frac{k_0}{\rho_{z0}} \quad (4.16c)$$

In case of constant external magnetic field ( $R_B = 1$ ), and looking for spatially varying solutions of the form  $\delta\phi = A\exp(ikz)$  and  $\delta\rho = B\exp(ikz)$ , we obtain a second order equation of  $k$ :

$$k^2 + \frac{\gamma_0\omega_p^2}{4c\Omega_0\rho_{z0}}k + \frac{\gamma_0\omega_p^2}{4c\Omega_0}\frac{\rho_{\perp 0}^2}{\rho_{z0}^2\gamma_0}k_0 = 0. \quad (4.17)$$

Substituting  $k = k_r - ik_i$  in to Eq. (4.17), the spatial growth rate of the perturbed quantities  $k_i$  is

$$k_i = \frac{1}{2} \frac{\omega_p}{c} \frac{v_{\perp 0}}{v_{z0}\sqrt{\gamma_0}}. \quad (4.18)$$

This is consistent with the spatial growth rate of space charge calculated in Ref. 37 by solving the Vlasov equation in the homogenous beam limit. The dispersion equation from Ref. 37 is written as

$$1 - \frac{\omega_p^2\gamma}{4\gamma_z^2\Omega_0^2} \left( \frac{\gamma v_{\perp 0}}{c} \right)^2 \left( \frac{k_z^2 c^2 - \omega^2}{d(\omega, k_z)} \right) = 0, \quad (4.19)$$

where  $\gamma_z = \left(1 + \gamma^2 v_{z0}^2 / c^2\right)^{1/2}$ ,  $d(\omega, k_z) = \left(\gamma\omega - k_z u_{z0} - \Omega_0\right)^2$  when the thermal velocity spread of the electron speed can be neglected. We solve this dispersion equation by letting  $k_z = (\gamma\omega - \Omega_0)/u_{z0} + ik_i$ , then

$$k_i = \frac{\omega_p\gamma^{1/2}}{\gamma_z\Omega_0} \frac{v_{\perp 0}}{2v_{z0}c} \left( \omega^2 - \frac{c^2(\gamma\omega - \Omega_0)^2}{\gamma^2 v_{z0}^2} \right)^{1/2}. \quad (4.20)$$

The two terms in Eq. (4.20) originate from gyrophase and axial bunching respectively. Gyrophase bunching is destabilizing, while axial bunching is stabilizing. The most unstable case occurs when  $\gamma_0\omega - \Omega_0 = 0$ , so the second term is 0. Then

$$k_i = \frac{1}{2} \frac{\omega_p v_{\pm 0}}{v_{z0} c \gamma_0^{1/2}}, \quad (4.21)$$

which agrees with our result, Eq. (4.18).

For the situation when the velocity spread can not be neglected,  $d(\omega, k_z) = (\gamma\omega - k_z u_{z0} - \Omega_0)^2 - \frac{1}{4} k_z^2 \Delta u_z^2$ . The last term stands for the axial momentum spread. This term suppresses the instability when  $k_z \equiv (\omega - \Omega_0/\gamma)/v_{z0}$  is large. This will be important in the beam tunnel where the cyclotron frequency varies with  $z$ .

### 4.3.3 Results and analysis

We now consider the growth of fields in the CPI beam tunnel with inhomogeneous magnetic field and varying wall radius. Fig. 4.9 compares the spatial growth of the perturbed transverse velocity with backward wave (BWO) and electron cyclotron maser instability (ECM) for  $TE_{+19,2}$  mode. For initial condition in the case with ECM only we set  $\delta p_{\perp} = 0.01$ ,  $\delta\gamma = 0$  and  $\delta\phi = 0$ . The profile for ECM only is not strictly exponential growing because of magnetic field varying. The oscillation is caused by the interaction with the backward wave. By comparing between profiles for BWO only and for BWO and ECM, we see that electron cyclotron maser increases the instability in the tunnel.

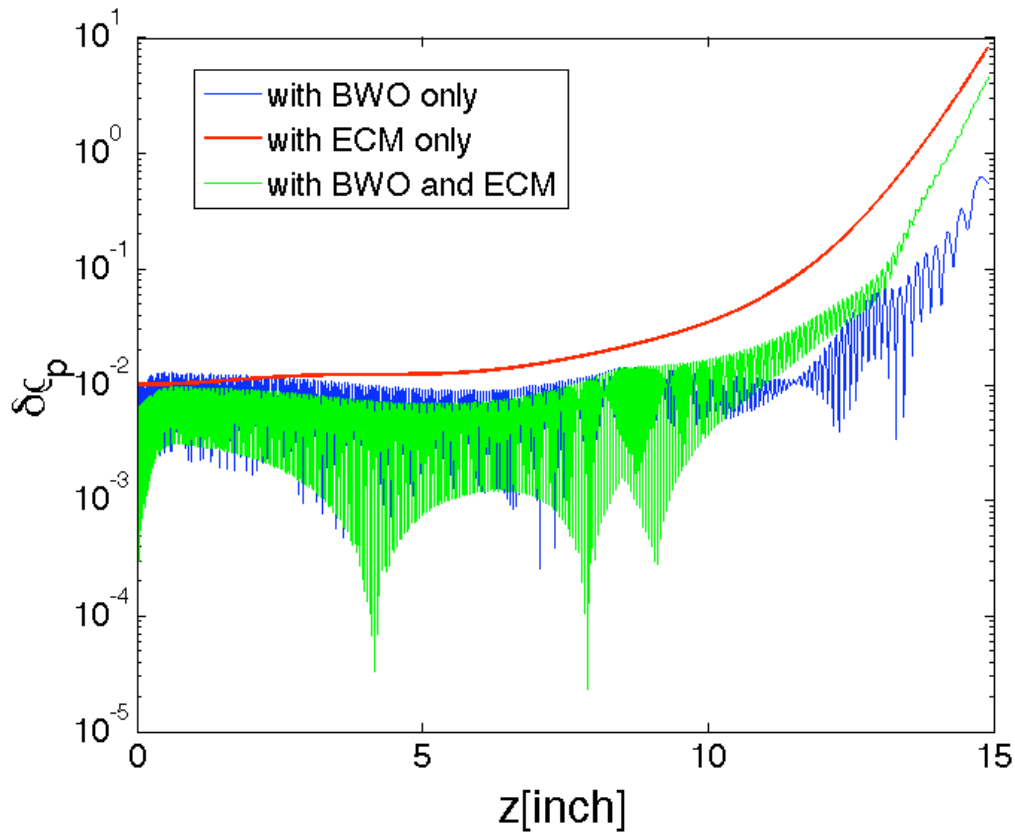
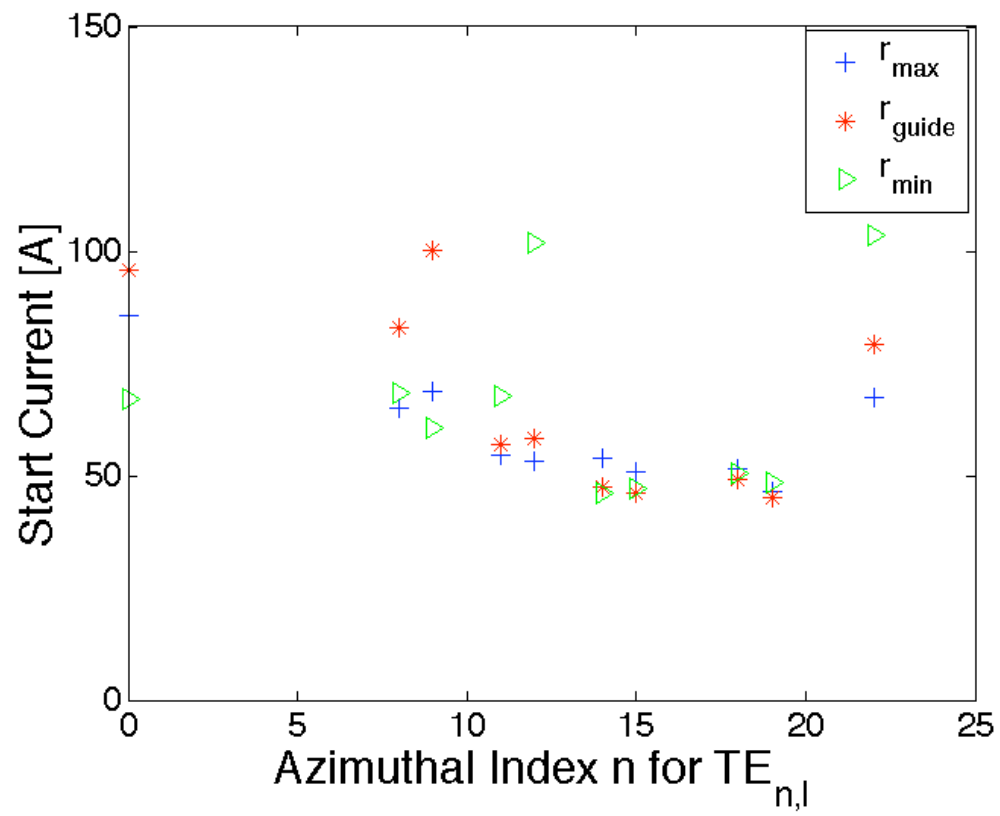
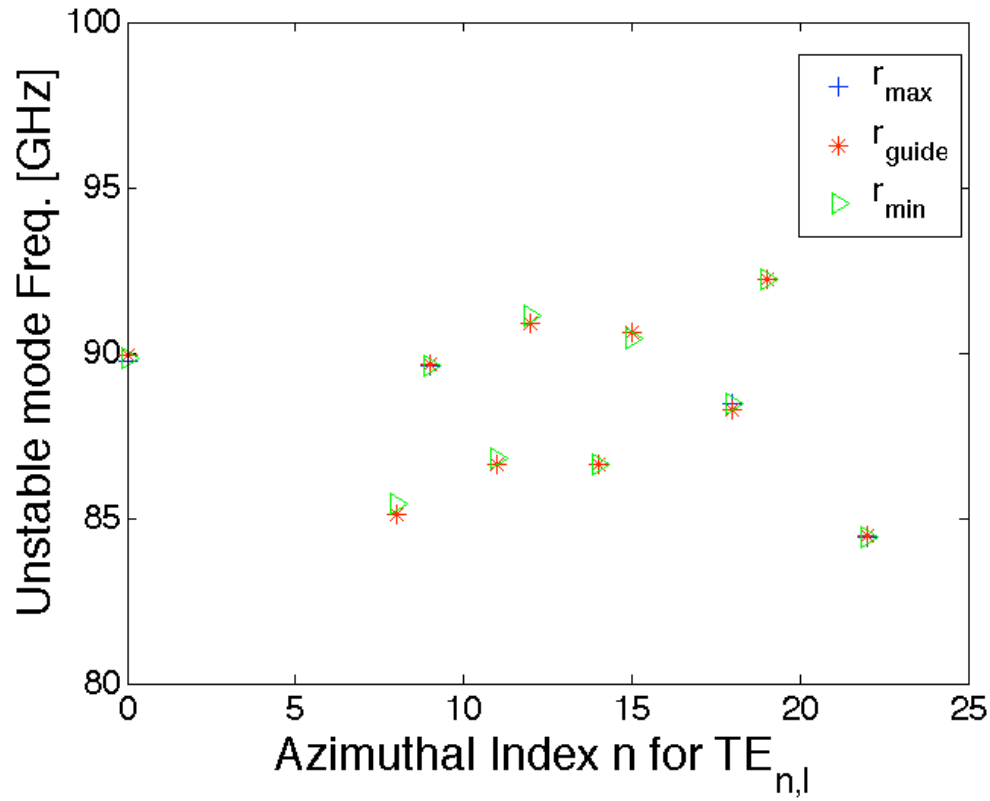


Fig. 4.9. Perturbations in the electron orbital momentum in a tapered magnetic field with and without interaction with backward wave.

The start current and frequencies of the most unstable modes considering electron cyclotron instability at different beam center positions are listed in Fig. 4.10. Compared with plots in Fig. 4.4, we see that space charge reduces the start current substantially, i.e. space charge greatly increases the instability of the backward wave. At the same time, the space charge doesn't affect the frequencies of the most unstable modes. We also see that the beam position doesn't affect the start current as much as for the situation with no space charge.



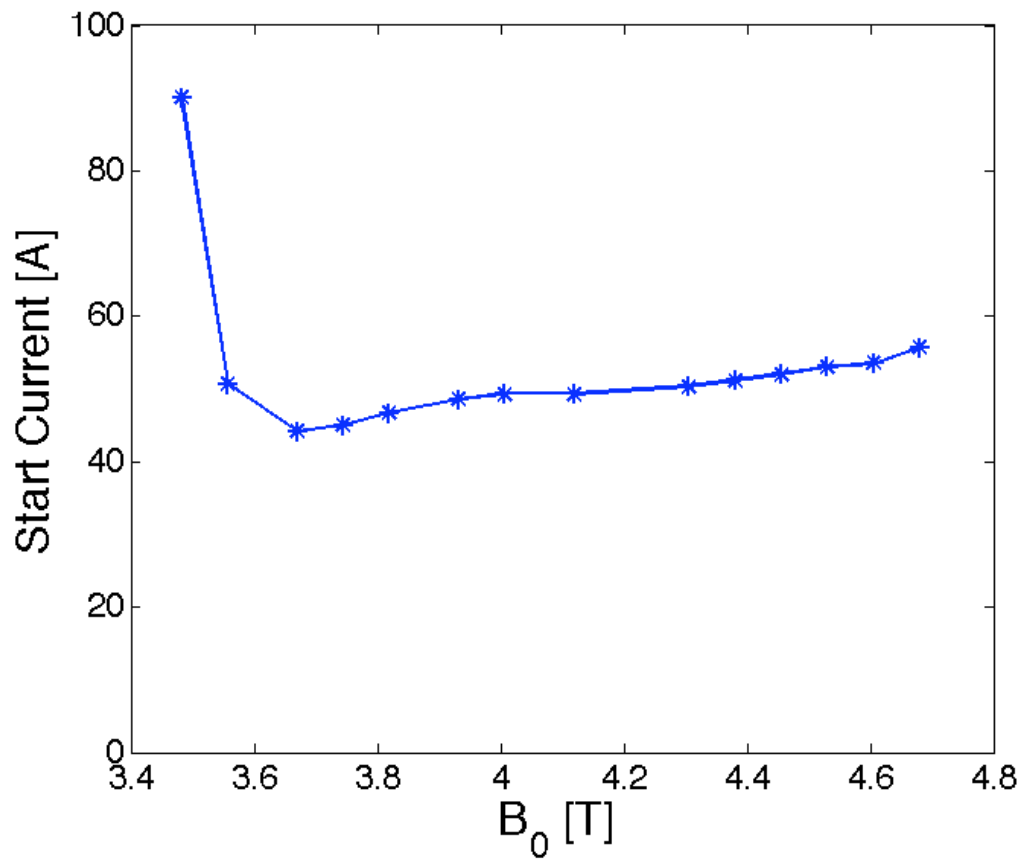
(a) Start Current of most unstable modes



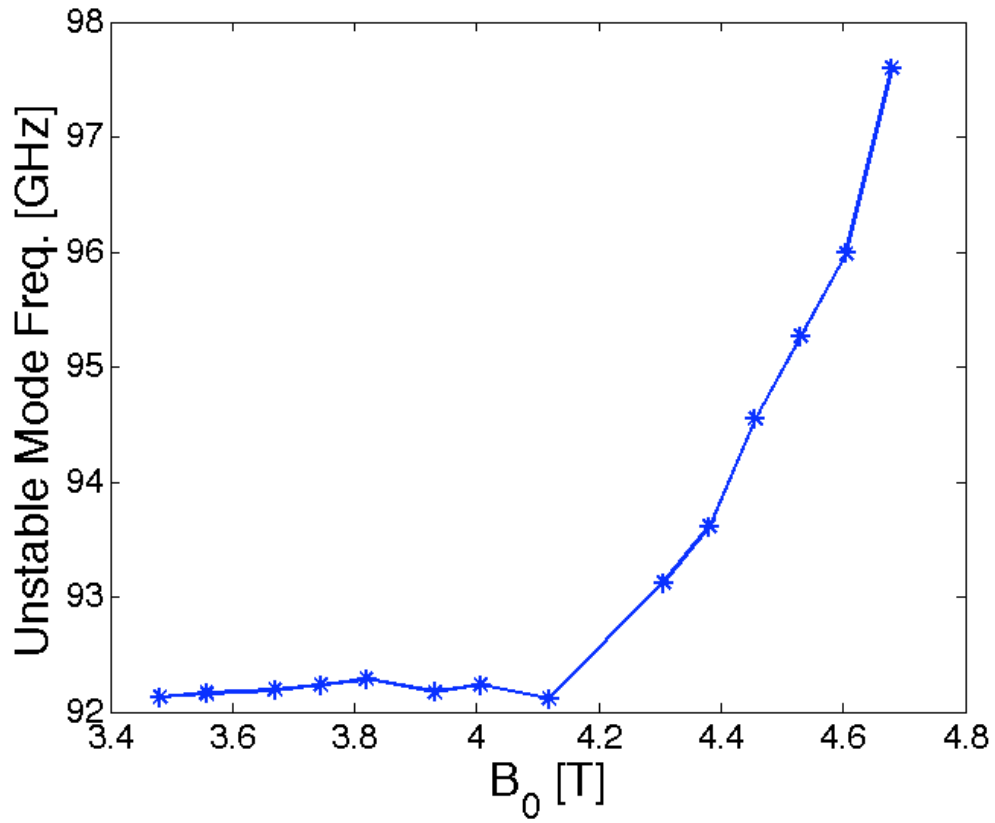
(b) Frequencies of most unstable modes

Fig. 4.10. Start current and frequencies of most unstable modes without and with space-charge effect with beam center at  $r_{\max}$ ,  $r_{\text{guide}}$  and  $r_{\min}$

In Fig. 4.11, the start current and most unstable mode frequencies are plotted as function of external magnetic field. Start current decreases and then increases with external magnetic field in Fig. 4.11(a), which is caused by the transit of excitation from forward wave to backward wave. The unstable mode frequency increases with external magnetic field in Fig. 4.11(b). This proportional relation can be explained by the cyclotron resonance condition in Eq. (3.1).

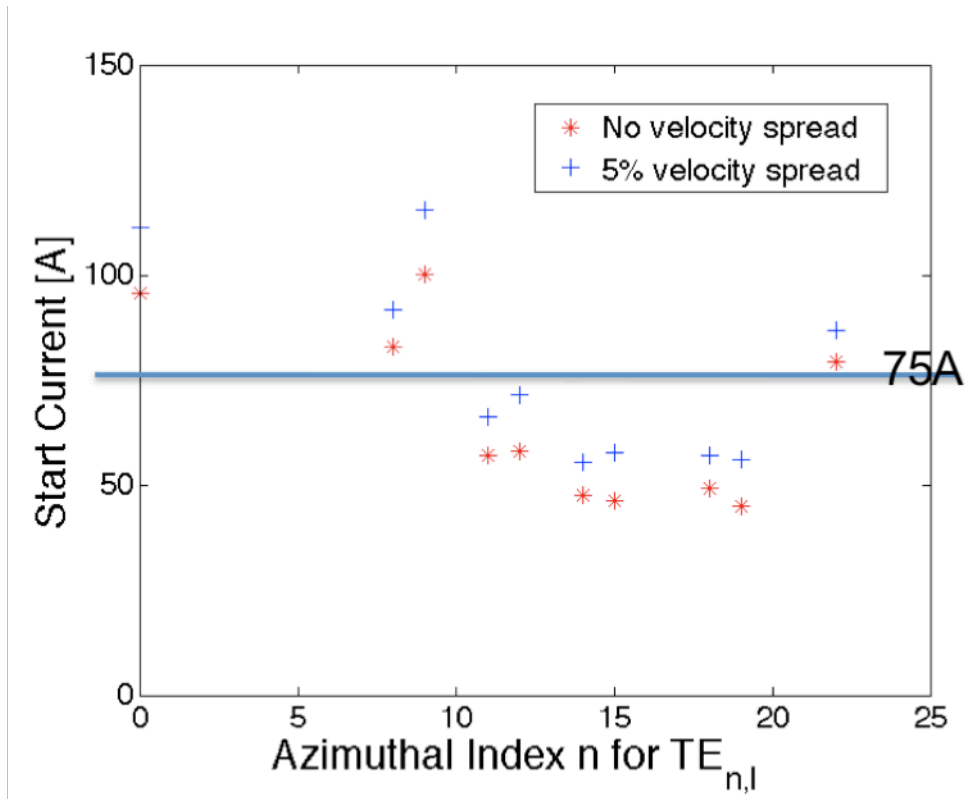


(a) Start current of most unstable modes

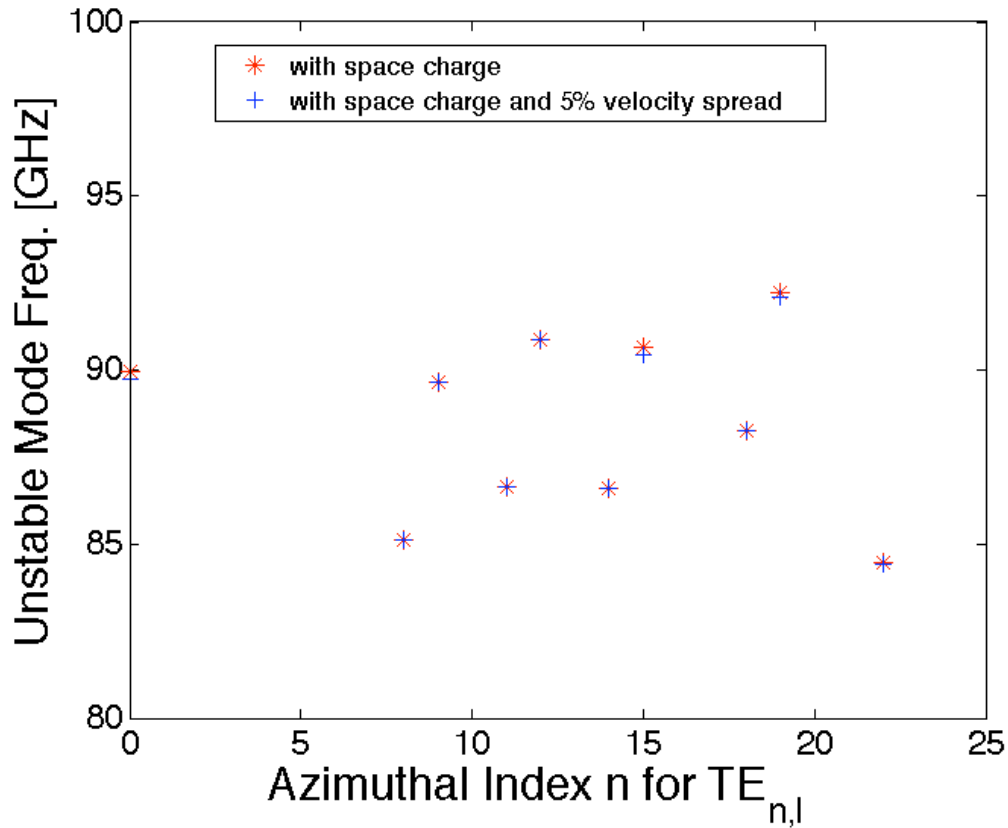


(b) Frequencies of most unstable modes

Fig. 4.11. Start current and Frequencies of unstable modes as function of external magnetic field



(a) Start current of most unstable modes



(b) Frequencies of most unstable modes

Fig. 4.12. Start current and Frequencies of most unstable modes with space charge effect, without and with 5% velocity spread

We consider both the space-charge effect and velocity spread in our calculation in Fig. 4.12 for beam guiding center at  $r_{guide}$ . The velocity spread still increases the start current. Here an 8% velocity spread doubles the start current. But, velocity spread doesn't affect the frequency.  $TE_{+19,2}$  is still the most unstable mode in the beam tunnel of CPI Gyrotron. A beam current larger than 60A can excite the backward wave.

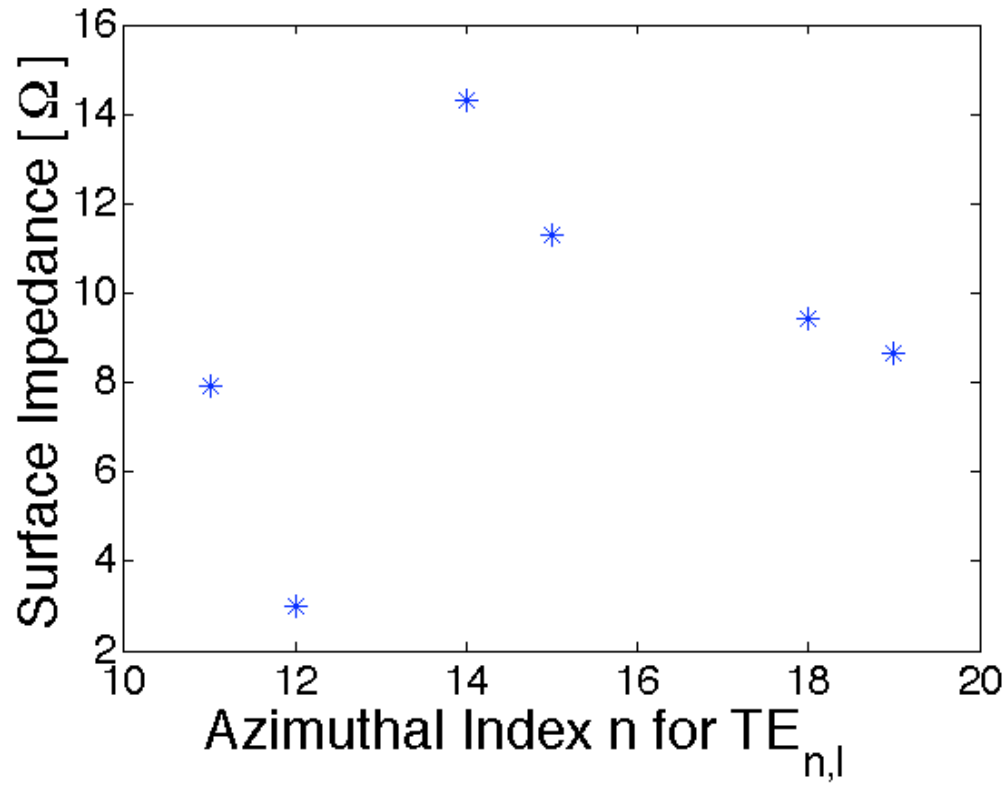


Fig. 4.13. Surface Impedance needed to suppress instability in beam tunnel with 75A beam current considering both space charge effect and 5% velocity spread.

For the desired 75A beam current of CPI Gyrotron, modes  $TE_{+11,4}$ ,  $TE_{+12,4}$ ,  $TE_{+14,3}$ ,  $TE_{+15,3}$ ,  $TE_{+18,2}$  and  $TE_{+19,2}$  can be excited in the beam tunnel when the beam guiding center is  $r_{guide}$ . The surface impedances needed to suppress the instability considering

both space charge effect and 5% velocity spread for the unstable modes are listed in Fig. 4.13. We see that a surface impedance of  $15\Omega$  can suppress the instability.

#### **4.4 Conclusion**

Our calculation provides a more accurate and general estimate of start current needed to excite backward wave excitation and the surface impedance of the absorbing material placed on the inner surface to suppress the instability in the beam tunnel of CPI Gyrotron by taking velocity spread and space charge effect into our calculation. The most unstable mode for this specific gyrotron is  $TE_{19,2}$ . The start current is around 60A. In the same way, our calculation can also be applied to other high power gyrotrons, and will be very helpful to enhance their efficiency.

## Appendix A: Structure parameters

In this appendix, we analyze a rectangular grating of the type shown in Fig. 1.2. The purpose is to find the properties of the structure field needed for both the basic (low density) theory, and for the elements of the reactance matrix needed to determine the effect of self-fields.

The field above the grating surface ( $x>0$ ) is expressed in Eqs. (2.1a-2.1c),  $E_{zn}$  and  $B_{yn}$  are related by Eq. (A-1), which is derived from Maxwell equations. The 0<sup>th</sup>-harmonic term is expressed in Eqs. (2.12), and 1<sup>st</sup>-harmonic term is given in Eqs. (2.10).

$$B_{yn} = \frac{-i\omega/c}{(k_{zn}^2 - \omega^2/c^2)} \frac{\partial}{\partial x} E_{zn} \quad (\text{A-1})$$

Meanwhile, the field in one of the grating slots is given by

$$E_z(x,z) = \sum_{m=1}^{\infty} E_{zm}^{(g)} \cos(k_m z) \frac{\sinh(k_m^<(x+d))}{\cosh(k_m^<d)} + E_{z0}^{(g)} \cos(k_0 z) \frac{\sin(\omega(x+d)/c)}{\cos(\omega d/c)} \quad (\text{A-2a})$$

$$B_y(x,z) = \sum_{m=1}^{\infty} B_{ym}^{(g)} \cos(k_m z) \frac{\cosh(k_m^<(x+d))}{\cosh(k_m^<d)} + B_{y0}^{(g)} \cos(k_0 z) \frac{\cos(\omega(x+d)/c)}{\cos(\omega d/c)} \quad (\text{A-2b})$$

Here,  $k_m = m\pi/w$ ,  $k_m^< = \sqrt{k_m^2 - \omega^2/c^2}$ ,  $B_{ym}^{(g)}$  and  $E_{zm}^{(g)}$  are also related by Eq. (A-1).

The field components  $E_z$  and  $B_y$  are continuous at  $x=0$ , and we note that the  $E_z$ -field on the metallic surface is zero. We match the  $E_z$ -field by multiplying both  $E_z$  expressions (Eq. (2.1a) and Eq. (A-1a)) by  $e^{-i(\bar{k}_z + nk_0)z}$  then integrating  $z$  from 0 to  $p$  in the case of Eq. (2.1a) and 0 to  $w$  in case of Eq. (A-1a). This generates a set of equations  $E_{zn} = \sum_m T_{nm} E_{zm}^{(g)}$ , where  $T_{nm} = \int_0^w (dz/p) e^{-i(\bar{k}_z + nk_0)z} \cos(k_m z)$ . Doing a similar

process for the  $B_y$ -field, except multiplying both Eq. (2.1c) and Eq. (A-1b) by

$\cos(k_m z)$ , generates  $B_{ym}^{(g)} = \sum_n N_m T_{mn}^* B_{yn}$ , here  $N_m = (p/w) / \int_0^w (dz/w) \cos^2(k_m z)$ . At

$$x=0, \quad E_{zn}^{(g)} = i \xi_m B_{ym}^{(g)} \quad (\text{derived from (A-1)}), \quad \xi_0 = -\tan(kd) \quad \text{and}$$

$\xi_m = (k_m c / \omega) \tanh(k_m c d)$ . This leads to a matrix relation between the different spatial harmonics of the magnetic and electric fields above the grating surface,

$$E_{zn} = i \sum_n Z_{nn} B_{yn} \quad (\text{A-3})$$

$$\text{with } Z_{mn} = \sum_m T_{nm} \xi_m T_{mn}^*$$

We next use Eq. (A-1) to express  $B_{yn} = i \tilde{\xi}_n E_{zn}$  for  $n \neq 0,1$ , where

$$\tilde{\xi}_n = (\omega/c) (k_{zn}^2 - \omega^2/c^2)^{-1/2}. \quad \text{We then solve}$$

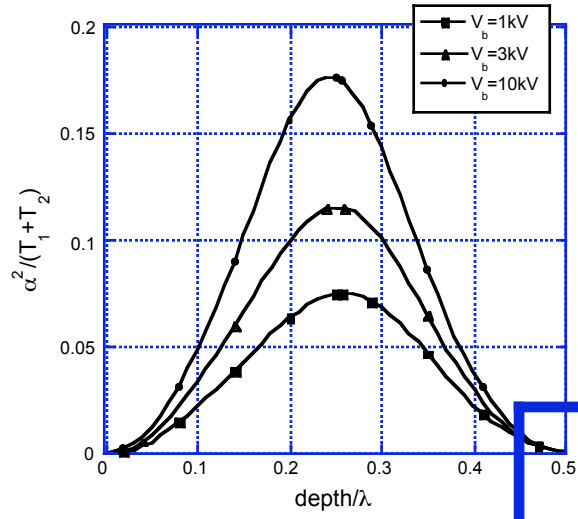
$$E_{zn} + \sum_{n \neq 0,1} Z_{nn} \tilde{\xi}_n E_{zn} = \sum_{n \neq 0,1} i Z_{mn} B_{yn} \quad (\text{A-4})$$

for  $E_{zn}$  for  $n \neq 0,1$  in terms of  $B_{y0}$  and  $B_{y1}$ . Substituting this back into Eq. (A-4) now for  $n=0$  and  $n=1$  gives linear relations between  $E_{z0,1}$  and  $B_{y0,1}$ . These relations are then expressed in the form of Eq. (2.11).

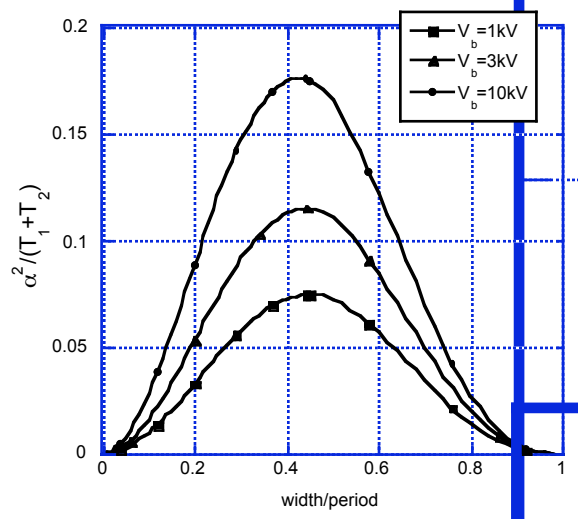
Two grating dependent quantities are needed to evaluate the start current: the strength of first spatial harmonic relative to the incident wave amplitude  $\alpha^2$  and the geometric surface loss factor  $T$ . The factor  $\alpha$  is determined by solving Eqs. (2.11) - (2.14) in the absence of a beam, with  $r=0$  in Eq. (2.14). The factor  $T$  can be calculated once the fields in the case of a perfectly conducting grating are known. In general the  $n=0$  spatial components of the tangential electric and magnetic fields are related by the complex surface impedance  $\hat{E}_{z0} = \hat{Z}_s \hat{B}_{y0}$ , the coefficient  $T$  is defined in terms of the real part of  $\hat{Z}_s$ ,  $\text{Re}\{\hat{Z}_s\} \equiv TR_s/Z_0$ , where  $R_s$  is the surface impedance of

the metal from which the grating is constructed. For small values of  $R_s/Z_0 \ll 1$ , we have  $T = \int dl |\vec{B}_t|^2 / \int dz |\hat{B}_{y0}|^2$ . Here  $\vec{B}_t$  is the component of magnetic field tangent to the metal surface and the integration  $dl$  is along the grating metal surface. Therefore  $T$  equals 1 for flat surface.

We know from Eq. (2.7), that the start current density is inversely proportional to  $\alpha^2/(T_1 + T_2)$ , where  $T_1$  is the geometric loss factor for the parabolic metal mirror, which is approximately 1,  $T_2$  corresponds to the grating surface. Figure (A-1) shows us how the quantity  $\alpha^2/(T_1 + T_2)$  changes with grating depth and width. The peak value is achieved by varying both the grating width and depth. Figure (A-1a) shows the dependence on depth with width fixed  $w = 0.44p$ . The peak occurs around  $d/\lambda = 0.252$ . Figure (A-1b) shows the dependence on width with  $d/\lambda = 0.252$ . Here the peak occurs for  $w = 0.44p$ .



(a)



(b)

Fig. A-1, (a) is plot of  $\alpha^2 / (T_1 + T_2)$  versus  $depth/\lambda$  (keep  $width/period=0.442$ )  
 (b) is for  $\alpha^2 / (T_1 + T_2)$  versus  $width/period$  (keep  $depth/\lambda=0.252$ )

## Appendix B: Cavity modes with $k$ -dependent reflectivity

The evaluation of gain and loss that determines the start current described by Eq. (2.15) involves integration of both gain and loss over wave number. This relation is derived here.

Near the surface of the grating, the fundamental spatial harmonic fields have the character of counter propagation plane waves as described by Eq. (2.12). The reflected wave amplitude (upward propagation) is related to the incident wave amplitude (downward propagation) by the reflection coefficient  $\rho$  that includes the interaction with the beam.

The waves will diffract as they propagate back and forth between the mirror and the grating. The incident and reflected wave fields at the mirror surface  $x_m = L_x - \Delta x(z)$  are given by:

$$E_{inc,refl}(z, x_m(z)) = \int \frac{d\tilde{k}_z}{2\pi} [\bar{E}_{inc,refl}(\tilde{k}_z) e^{\mp i\varphi(z)}],$$

where  $\varphi(z) = (\omega^2/c^2 - \tilde{k}_z^2)^{1/2}(L_x - \Delta x(z))$ , and are related to each other by  $E_{inc}(z, L_x - \Delta x) = \rho_m E_{refl}(z, L_x - \Delta x)$ , where  $\rho_m = e^{i\pi + \eta_m}$  is the reflection coefficient of the metallic mirror surface where  $\eta_m < 0$  and  $\eta_m \ll 1$  in the small loss limit.

We expand the phase  $\varphi(z)$  using the assumption  $\omega L_w/c \gg 1$ , and define

$$\theta(\tilde{k}_z) = \tilde{k}_z^2 L_x / (2\omega/c),$$

$$\begin{aligned}
E_{refl}(z, L_x - \Delta x) &= \int \frac{d\tilde{k}_z}{2\pi} e^{i\tilde{k}_z z} \bar{E}_{refl}(\tilde{k}_z) e^{ik_x(L_x - \Delta x(z))} \\
&\approx \int \frac{d\tilde{k}_z}{2\pi} \bar{E}_{refl}(\tilde{k}_z) \exp\left[i\tilde{k}_z z + i\frac{\omega}{c}(L_x - \Delta x(z)) - i\theta(\tilde{k}_z)\right]
\end{aligned} \tag{B-1a}$$

and

$$E_{inc}(z, L_x - \Delta x) \approx \int \frac{d\tilde{k}_z'}{2\pi} \bar{E}_{inc}(\tilde{k}_z') \exp\left[i\tilde{k}_z' z - i\frac{\omega}{c}(L_x - \Delta x(z)) + i\theta(\tilde{k}_z')\right] \tag{B-1b}$$

We then use the relationship between the amplitudes at the mirror surface  $E_{inc} = \rho_m E_{refl}$  and at the grating surface with  $\bar{E}_{refl}(\tilde{k}_z) = \rho(\tilde{k}_z) \bar{E}_{inc}(\tilde{k}_z)$ , and inverse Fourier Transform to obtain an integral equation for the wavenumber dependence of the incident field

$$\bar{E}_{inc}(\tilde{k}_z'') = e^{-i\theta(\tilde{k}_z'')} \int \frac{d\tilde{k}_z}{2\pi} \rho_m \rho(\tilde{k}_z) \kappa(\tilde{k}_z'' - \tilde{k}_z) e^{2i\frac{\omega}{c} - i\theta(\tilde{k}_z)} \bar{E}_{inc}(\tilde{k}_z) \tag{B-2}$$

where  $\kappa(\tilde{k}_z'' - \tilde{k}_z) = \int_{-\infty}^{\infty} e^{-2ik_x \Delta(z) + i(k_z - \tilde{k}_z'')z} dz$ .

We now consider perturbations to the case of a perfectly reflecting grating and mirror.

The two reflection coefficients are written as  $\rho_m \equiv e^{i\pi}(1 + \eta_m)$ ,  $\rho(\tilde{k}_z) = e^{i\phi_0}(1 + \eta(\tilde{k}_z))$ .

Also let  $\bar{E}_{inc}(\tilde{k}_z) = \bar{E}_{inc}^{(0)}(\tilde{k}_z) + \bar{E}_{inc}^{(1)}(\tilde{k}_z)$ ,  $\omega = \omega^{(0)} + \omega^{(1)}$ , which is complex determining frequency and growth rate. Here all quantities with superscript “0” refer to the case of perfectly reflecting surfaces, and those with superscript “1” are perturbations of these quantities when losses and the beam are included.

The 0<sup>th</sup> order of Eq. (B-2) defines the unperturbed eigenfunction and cavity frequency.

$$\bar{E}_{inc}^{(0)}(\tilde{k}_z'') = e^{-i\theta(\tilde{k}_z'')} \int \frac{d\tilde{k}_z}{2\pi} e^{i(\pi + \phi_0) + 2i\frac{\omega^{(0)}}{c}L_x - i\theta(\tilde{k}_z)} \kappa(\tilde{k}_z'' - \tilde{k}_z) \bar{E}_{inc}^{(0)}(\tilde{k}_z) \tag{B-3}$$

For given parameters of the beam, grating and mirror, this is an eigenvalue equation for the complex frequency  $\omega$ . The solution depends on the mirror shape  $\Delta x(z)$  through  $\kappa(\tilde{k}_z'' - \tilde{k}_z)$ . For parabolic mirrors the solutions are Gaussian. The eigenvalue  $(\pi + \phi_0 + 2L_x \omega^{(0)}/c) = \phi_{eig} + 2\pi n$ , determines the real mode frequencies.

To the first order Eq. (B-2) gives

$$\bar{E}_{inc}^{(1)}(\tilde{k}_z'') = e^{-i\theta(\tilde{k}_z'')} \int \frac{d\tilde{k}_z}{2\pi} e^{i\phi_{eig} - i\theta(\tilde{k}_z)} \kappa(\tilde{k}_z'' - \tilde{k}_z) [\bar{E}_{inc}^{(1)}(\tilde{k}_z) + (\eta_m + \eta(\tilde{k}_z) + 2i \frac{\omega^{(1)}}{c} L_x) \bar{E}_{inc}^{(0)}(\tilde{k}_z)]$$

We multiply this by  $\bar{E}_{inc}^{(0)*}(\tilde{k}_z'')$  on both sides, and integrate over  $\tilde{k}_z''$ , using Eq. (B-3).

This eliminates all terms involving the unknown field perturbation  $\bar{E}_{inc}^{(1)}$ .

The result is

$$0 = \int d\tilde{k}_z \left| \bar{E}_{inc}^{(0)}(\tilde{k}_z) \right|^2 (\eta_m + \eta(\tilde{k}_z) + 2i \frac{\omega^{(1)}}{c} L_x) \quad (\text{B-6})$$

This is the desired requirement that the growth rate is found by balancing gain and losses, in a wavenumber integrated sense.

References:

1. F. S. Rusin and G. D. Bogomolov, "Generation of electromagnetic oscillations in an open resonator", JETP Letters, **4**, 160-162 (1966)
2. S. J. Smith and E. M. Purcell, "Visible Light from localized Surface Charges Moving across a Grating", Phys. Rev. **92**, 1069-1069 (1953)
3. D. E. Wortman and R. P. Leavitt, "The Orotron", Ch. 7 in "Infrared and Millimeter Waves", vol. 7, Part II, Ed. K. J. Button, Academic Press, New York, 1983.
4. M. B. Tseitlin and E. A. Myasin, "Orotron: analysis of efficient regimes (review)", Radiotekhnika I Elektronika, **38**, 961-981 (1993)
5. V. L. Bratman, I. V. Bandurkin, B. S. Dumesh, A. E. Fedotov, Y. K. Kalynov, N. G. Kolganov, V. N. Manuilov, F. S. Rusin, S. V. Samsonov, and A. V. Saviylov, "Sources of Coherent Terahertz Radiation" in "High Energy Density and High Power RF" (7<sup>th</sup> Workshop on High Energy Density and High Power RF, Kalamata, Greece, 13-17 June 2005), edited by D. K. Abe and G. S. Nusinovich, AIP Con. Proc. **807**, Melville, New York, 2006, 356-366
6. L. A. Surin, B. S. Dumesh, F. Lewen, D. A. Roth, V. P. Kostromin, F. S. Rusin, G. Winnewisser, and I. Pak, "Millimeter-wave intracavity-jet OROTRON-spectrometer for investigation of van der Waals complexes", Rev. Sci. Instrum., **72**, 2535-2542 (June 2001).
7. V. A. Flyagin, A. V. Gaponov, M. I. Petelin, V. K. Yulpatov, "The Gyrotron", Microwave Theory and Techniques, IEEE Transactions on, vol. 25 (6) pp. 514 – 521 (1977)

8. R. Q. Twiss, "Radiation Transfer and the Possibility of Negative Absorption in Radio Astronomy", *Australian Journal of Physics*, vol. 11 pp. 564-579 (1958)
9. J. Schneider, "Stimulated Emission of Radiation by Relativistic Electrons in a Magnetic Field", *Phys. Rev. Lett.*, vol. 2 pp. 504 (1959)
10. A. V. Gaponov, "Interaction between electron fluxes and electromagnetic waves in waveguides", *Izv. Vyssh. Uchebn. Zaved. Radiofiz*, 450; 836 (1959)
11. J. L. Hirshfield and J. M. Wachtel, "Electron Cyclotron Maser", *Phys. Rev. Lett.*, vol. 12 pp. 533 – 536 (1964)
12. G. S. Nusinovich "Introduction to The Physics of Gyrotrons" Published by JHU Press, SBN 0801879213, 9780801879210 (2004)
13. M. Thumm, "MW gyrotron development for fusion plasma applications", *Plasma Phys. Control. Fusion* **45** A143–A161 (2003)
14. K. Sakamoto, "Progress of high-power-gyrotron development for fusion research", *Fusion Science and Technology*, vol. 52 (2) pp. 145-153 (2007)
15. G. G. Denisov, V. E. Zapevalov, A. G. Litvak, and V. E. Myasnikov, "Megawatt gyrotrons for ECR Heating and Current-Drive Systems in Controlled-fusion Facilities", *Radiophysics and Quantum Electronics*, vol. 46 (No. 10) pp. 757-768, (2003)
16. R. W. Gould, "Space Charge Effects in Beam-Type Magnetrons", *Journal of Applied Physics*, **28**, 595-605 (May. 1957)
17. F. S. Rusin and G. D. Bogomolov, "The orotron, an electronic device with an open resonator and a reflecting grating", *Radiophysics and Quantum Electronics*, **11**, 430-433 (1968)

18. F. S. Rusin and G. D. Bogomolov, "Orotron – An Electronic Oscillator with an Open Resonator and Reflecting Grating", Proc. IEEE, **57**, 720-726 (April 1969)
19. A. Gover and P. Sprangle, "A unified theory of magnetic bremsstrahlung, electrostatic bremsstrahlung, Compton-Raman scattering, and Cerenkov-Smith-Purcell free-electron lasers", IEEE J. Quantum Electronics, **17**, 1196-1215 (1981)
20. G. M. Branch and T. G. Mihran, "Plasma frequency reduction factors in electron beams", IRE Trans. Electron. Devices, **ED-2**, 3-11 (1955)
21. G. S. Nusinovich, T. M. Antonsen, Jr., V. L. Bratman, and N. S. Ginzburg, "Principles and Capabilities of High-Power Microwave Generators" (Chapter 2 of "Applications of High Power Microwaves" by A. V. Gaponov-Grekhov, Victor L. Granatstein, published by Artech House, 1994, ISBN: 089006699X, 9780890066997)
22. F. S. Rusin and G. D. Bogomolov, "Oscillating system of the orotron," in "High Power Electronics", edited by P. L. Kapitsa and L. A. Weinstein (Nauka, Moscow, U.S.S.R, 1968), vol. 5, p. 38
23. G. S. Nusinovich, "Analytical nonlinear theory of the orotron", Physics of Plasmas, **13**, paper 053107 (2006)
24. J. H. Booske, Brian D. Mc Vey, and T. M. Antonsen, Jr., "Stability and Confinement of Nonrelativistic Sheet Electron Beams with Periodic Cusped Magnetic Focusing," J. Appl. Phys. **73**,4140 (1993)
25. K. Sakamoto, A. Kasugai, Yo. Ikeda K. Hayashi, K. Takahashi, K. Kajiwara, S. Moriyama, M. Seki, T. Kariya, Y. Mitsunaka, M. Tsuneoka, T. Fujii and

- T. Imai, "Development of Gyrotron and JT-60U EC Heating System for Fusion Reactor", Nippon Genshiryoku Kenkyujo JAERI, Review, pp. 321-326 (2003)
26. K. Felch, M. Blank, P. Borchard, P. Cahalan, S. Cauffman and H. Jory, "Recent Test Results on a 95 GHz, 2 MW Gyrotron", 33<sup>rd</sup> IRMMW 2008, Pasadena", CA, T2A2.1608 (2008)
27. V. L. Bratman and M. A. Moiseev, "Conditions for self-excitation of a cyclotron resonance maser with a nonresonant electrodynamic system", Radiophys. Quantum Electron, vol. 18, pp. 772-779 (1975).
28. A. V. Gaponov, M. I. Petelin and V. K. Yulpatov, "The Induced Radiation of Excited Classical Oscillators and its Use in High-frequency Electronics", Radiophys. Quantum Electron, vol. 10 (9-10) pp. 1414-1453 (1967)
29. J. M. Wachtel and E. J. Wachtel, "Backward wave oscillation in the gyrotron", Appl. Phys. Lett., vol. 37, pp. 1059-1061 (1980)
30. V. L. Bratman, N. S. Ginzburg, G. S. Nusinovich, M. I. Petelin, P. S. Strelkov, "Relativistic Gyrotrons and Cyclotron Autoresonance Masers", Int. J Electron, vol. 51 (4) pp. 541-567 (1981)
31. A. W. Fliflet, "Linear and Nonlinear-theory of the Doppler-shift Cyclotron-resonance Maser Based on TE and TM Wave-guide modes", Int J Electron, vol. 61 (6) pp. 1049-1080 (1986)
32. J. Pierce, "Traveling-Wave Tubes", Van Nostrand (1950).
33. H. R. Johnson, "Backward-wave Oscillators", Proc. IRE, vol. 43 (6) pp. 684-697 (1955)

34. K. R. Chu, M. E. Read and A. K. Ganguly, "Methods of Efficiency Enhancement and Scaling for the Gyrotron Oscillator", IEEE Transactions on Microwave Theory and Techniques, vol. 28 (4) pp. 318-325 (1980)
35. G. Nusinovich and O. Dumbrajs, "Theory of Gyro-backward Wave Oscillators with Tapered Magnetic Field and Waveguide Cross Section", IEEE Transactions on Plasma Science, vol. 24 (3) pp. 620 – 629 (1996)
36. Y. Y. Lau and K. R. Chu, "Gyrotron Travelling Wave Amplifier: III. A Proposed Wide-Band Fast Wave Amplifier", International Journal of Infrared and Millimeter Waves, vol. 2 (3) pp. 415-425 (1981)
37. H. Li, T. M. Antonsen, "Space-Charge Instability in Gyrotron Beams", Phys. Plasmas vol. 1 (3), pp. 714-729 (1994)
38. G. S. Nusinovich, A. N. Vlasov and T. M. Antonsen, Jr., "Nonstationary Phenomena in Tapered Gyro-Backward Wave Oscillators", Phys. Rev. Lett. vol. 87 (218301) (2001)
39. G. Reiter, "Generalized Telegraphist's Equation for Waveguides of Varying Cross-Section," in *Conv. Long Distance Transmission by WaveGuide*, 1959, pp. 54–57; also, Inst. Elect. Eng., paper 3028, Sept. 1959
40. M. Botton, T. M. Antonsen, B. Levush, K. T. Nguyen, A. N. Vlasov, "MAGY: A Time-dependent Code for Simulation of Slow and Fast Microwave Sources", IEEE Tran. Plasma Sci., vol. 26 (3) pp. 882-892 (1998)
41. V. L. Bratman, G. G. Denisov, S. V. Samsonov, "Suppression of Self-Excitation in Relativistic MCR-TWT with Absorbing Wave-Guide", Zhurnal Tekhnicheskoi Fiziki vol. 60 (8), pp. 158-163 (1990)

42. Om P. Gandhi, "Microwave Engineering and Applications", Pergamon Press, ISBN0080255892, 0080255884, pp. 98-99 (1981)
43. S.H. Chen, K. R. Chu and T. H. Chang, "Saturated Behavior of the Gyrotron Backward-Wave Oscillator", Physical Review Letters, vol. 85(12), pp 2633-2636
44. W. R. Perkins, J. B. Cruz, Jr. "Engineering of dynamic systems", Wiley, SBN 471680354, pp.308-313 (1969)
45. S. Y. Park, V. L. Granatstein, and R. K. Parker, "A linear theory and design study for a gyrotron backward-wave oscillator", Int. J. Electron vol. 57, pp. 1109-1123 (1984).
46. K. T. Nguyen, J. P. Calame, B. G. Danly, et al., "Higher order mode excitations in gyro-amplifiers", Phys. Plasmas vol. 8 (5), pp. 2488-2494 (2001)
47. Y. Y. Lau, K. R. Chu, L. Barnett and V. L. Granatstein, "Gyrotron Travelling Wave Amplifier: II. Effect of Velocity Spread and Wall Resistivity", International Journal of Infrared and Millimeter Waves, vol. 2 (3), pp. 395-413 (1981)
48. J. L. Hirshfield, "Cyclotron Harmonic Maser ", International Journal of Infrared and Millimeter Waves, vol. 2 (4), pp. 695-704 (1981)
49. P. Charbit, A. Herscovici and G. Mourier, "A Partly Self-Consistent Theory of the Gyrotron", Int. J. Electron, vol. 51, pp. 303-330 (1981)
50. K. R. Chen and K. R. Chu, "Study of a Noise Amplification Mechanism in Gyrotrons", IEEE Trans. Microwave Theory Technol., vol. MTT-34 (72), pp. 72-79 (1986)
51. A. Bondeson and T. M. Antonsen, Jr., "Space-Charge Instability in Gyrotron Beams" Int. J. Electron, vol. 61, pp. 855-870 (1986)

52. W. M. Manheimer and T. M. Antonsen, Jr., "Shot noise in gyrokystrons", IEEE Transactions on Plasma Science, vol. 26 (3), pp. 444-450 (1998)
53. M. Pedrozzi, S. Alberti, J. P. Hogge, M. Q. Tran, T. M. Tran, "Electron beam instabilities in gyrotron beam tunnels", Physics of Plasmas, vol. 5(6), pp. 2421-2430 (1998)
54. R. G. Kleva, T. M. Antonsen, Jr. and B. Levush, "The Effect of the Time-Dependent Self-Consistent Electrostatic Field on Gyrotron Operation", Phys. Fluids, vol. 31 (2), pp. 375-386 (1988)
55. T. M. Antonsen, Jr., A. Fliflet, J.P. Calame and B. Levush, "Collective theory of shot noise in gyrokystrons", Physics of Plasmas, vol. 8 (10), pp. 4592-4607 (2001)

## Bibliography

- **Jiao Yu**, Thomas M. Antonsen, Jr., Gregory S. Nusinovich, “Self-fields In a Planar Orotron”, IEEE Transactions on Plasma Science, 36, 3, 637 2008
- **Jiao Yu**, Thomas M. Antonsen, Jr., Gregory S. Nusinovich, “Miniature Orotrons utilizing Carbon Nanotube Cathodes”, IEEE Pulsed Power and Plasma Science Conference, Albuquerque, NM 2007
- **Jiao Yu**, Thomas M. Antonsen, Jr., Gregory S. Nusinovich, “Backward Wave Excitation in Gyrotrons”, 33<sup>rd</sup> International Conference on Infrared, Millimeter, and Terahertz Waves, Pasadena, CA 2008
- **Jiao Yu**, Thomas M. Antonsen, Jr., Gregory S. Nusinovich, “Backward Wave Excitation in the Beam Tunnels of High-Power Gyrotron ”, 36<sup>th</sup> International Conference on Plasma Science, San Diego, California 2009
- S. J. Papadakis, A. H. Monica, **Jiao Yu**, J. A. Miragliotta. R.Osiander, T. Antonsen, G. Nusinovich, “Carbon-nanotube field-emitter driven compact, frequency-scanning THz source”, Proceedings of SPIE, 2007
- G. S. Nusinovich, R. Pu, O. V. Sinitsyn, **Jiao Yu**, T. M. Antonsen, Jr. and V. L. Granatstein “Self-Excitation of a Tapered Gyrotron Oscillator”, IEEE Transactions on Plasma Science, 38, 6, 1200, 2010
- **Jiao Yu**, Thomas M. Antonsen, Jr., Gregory S. Nusinovich, “Backward Wave Excitation in the Beam Tunnels of High-Power Gyrotron ”, IEEE Transactions on Plasma Science, 38, 6, 1193, 2010